



SAPIENZA
UNIVERSITÀ DI ROMA

Department of Physics ‘G. Marconi’
PhD in Accelerator Physics

THESIS FOR THE DEGREE OF DOCTOR OF PHILOSOPHY

New high intensity & brightness muon beams for experiments at the intensity frontier



Thesis advisor

Prof. Angela Papa

Thesis co-advisor

Prof. Aldo Sady Antognini

Candidate

Bastiano Vitali

1949877

Academic Year 2023-2024 (XXXVI cycle)

Contents

missing, started, review, correct, done	1
1 Introduction	1
1.1 Outline of this thesis	1
1.2 Particle physics at Paul Scherrer Institute	1
1.3 Bite-size theory	2
1.3.1 Standard Model at low energies	2
1.3.2 Beyond Standard Model at low-energy	4
1.3.3 Muon	5
1.3.4 Muon decay	6
1.3.5 Electric Dipole Moment	7
1.4 Experimental status	8
1.4.1 CLFV experiments	8
1.4.2 EDM experiments	14
1.5 The beams at PSI	16
1.5.1 High-Intensity Proton Accelerator facility	16
1.5.2 Meson production	19
1.5.3 Neutron production	22
1.5.4 High-Intensity Muon Beams	23
1.6 Proton Ionization Facility	26
Bibliography for the introduction	27
I muEDM	32
2 muEDM	33
2.1 Electric Dipole Moment	33
2.1.1 Symmetry violation	34
2.1.2 Current limits on EDM	34
2.1.3 The <i>frozen spin</i> technique	34
2.2 The muEDM experiment	35
2.3 The precursor	35
2.3.1 Superconducting injection channel	35
2.3.2 Entrance detector	36
2.3.3 Muon tracking	36
2.3.4 Kicker	36
2.3.5 Electrodes	36
2.3.6 Positron tracking	37
2.4 Systematics	37
2.5 Conclusions	37
Bibliography on muEDM	37

3 muEDM entrance detector	39
3.1 GEANT4 simulations	39
3.1.1 Entrance system	39
3.1.2 Thin scintillators	39
3.1.3 Telescope and entrance detector	39
3.2 Beamtime 2021	39
3.2.1 Description of the multiple scattering	39
3.2.2 Data taking	40
3.2.3 Data analysis	41
3.2.4 Model evaluation and conclusions	44
3.3 Beamtime 2022: Telescope and entrance detector	45
3.3.1 Construction	45
3.3.2 Data taking	45
3.3.3 Data analysis	45
3.4 Beamtime 2023: Multi readout entrance	45
3.4.1 Data taking	45
3.4.2 Data analysis	45
3.4.3 Describe the beam	46
3.5 Conclusions	46
Bibliography on muEDM entrance detector	46
4 muEDM positron tracker	48
4.1 Design in the proposal 2022	48
4.1.1 SciFi prototype	48
4.1.2 The barrel geometry	48
4.1.3 Issues	48
4.1.4 Alternatives	48
4.2 CHeT or CyFi	48
4.2.1 Resolutions of crossed fibers ribbons	48
4.2.2 Angle choices for the layers	49
4.2.3 GEANT4 simulation	50
4.2.4 From γ s to waveforms	52
4.2.5 From hits to c-hits	54
4.3 Prototype/Beamtime	54
4.4 Conclusions	54
II muCool	55
5 muCool	56
5.1 The working principle	56
5.2 Simulations	56
5.2.1 Cooling	56
5.2.2 Extraction	56
5.2.3 Re-acceleration	56
5.3 Validation	56
5.4 Conclusion	56
6 muCool upgrade	57
6.1 New target	57
6.2 Cryogenic system	57

6.3	High Voltage system	57
6.4	Conclusion	57
III	MEG II	58
7	MEG II and the Cockcroft–Walton	59
7.1	MEG II	60
7.2	XEC	60
7.2.1	Xe scintillation	60
7.2.2	Xe as calorimeter	60
7.2.3	Cryogenics	60
7.2.4	PMTs	60
7.2.5	Performances	60
7.2.6	LED Calibration	60
7.3	Spectrometer	60
7.3.1	COBRA	60
7.3.2	CDCH	60
7.3.3	TC	60
7.4	Trigger and DAQ	60
7.5	Beam and target	60
7.5.1	$\pi e5$	60
7.5.2	Simulations	61
7.5.3	MEG II target	61
7.6	Cockcroft–Walton	62
7.6.1	Description of the machine	62
7.6.2	XEC calibrations	64
7.6.3	X17	64
7.7	CW issues and maintenance	65
7.8	Conclusions	68
8	Liquid Hydrogen target	71
8.1	Charge EXchange reaction	71
8.2	BGO	71
8.3	LH ₂ target working principle	72
8.3.1	Operation and control	74
8.4	2021	74
8.4.1	Data taking	74
8.4.2	Data analysis	75
8.5	2022	75
8.5.1	Upgrades	75
8.5.2	Data taking	75
8.5.3	Data analysis	75
8.6	2023	75
8.6.1	Upgrades	75
8.6.2	Data taking	76
8.6.3	Data analysis	76
8.7	Conclusions	76
Bibliography on LH₂	76	
9	Search for X17	78

9.1	ATOMKI and the X17 ‘anomaly’	78
9.2	X17 in MEG II	78
9.2.1	MC simulations	78
9.2.2	Magnetic field choice	78
9.2.3	Target	79
9.3	Data acquisition	79
9.3.1	Beam tuning	79
9.3.2	Asymmetry	81
9.3.3	Normalization	81
9.4	Data analysis	81
9.4.1	Pair reconstruction	81
9.4.2	Asymmetry	81
9.4.3	Feldman-Cousin	81
9.5	Results and conclusions	82
	Bibliography on X17	82
	Acknowledgement	84

Chapter 1

Introduction

Here we will provide an overview of the following chapters as well as define the theoretical and experimental background for this work. The first section will be dedicated to the outline of this thesis, to aid the readers. A somewhat shallow review of the particle physics searches at PSI will follow, with some in-depth dive into the subjects which are close to the core of this thesis. This will be complemented by the description of the different facilities at PSI, with a final section dedicated to the Proton Ionization Facility. This whole chapter relies heavily on references Calibbi and Signorelli [1] [2].

1.1 Outline of this thesis

The structure of this Thesis might differ slightly from the norm. While most of my colleagues dedicated their work to a singular subject, like a particular detector or theory, my effort during the course of this Ph.D. has been spread on a wider angle. At first glance, this work might seem the result of three separate projects, namely MEG, MuEDM, and muCool. In fact, the spirit in which this Thesis has been developed is orthogonal to the chapters themselves: the overall progress of muonic particle physics experiments.

- Introduction: theory, PSI facilities and key experiments
- muCool (?)
- muEDM: introduction, entrance detector, tracker
- MEG: introduction and CW, Liquid Hydrogen target, X17 search

1.2 Particle physics at Paul Scherrer Institute

Belonging to ETH domain and formed in 1988 as a national laboratory, the Paul Scherrer Institute (PSI) is the largest federal research institute in Switzerland. PSI hosts the world's most powerful proton accelerators, with an average power of 1.4 MW and a beam current of over 2 mA. On top of the proton facility, in the last 10 years, a neutron spallation target has been added for ultracold neutrons production. PSI is renowned for its extensive research across a wide range of scientific disciplines. With its world-class facilities and expertise, PSI plays a pivotal role in advancing our understanding of fundamental particles and their interactions, solidifying its position as a key player in the field of particle physics on a global scale. Everything discussed in this thesis is a

product of the fertile environment at this Institute and the active collaborations with universities and institutions, such as INFN, around the world.

1.3 Bite-size theory

The aim of this section is to define the framework in which (part) of particle physics research is moving. In particular, we will be focusing on the aspects which are relevant to the three experiments core of this thesis. The searches Beyond Standard Model (BSM) proceed in two main directions: *intensity frontier* is used to describe the test of contributions that are too small to be experimentally accessible observing large numbers of events; *precision frontier* is used when improving the accuracy of a specific parameter to test the agreement with the Standard Model (SM). Searches for charged lepton flavour violation (cLFV) or neutron permanent Electric Dipole Moment (EDM) are examples of the former type while precision Quantum ElectroDynamics (QED) tests with muonium are of the latter.

1.3.1 Standard Model at low energies

In the low energy regime QED and Quantum ChromoDynamics (QCD) are essentially ‘frozen’, and the SM reduces to the standard Lagrangian

$$\mathcal{L}_{QED+QCD} = \sum_f \bar{f}(i\cancel{D} - m_f)f - \frac{1}{4}F_{\alpha\beta}F^{\alpha\beta} - \frac{1}{4}G_{\alpha\beta}G^{\alpha\beta} \quad (1.1)$$

where F and G are the electromagnetic and gluonic field-strength tensors. The sum here is on fermions of mass m_f , charge eQ_f , and color $g_s t_f^a$. For a lepton, this would mean $Q_\ell = -1$ and $t_\ell^a = 0$ while for a quark $Q_q = 2/3$ or $-1/3$ and $t_q^a = \lambda^a/2$, with λ Gell-Mann matrices. To compute the matrix element between two lepton states we find:

$$\langle \ell(p_2) | J_{em}^a | \ell(p_1) \rangle = \bar{u}(p_2, m_\ell) \left(F_1^{(\ell)}(q^2) \gamma^a + F_2^{(\ell)}(q^2) \frac{i\sigma^{\alpha\beta} q_\beta}{2m_\ell} \right) u(p_1, m_\ell) \quad (1.2)$$

Here u and \bar{u} are the spinors and the two states are with momenta p_1 and $p_2 = p_1 + q$ while $F_1^{(\ell)}$ and $F_2^{(\ell)}$ are related respectively to the electric charge and the anomalous magnetic moment (AMM). In particular, for the AMM we find

$$F_2^{(\ell)}(0) = a_\ell = \frac{(g-2)_\ell}{2} \quad (1.3)$$

Even when considering non point-like particles, like nucleons $N \in \{p, n\}$ the form used in 1.2 holds and we find:

$$\langle N(p_2) | J_{em}^a | N(p_1) \rangle = \bar{u}(p_2, m_N) \left(F_1^{(N)}(Q^2) \gamma^a + F_2^{(N)}(Q^2) \frac{i\sigma^{\alpha\beta} q_\beta}{2m_N} \right) u(p_1, m_N) \quad (1.4)$$

Here $Q^2 \equiv -q^2$ and, while 1.3 holds, $F_2^{(N)}$ depends on strong dynamics. In the case of nucleons, it is often useful to introduce the *electric* and *magnetic form factors*

$$G_E^{(N)}(Q^2) \equiv F_1^{(N)}(Q^2) - \frac{Q^2}{4m_N^2} F_2^{(N)}(Q^2); \quad G_M^{(N)}(Q^2) \equiv F_1^{(N)}(Q^2) + F_2^{(N)}(Q^2)$$

It is of particular interest that, in the limit for small Q^2 , the form factors can be understood as Fourier transform of extended classical ‘charge’ distributions $\rho_i(r)$

$$F_i(Q^2) = \int d^3r e^{-iq \cdot r} \rho_i(r) = \int d^3r \rho_i(r) + \frac{1}{6} Q^2 \int d^3r r^2 \rho_i(r) + \dots$$

From this, we can write the general expression for the second moment of the charge distribution or EDM. This relation is used for example when determining the charge and magnetic radii of the proton.

$$r_i^2 \equiv \frac{1}{N} \int d^3r r^2 \rho_i(r) = -6 \frac{1}{N} \left. \frac{dF_i(Q^2)}{dQ^2} \right|_{Q^2=0}; \quad N = \begin{cases} 1 & \text{if } F_i(0) = 0, \\ F_i(0) & \text{else.} \end{cases} \quad (1.5)$$

When introducing the weak interaction we arrange fermions in *left-handed doublets* and *right-handed singlets*. We then define the *charged weak current* J_{cc}^α , a similar *neutral weak current* J_{cn}^α and we find

$$\mathcal{L}_{EW} = e A_\alpha J_{em}^\alpha + \frac{g}{\sqrt{2}} (W_\alpha^\pm J_{cc}^\alpha + h.c.) + g_Z Z_\alpha J_{nc}^\alpha; \quad J_{cc}^\alpha = \sum_\ell \bar{\nu}_\ell \gamma^\alpha P_L \ell + \sum_{ij} V_{ij} \bar{u}_i \gamma^\alpha P_L d_j \quad (1.6)$$

where $g = e/\sin\vartheta_W$, $g_Z = e/\cos\vartheta_W$ are the $SU(2)_L$ coupling expressed through the Weinberg mixing angle ϑ_W . Only the left-handed fermions are coupled (through $P_L \equiv (1 - \gamma_5)/2$) and, in the sum over the quark, the Cabibbo–Kobayashi–Maskawa (CKM) matrix V_{ij} describes the flavor-changing effect. When dealing with masses much smaller than m_W and m_Z the result is the ‘effective’ Fermi theory current-current interaction

$$\mathcal{L}_{4F} = -\frac{4G_F}{\sqrt{2}} \left(J_{cc}^\alpha (J_{cc}^\alpha)^\dagger + J_{nc}^\alpha (J_{nc}^\alpha)^\dagger \right) \quad (1.7)$$

In this equation $4G_F/\sqrt{2} = g^2/(2m_W^2)$ and using the definitions for $J_{nc/cc}^\alpha$ we end up with the vector contact interactions. In this framework photons and gluons are the only gauge bosons and the gauge symmetry of the SM $SU(3)_c \times SU(2)_L \times U(1)_Y$ is reduced to QCD and QED: $SU(3)_c \times U(1)_{em}$. We can write a 6-dimension vector operator which links 4 fermions in a generic form

$$[O_f^{XY}]_{ijkl} = (\bar{\psi}_i \gamma^\alpha P_X \psi_j)(\bar{\psi}_k \gamma_\alpha P_Y \psi_l) \quad (1.8)$$

where $X, Y \in L, R$ and i, j, k, l are generation indices. There are many such operators because ψ could be leptons or quarks but the integration of the W and Z generates only a subset (i.g. we have no cLFV operator due to accidental symmetries). In a similar fashion, an operator will be a 6-dimension scalar when removing the γ matrices or a 5-dimension dipole operator including

photons and gluons:

$$[O_{f\gamma}^D]_{ij} = (\bar{\psi}_i \sigma_{\alpha\beta} P_R \psi_j) F^{\alpha\beta}; \quad [O_{qG}^D]_{ij} = (\bar{\psi}_i \sigma_{\alpha\beta} G^{\alpha\beta} P_R \psi_j) \quad (1.9)$$

1.3.2 Beyond Standard Model at low-energy

There is no shortage of BSM models and one way of (roughly) classifying them would be by the masses and coupling strengths of the particles they introduce. Light BSM particles have small couplings to SM particles, which would explain the small contribution to physical observables. Prominent examples are dark photons, axions and Axion-Like Particles (ALPs). Axions in particular were proposed as a solution to the small value of the Charge and Parity (CP) violating QCD ϑ parameter. When discussing Heavy BSM particles we can follow the process of ‘integration’ shown for W and Z in this section, in an Effective Field Theory (EFT) approach. As long as the BSM physics respects QED and QCD gauge symmetry and involves ‘large’ mass scale Λ ($m_b < \lambda < m_W$), it can be integrated out. This way we add higher-dimensional operators to the SM Lagrangian, obtaining a Low-energy Effective Field Theory (LEFT)

$$\mathcal{L}_{LEFT} = \mathcal{L}_{QED+QCD} + \frac{1}{\Lambda} \sum_i C_i^{(5)} O_i^{(5)} + \frac{1}{\Lambda^2} \sum_i C_i^{(6)} O_i^{(6)} + \dots \quad (1.10)$$

To parameterize low-energy observables and measuring (or constraining) associated parameters is not an easy task: a prime example would be the Michel decay (which we will discuss in the following sections), generalized in terms of scalar vector and tensor contact interactions or the similar effort for the cLFV $\mu \rightarrow e\gamma$ and $\mu \rightarrow eee$ with the lepton-flavor-violating contact interactions. If the BSM physics appears at a scale larger than m_W , we first have to develop a Standard Model Effective Field Theory (SMEFT). The details on how this is achieved are outside our purpose but, including all the different gauge fields, Higgs doublet, left-handed doublets, and right-handed singlet (respecting the $SU(3)_c \times SU(2)_L \times U(1)_Y$ gauge symmetry) we find

$$\mathcal{L}_{SMEFT} = \mathcal{L}_{SM} + \frac{1}{\Lambda} (C^{(5)} O^{(5)} + \text{h.c.}) + \frac{1}{\Lambda^2} \sum_i C_i^{(6)} O_i^{(6)} + \dots \quad (1.11)$$

We can now re-evaluate the matrix in 1.2 element using 1.11 instead of 1.1. We will leave the details of the calculation under the hood but the result we get is the following

$$\begin{aligned} \langle f(p_2) | J_{em}^\alpha | f(p_1) \rangle = \bar{u}(p_2, m_f) & \left(F_1^{(f)}(q^2) \gamma^\alpha + \left(F_2^{(f)}(q^2) - i\gamma_5 F_3^{(f)}(q^2) \right) \frac{i\sigma^{\alpha\beta} q_\beta}{2m_f} + \right. \\ & \left. F_4^{(f)}(q^2) \frac{1}{m_f^2} (q^2 \gamma^\alpha - 2m_f q^\alpha) \gamma_5 \right) u(p_1, m_f) \end{aligned} \quad (1.12)$$

It is of interest that the CP-violating F_3 form factor is linked to the EDM of the lepton d_f

$$d_f = \frac{eF_3^{(f)}(0)}{2m_f} \quad (1.13)$$

In the SM, d_f receives contributions from quarks at 3-loops and leptons at 4-loops (induced by CP-violation in the CKM). When considering protons and neutrons there is an additional contribution from the CP violating QCD ϑ parameter (found to be extremely low constraining the neutron EDM). For completeness sake, J_{cc}^α give rise to matrix elements between different $SU(2)$ doublets, like (ν_ℓ, ℓ) or (p, n) . This leads to muon and beta decay or quasi-elastic scattering $\ell p \rightarrow \nu_\ell n$.

1.3.3 Muon

The muon is the lepton with the intermediate mass of $m_\mu \approx 105.66$ MeV and it is unstable. The dominant process is the Michel decay $\mu \rightarrow e\nu\bar{\nu}$ which translates to a lifetime of $\tau \approx 2.2 \mu s$. We already hinted at the fact that this decay is mediated by the charged current J_{cc}^α through $\langle \nu_\mu | J_{cc}^\alpha | \mu \rangle \langle e | (J_{cc})_\alpha^\dagger | \nu_e \rangle$ which in EFT corresponds to $(\bar{\nu}_\mu \gamma^\alpha P_L \mu)(\bar{e} \gamma_\alpha P_L \nu_e)$. The resulting EFT Lagrangian is

$$\mathcal{L}_{Fermi} = -\frac{4G_F}{\sqrt{2}}(\bar{\nu}_\mu \gamma^\alpha P_L \mu)(\bar{e} \gamma_\alpha P_L \nu_e) + \text{h.h} + \mathcal{L}_{QED+QCD} \quad (1.14)$$

When evaluating the lifetime we get an equation that contains, in Δq , all corrections induced by our Lagrangian: electron mass effect, higher order QED correction, and hadronic corrections.

$$\frac{1}{\tau_\mu} \equiv \Gamma_\mu = \Gamma_0(1 + \Delta q) = \frac{G_F^2 m_\mu^5}{192\pi^3}(1 + \Delta q) \quad (1.15)$$

Unfortunately, QCD corrections are non-perturbative for $q^2 \sim m_\mu^2$ and are the leading theoretical uncertainty. These corrections are known at NNLO. Precision measurement of the muon lifetime is key for consistency checks of the SM. In fact G_F can be related to m_W and m_Z

$$\frac{4G_F}{\sqrt{2}} = \frac{g^2}{2m_W^2}(1 + \Delta r) = \frac{2\pi}{\sin^2 \vartheta_W m_W^2}(\Delta r) \quad (1.16)$$

Here Δr are the SM corrections and $\sin^2 \vartheta_W = 1 - m_W^2/m_Z^2$.

On top of the Michel decay, we also have radiative and rare decays

$$\mu \rightarrow e\nu\bar{\nu}\gamma, \quad \mu \rightarrow e\nu\bar{\nu}e^+e^- \quad (1.17)$$

for which we have $B(\mu \rightarrow e\nu\bar{\nu}\gamma) \sim 1.3 \times 10^{-2}$ (for $E_\gamma > 10$ MeV) and $B(\mu \rightarrow e\nu\bar{\nu}ee) \sim 3.6 \times 10^{-5}$. At last, we arrive at the ‘golden’ channels for cLFV studies:

$$\mu \rightarrow e\gamma, \quad \mu \rightarrow eee, \quad \mu^- \stackrel{A}{Z}N \rightarrow e^- \stackrel{A}{Z}N \quad (1.18)$$

With non-vanishing neutrino masses, the branching ratios for these processes are expected to be below 10^{-50} . To extract constraints on BSM physics from the branching ratios we can mostly use standard perturbative methods with the Lagrangian 1.10. For the muon conversion, additional precautions are needed due to the nuclear matrix elements $\langle \stackrel{A}{Z}N | J | \stackrel{A}{Z}N \rangle$ as well as the study of the Decay In Orbit (DIO), electrons for which the energy spectrum was modified by the nuclear recoil.

The last two properties of interest of the muon are the AMM (eq. 1.3) and EDM (eq. 1.13). After the results of the G-2 experiment at Fermi National Accelerator Laboratory (FERMILAB),

there is some tension on the first between experimental results and theory. For the EDM the SM value is zero for practical purposes and a non-vanishing result would be a clear indication of BSM. We will further discuss the muon EDM.

1.3.4 Muon decay

When using a charge-changing Hamiltonian characterized by fields with define chirality [5], the general matrix element of the muon decay can be written as [7]

$$M = 4 \frac{G_F}{\sqrt{2}} \sum_{\substack{\gamma=S,V,T \\ \varepsilon,\mu=R,L}} g_{\varepsilon\mu}^{\gamma} \langle \bar{e}_{\varepsilon} | \Gamma^{\gamma} | (\nu_e)_n \rangle \langle (\bar{\nu}_{\mu})_m | \Gamma_{\gamma} | \mu_{\mu} \rangle \quad (1.19)$$

In this definition, we find: γ indicates a 4-scalar, 4-vector or 4-tensor; Γ Dirac (or Pauli) matrices; ε, μ indicate the chirality of the spinors; m, n the chirality of the neutrinos. This means that the physical interpretation of $g_{\varepsilon\mu}^{\gamma}$ is quite straightforward: $n_{\gamma}|g_{\varepsilon\mu}^{\gamma}|^2$ is the probabilit of a μ -handed muon decaying in a ε -handed electron by the interaction Γ^{γ} (n_{γ} are required for the correct normalization). In this picture, the SM corresponds to $g_{LL}^V = 1$ with all other couplings to 0. **Review chirality vs helicity**

Observables Neglecting radiative corrections, we find the differential decay probability: with reduced energy in $[x, x + dx]$; along \hat{x}_3 with an angle $[\vartheta, \vartheta + d\vartheta]$ with respect to the muon polarization \mathbf{P}_{μ} ; spin along $\hat{\zeta}$.

$$\frac{\partial^2 \Gamma}{\partial x \partial \cos \vartheta} = \frac{m_{\mu}}{4\pi^3} W_{e\mu}^4 G_F^2 \sqrt{x^2 - x_0^2} \cdot \{F_{IS}(x) \pm P_{\mu} \cos \vartheta F_{AS}(x)\} \cdot \{\hat{\zeta} \cdot \mathbf{P}_e(x, \vartheta)\} \quad (1.20)$$

Here, $W_{e\mu} = \max(E_e) = (m_{\mu}^2 + m_e^2)/2m_{\mu}$ is the maximum e^{\pm} energy and $x = E_e/W_{e\mu}$ is the reduced energy ($x_0 = m_e/W_{e\mu}$). This spectrum has both an isotropic (F_{IS}) and anisotropic part (F_{AS}). The electron polarization $\mathbf{P}_e(x, \vartheta)$ can be parametrized by *Michel parameters*, which are combinations of the coupling constants $g_{\varepsilon\mu}^{\gamma}$. If the neutrinos' and x_0 are neglected, 1.20 becomes

$$\frac{\partial^2 \Gamma}{\partial x \partial \cos \vartheta} \sim x^2 \left\{ 3(1-x) + \frac{2\rho}{3}(4x-3) + 3\eta x_0 \frac{(1-x)}{x} \pm P_{\mu} \xi \cos \vartheta \left[1 - x + \frac{2\delta}{3}(4x-3) \right] \right\} \quad (1.21)$$

Here ϑ is the angle between the electron momentum and the muon spin and $x \equiv 2E_e/m_{\mu}$. In the SM we get the following, in which we find the total rate used in 1.15. $\rho = \xi\delta = 3/4$, $\xi = 1$, $\eta = 0$

$$\frac{\partial^2 \Gamma}{\partial x \partial \cos \vartheta} = \frac{G_F^2 m_{\mu}^5}{192\pi^3} [3 - 2x \pm P_{\mu} \cos \vartheta (2x - 1)] x^2 \quad (1.22)$$

The way the $g_{\varepsilon\mu}^{\gamma}$ are connected to the nine decay parameters [3, 10], or the 10 intermediate quantities we can measure [3], is outside the purpose of this short review. The bottom line is that a 20-dimensional space of the complex $g_{\varepsilon\mu}^{\gamma}$ can be mapped to a 10-dimensional space. Unfortunately, many of these parameters are intertwined, and (generally) the precise measurement of individual parameters does not give conclusive information on the type of interaction. To avoid being too vague we will take an example from [2]. The rate S of the reaction $\nu_{\mu} e^- \rightarrow \mu^- \nu_e$, normalized to

the rate predicted by $V - A$ and assuming a negative helicity for ν_μ , has been found close to 1 [17]. S depends on five coupling constants $\{g_{LL}^v, g_{RL}^v, g_{LR}^s, g_{RR}^s\}$ but four of these parameters are found to be small, and in first approximation, we find [7]:

$$S = |g_{LL}^v|^2; \quad |g_{LL}^s| < 2\sqrt{1 - S} \quad (1.23)$$

1.3.5 Electric Dipole Moment

Similarly to how the permanent Magnetic Dipole Moment (MDM) μ represents the coupling between the spin of a quantum system and an external magnetic \mathbf{B} field, the EDM d represents the coupling between the spin of and an external electric field \mathbf{E} . The Hamiltonian describing the spin dynamics, indicating the Pauli matrices with σ , is then:

$$\hat{H} = -\mu\hat{\sigma} \cdot \mathbf{B} - d\hat{\sigma} \cdot \mathbf{E} \quad (1.24)$$

Given that $\hat{\sigma} \cdot \mathbf{E}$ is odd for time reversal, the existence of a non-zero EDM would violate CP symmetry. This is an interesting topic, with many implications, and key to many searches. In a magnetic field, the dynamic of a particle at rest is described by $ds/dt = \boldsymbol{\mu} \times \mathbf{b} = \omega_L \times \mathbf{s}$, where $\boldsymbol{\mu} = ge/(2m)\mathbf{s}$ is the MDM and $\omega_L = -2\mu B/\hbar$ the Larmor precession frequency. Similarly a hypothetical EDM $\mathbf{d} = \eta e/(2mc)\mathbf{s}$ results in a precession $\omega_d = -2d\mathbf{E}/\hbar$ in an electric field \mathbf{E} . When considering a moving particle in both fields it is useful to introduce the polarization vector $\Pi = \mathbf{s}/s$ and the Thomas precession Ω_0

$$\frac{d\Pi}{dt} = \Omega_0 \times \Pi, \quad \Omega_0 = -\frac{e}{m\gamma} \left[(1 + \gamma a)\mathbf{B} - \frac{a\gamma^2}{\gamma + 1}(\boldsymbol{\beta} \cdot \mathbf{B})\boldsymbol{\beta} - \gamma \left(a + \frac{1}{\gamma + 1} \right) \frac{\boldsymbol{\beta} \times \mathbf{E}}{c} \right] \quad (1.25)$$

[3][4] If there is no electrical field parallel to the momentum the acceleration is purely transverse so we get the following motion, with Ω_c the cyclotron frequency.

$$\frac{d\boldsymbol{\beta}}{dt} = \Omega_c \times \boldsymbol{\beta}, \quad \Omega_c = -\frac{e}{m\gamma} \left(\mathbf{B} - \frac{\gamma^2}{\gamma^2 - 1} \frac{\boldsymbol{\beta} \times \mathbf{E}}{c} \right) \quad (1.26)$$

The relative spin precession of a muon in a storage ring will be then given by (T-BMT [**miss-59**])

$$\begin{aligned} \boldsymbol{\Omega} = \boldsymbol{\Omega}_0 - \boldsymbol{\Omega}_c &= \underbrace{\frac{q}{m} \left[a\mathbf{B} - \frac{a\gamma}{\gamma + 1} (\boldsymbol{\beta} \cdot \mathbf{B})\boldsymbol{\beta} - \left(a + \frac{1}{1 - \gamma^2} \right) \frac{\boldsymbol{\beta} \times \mathbf{E}}{c} \right]}_{\text{Anomalous precession, } \omega_a = \omega_L - \omega_c} \\ &\quad + \underbrace{\frac{\eta q}{2m} \left[\boldsymbol{\beta} \times \mathbf{B} + \frac{\mathbf{E}}{c} - \frac{\gamma c}{\gamma + 1} (\boldsymbol{\beta} \cdot \mathbf{E})\boldsymbol{\beta} \right]}_{\text{Interaction of EDM and relativistic } \mathbf{E}, \omega_a} \end{aligned} \quad (1.27)$$

The second term describes the precession due to the EDM coupling to the relativistic \mathbf{E} , perpendicular to the \mathbf{B} in which the particle is moving. The simplification shown are the result of \mathbf{p} , \mathbf{B} and \mathbf{E} forming an orthogonal basis, hence the scalar products are null. In the case of the E821 experiment, the muon *magic* momentum was chosen, simplifying eq. 1.27 and making the anomaly

precession frequency independent from the electric fields needed for beam steering.

$$p_{magic} = \frac{m}{\sqrt{a}} = 3.09 \text{ GeV}/c, \quad \boldsymbol{\Omega} = \frac{q}{m} \left[a \boldsymbol{B} + \frac{\eta}{2} \left(\boldsymbol{\beta} \times \boldsymbol{B} + \frac{\boldsymbol{E}}{c} \right) \right] \quad (1.28)$$

In the presence of a muon EDM the plane would be tilted and a vertical precession ($\omega_e \perp \boldsymbol{B}$), shifted by $\pi/2$ to the horizontal anomalous precession, would become observable.

Paul Scherrer Institute (PSI) has been for decades at the frontier in the measurements of the neutron EDM. We will turn to this topic when describing the existing limits on EDMs and in the chapter dedicated to the muEDM experiment.

[5]

1.4 Experimental status

To give an exhaustive recap of the experimental development, both worldwide and at PSI, is a task we will not undertake. Here we will briefly discuss the key experiments in CLFV searches (MEG, Mu3e, Mu2e, COMET) and the nEDM experiment at PSI. This choice is driven by the experiment extensively discussed in the following chapters: muEDM; MEG II.

1.4.1 CLFV experiments

Process	Upper limit	reference
$\mu^+ \rightarrow e^+ \gamma$	4.2×10^{-13}	[6]
$\mu^+ \rightarrow e^+ e^+ e^-$	1.0×10^{-12}	[7]
$\mu^- \text{Ti} \rightarrow e^- \text{Ti}$	1.7×10^{-12}	[7]
$\mu^- \text{Au} \rightarrow e^- \text{Au}$	7×10^{-13}	[8]
$\mu^+ e^- \rightarrow \mu^- e^+$	8.3×10^{-11}	[9]
$\tau^\pm \rightarrow e^\pm \gamma$	3.3×10^{-8}	[10]
$\tau^\pm \rightarrow \mu^\pm \gamma$	4.4×10^{-8}	[10]
$\tau^- \rightarrow e^- e^- e^+$	2.7×10^{-8}	[11]
$\tau^- \rightarrow \mu^- \mu^- \mu^+$	2.1×10^{-8}	[11]
$\tau^- \rightarrow e^- \mu^- \mu^+$	2.7×10^{-8}	[11]
$\tau^- \rightarrow \mu^- e^- e^+$	1.8×10^{-8}	[11]
$\tau^- \rightarrow e^+ \mu^- \mu^-$	1.7×10^{-8}	[11]
$\tau^- \rightarrow \mu^- e^- e^-$	1.5×10^{-8}	[11]
$\pi^0 \rightarrow \mu e$	3.6×10^{-10}	[12]
$K_L^0 \rightarrow \mu e$	4.7×10^{-12}	[13]
$K^+ \rightarrow \pi^+ \mu^+ e^-$	1.3×10^{-11}	[14]
$K_L^0 \rightarrow \pi^0 \mu^+ e^-$	4.4×10^{-10}	[12]
$Z^0 \rightarrow \mu e$	7.5×10^{-7}	[15]
$Z^0 \rightarrow \tau e$	9.8×10^{-6}	[16]
$Z^0 \rightarrow \tau \mu$	1.2×10^{-6}	[16]

Fig. 1.1: Experimental upper limits for a variety of CLFV processes.

	$\mu^+ \rightarrow e^+ \gamma$	$\mu^+ \rightarrow e^+ e^- e^+$	$\mu^- N \rightarrow e^- N$
Background	Accidental	Radiative muon decay	Decay in orbit
Beam	Continuous	Continuous	Pulsed
Current limit	4.2×10^{-13} MEG [6]	1×10^{-12} SINDRUM [7]	7×10^{-13} SINDRUM II [17]
Planned/running	MEG II [18][19][20]	Mu3e [21][22][20]	Mu2e [23] [24] COMET [25][26][27][28]
Planned sensitivity	$\sim 6 \times 10^{-16}$	$\sim 10^{-16}$	$\sim \text{few} \times 10^{-17}$

Fig. 1.2: Overview of muon CLFV experiments

MEG

The MEG experiment [6] is designed based on two key concepts: the utilization of a liquid xenon detector (LXe) for photons detection, and the implementation of an anti-bottle magnetic field for positron tracking. Muons are stopped within a polyethylene target located at the magnet's center. The momentum of positrons is measured using a combination of drift chambers (DCH) and plastic scintillator timing counters (TC). Photon energy and direction, on the other hand, are determined in a liquid xenon volume containing over 800 photo-multiplier tubes. The measured quantities include electron and photon energies (E_e and E_γ), as well as relative positions (angles $\theta_{e\gamma}$, $\varphi_{e\gamma}$) and time $t_{e\gamma}$. Achieving resolutions that effectively separate background signals, such as radiative muon decays, necessitates an energy resolution of $\lesssim 1\%$ for both particles.

MEG's magnetic field is not uniform to avoid the accumulation of positrons emitted at low-pitch angles within the tracker. Instead, the magnetic field diminishes symmetrically from the center towards the periphery, pushing the particles away from the center. The specific field shape is chosen so that the track radius is proportional to the *absolute* momentum rather than the transverse momentum. This allows low-energy positrons to be discarded by positioning the detector at a sufficient distance from the magnet axis. The magnetic system of MEG, known as "COnstant Bending RAdius" (COBRA) magnets, possesses this distinctive feature.

The DCH spectrometer comprises 16 trapezoidal drift chambers filled with He-C₂H₆, arranged radially. The radial coordinate is determined using the timing data collected by the DCH and TC, while the z position is inferred from the induced charge on the zig-zag-shaped pads on the drift chamber sides. The momentum resolution for positrons is approximately 330 keV.

The choice of employing a liquid xenon scintillating detector for photon reconstruction is motivated by the aim to minimize passive material within the detector and achieve excellent time resolution. This choice provides a higher light yield and shorter decay time compared to other options, such as NaI crystals. The timing resolution for measuring photon interaction time is below 100 ps.

MEG successfully gathered 7.5×10^{14} stopped muons between 2008 and 2013 and, as previously mentioned, established the world's best limit on the branching ratio of $\mu^+ \rightarrow e^+ \gamma$ at 90% confidence level, with $\text{BR}(\mu^+ \rightarrow e^+ \gamma) < 4.2 \times 10^{-13}$ [6].

MEG II The upgraded MEG II experiment was proposed to reduce the contamination due to the accidental background that could not be further reduced in MEG [18] [19]. MEG II is currently running and a whole part (Part III) of this thesis will be dedicated to this experiment.

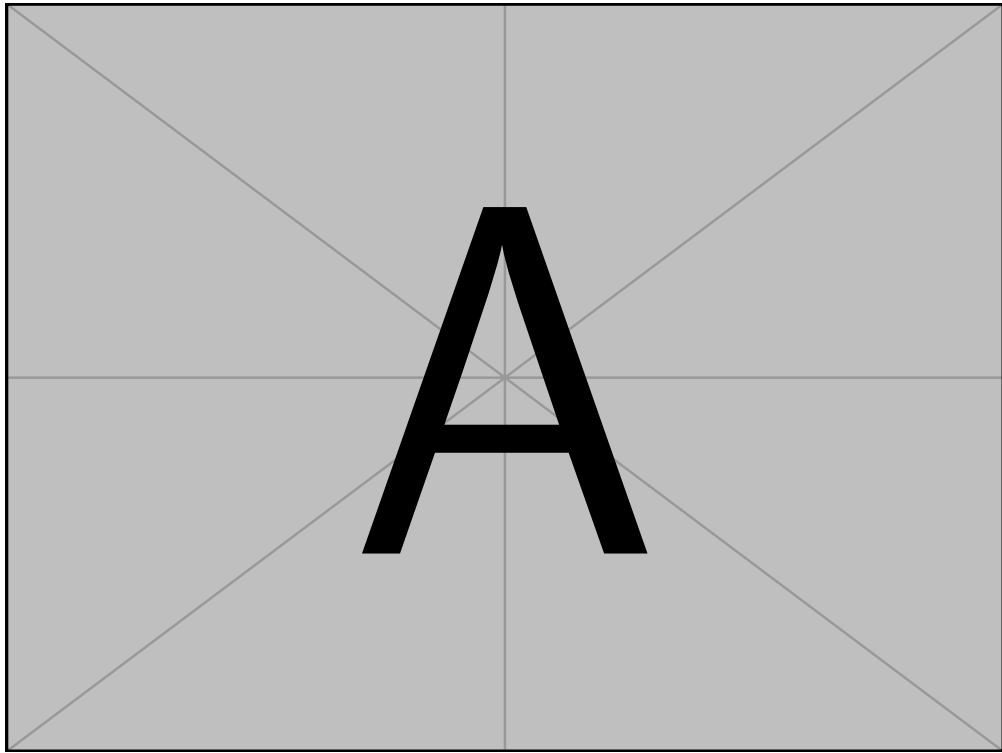


Fig. 1.1: Pictorial view of the MEG experiment [29][6].

Mu3e

The goal of the Mu3e experiment is to achieve a single-event sensitivity on the $\mu^+ \rightarrow e^+e^+e^-$ decay at the order of 10^{-16} [22]. This experiment will utilize the same muon beam as MEG II and employ a thin hollow double-cone Mylar target to stop muons. The detector will be a 2 m cylinder situated within a 1.5 T magnetic field and divided into 5 sections (Fig. 1.3). The central station will consist of two double layers of pixel detectors and a scintillating fiber tracker, while the other four stations will consist of two layers of pixel sensors and a scintillator hodoscope. A visual representation of the Mu3e apparatus can be seen in Fig. 1.2. To mitigate the impact of multiple Coulomb scattering, which poses limitations on precise track reconstruction, the tracker will utilize High Voltage Monolithic Active Pixel (HV-MAPS) technology, designed to partially cancel out the scattering effect within half of a turn. The estimated resolutions for time and vertex are $\sigma_t \approx 100$ ps and $\sigma_{xy} \approx 200$ μm , respectively, while the momentum resolution ranges from 100 to 400 keV for particles with momenta between 10 and 53 MeV/c [1]. The Mu3e experiment is planned in three phases [1], as depicted in Fig. 1.3:

- Phase Ia: Beam with an intensity of $\mathcal{O}(10^7)$ μ^+/s and installation of the tracker only.
- Phase Ib: Beam with an intensity of $\mathcal{O}(10^8)$ μ^+/s (currently the maximum at PSI) with the addition of scintillating fibers and two additional tracking stations.
- Phase II: Beam with an intensity of $\mathcal{O}(10^9)$ μ^+/s (requires a new beam-line) and inclusion of the remaining two stations to achieve the single-event sensitivity of 10^{-16} .

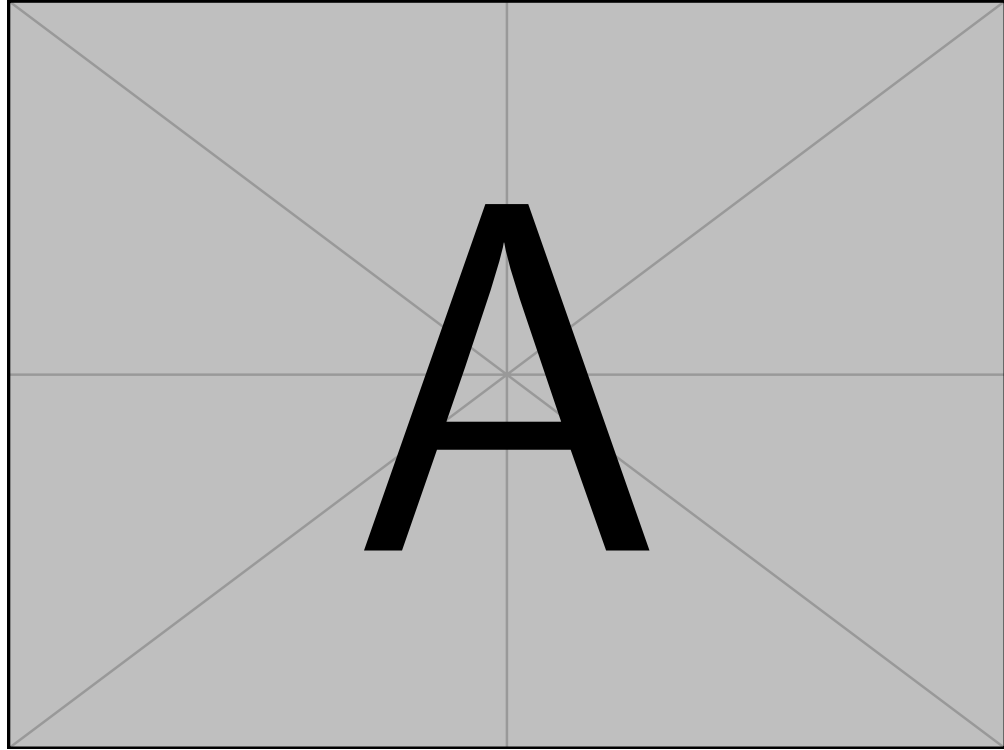


Fig. 1.2: Pictorial view of the Mu3e apparatus [20].

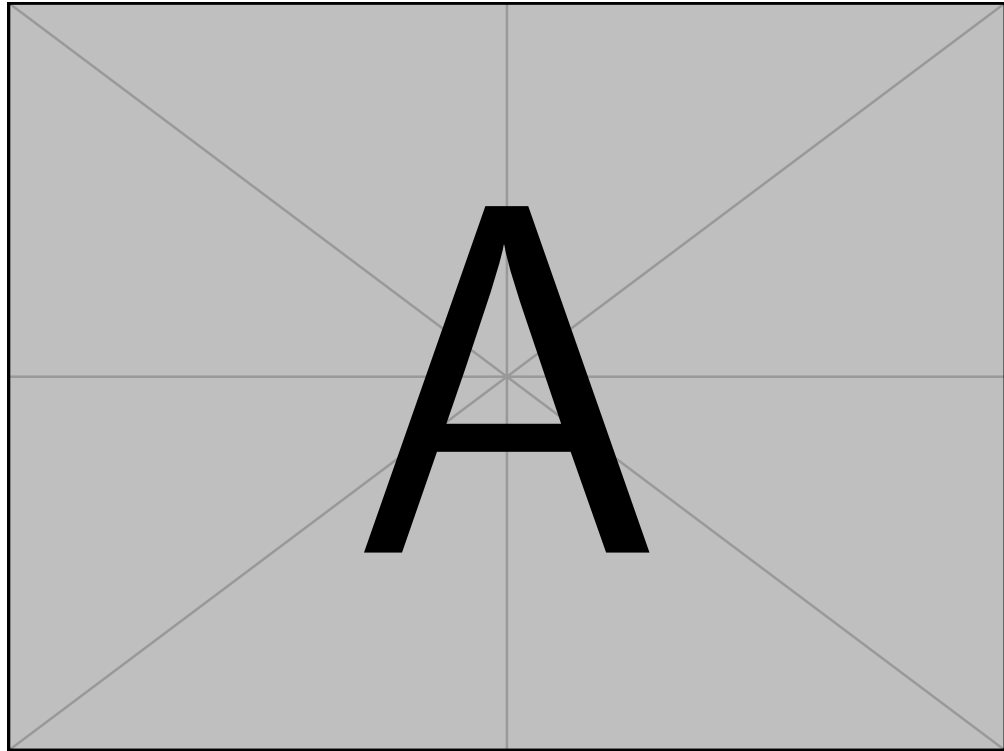


Fig. 1.3: A sketch view of the Mu3e apparatus [30] and the various phases.

Mu2e

Mu2e employs an 8 GeV, 25 kW pulsed proton beam with 100 ns wide bunches separated by 1.7 μ s. Figure ?? illustrates the experimental setup, which consists of three sections: the Production

Solenoid, Transport Solenoid, and Detector Solenoid. The magnetic field layout around the production target is graded to guide the particles into the transport section. Within this section, the gradient directs the particles towards the stopping target, while the S shape reduces background from neutral particles and enables charge sign selection using Eq. ?? and collimators. Generally, only negative muons with momenta below 100 MeV/c reach the stopping target. Downstream of the aluminum target, the straw tube tracker and crystal electromagnetic calorimeter are located. Both detectors feature a hollow-cylinder geometry, with the tracker consisting of crossed straw tubes grouped in 20 stations and the calorimeter composed of two identical disks made of CsI crystals read by SiPMs. With three years of data taking, Mu2e aims to achieve an expected sensitivity of $R_{\mu e} < 3 \times 10^{-17}$ [24].

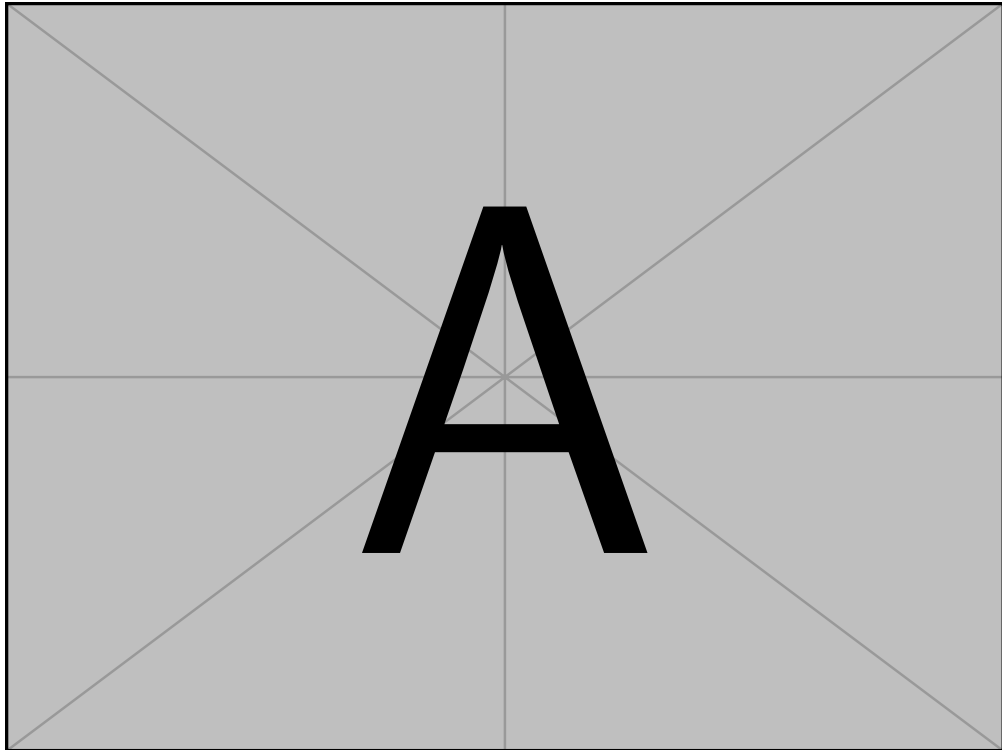


Fig. 1.4: Pictorial view of the muon beam-line of the Mu2e experiment [24].

Mu2e is a collaborative project involving international partners, including the Italian Institute of Nuclear Physics, responsible for constructing the electromagnetic calorimeter. The Mu2e Collaboration is also conducting preliminary investigations for the upgraded Mu2e II [31]. The proton beam intensity will be enhanced through the PIP-II upgrade [32], resulting in a higher rate of stopped muons on target, increasing from $10^{10} \mu^-/\text{s}$ (Mu2e) to $10^{11} \mu^-/\text{s}$. For the upgraded Mu2e II, new detector technologies are being explored. Simulation studies indicate that with three years of data acquisition, Mu2e II is expected to achieve a sensitivity of $R_{\mu e} < 3 \times 10^{-18}$.

COMET

The COherent Muon-to-Electron Transition (COMET) experiment is currently being constructed at the Japanese Proton Accelerator Research Center (J-PARC) [28]. While sharing similarities with Mu2e, such as the use of an 8 GeV, 56 kW pulsed proton beam with a bunch separation of $1.17 \mu\text{s}$, COMET differs in two main aspects, as illustrated in Fig. 1.5:

- The presence of a C-shaped transport solenoid, instead of an S-shaped one, enables a tighter selection of muon momentum, at the cost of reduced beam intensity (approximately 70%)
- An additional curved solenoid after the stopping target eliminates most of the non-interesting electrons before they reach the tracker.

The development of COMET will occur in two phases: Phase-I and Phase-II (Fig. 1.5).

COMET Phase-I This initial phase aims to establish the experimental techniques, study background effects, and achieve an intermediate measurement at $R_{\mu e} \approx 7 \times 10^{-15}$. The proton power will be limited to 3.2 kW, and a single 90° bend will be employed. The main challenge lies in the short distance between the various elements, with a cylindrical drift chamber serving as the electron tracker. Scintillating hodoscopes will surround the tracker for triggering and timing purposes. The Technical Design Report (TDR) for COMET Phase I can be found in [28].

COMET Phase-II To accommodate the increased particle rate, COMET Phase-II will introduce a straw tube tracker and a crystal electromagnetic calorimeter utilizing LYSO crystals. The entire magnetic system will be expanded and refined. The two-step approach is driven by uncertainties in the understanding of the underlying physics processes. Firstly, the backward production by 8 GeV protons remains poorly known, despite results from the HARP experiment [33]. Additionally, data on muon nuclear capture in aluminum is still limited, although efforts from the Mu2e and COMET collaborations have led to the development of the AlCap experiment at PSI [34][35][36]. The AlCap collaboration aims to measure the rate and spectra of particles emitted during muon capture in aluminum to improve the physics models employed in Monte Carlo simulations.

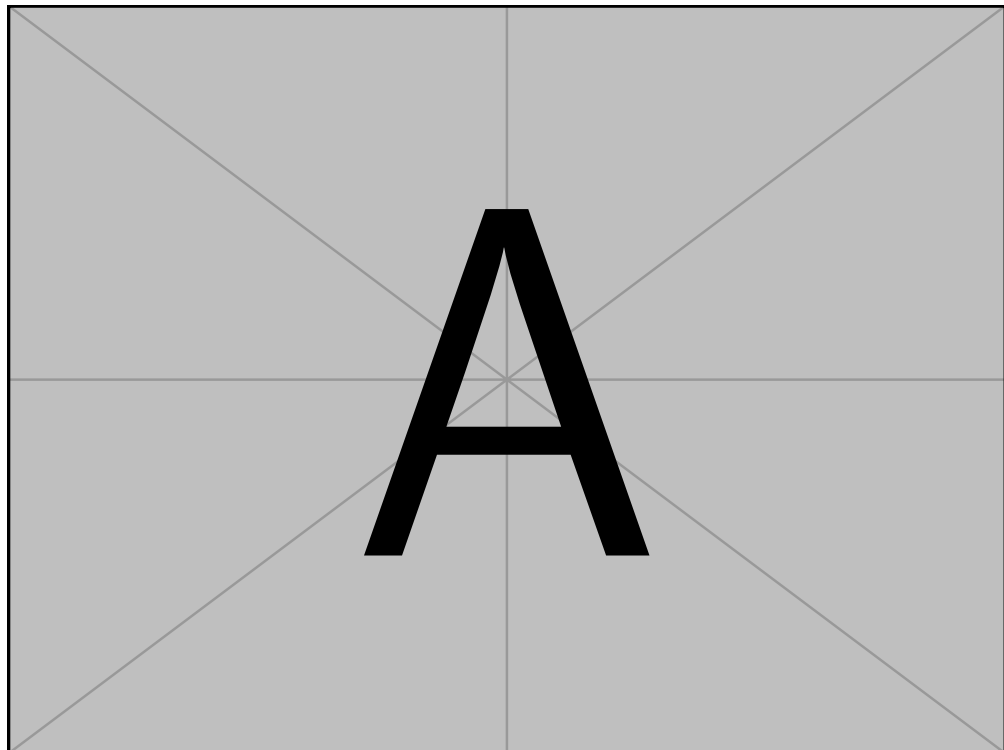


Fig. 1.5: Pictorial view of the COMET apparatus [28].

Experiment	Particle	EDM limit in ecm
nEDM [37]	n	0.18×10^{-25}
ACME [38]	e	1.1×10^{-29}
Indirect [39]	μ	$0.19 \times 10^{-19*}$
g-2 [40]	μ	1.8×10^{-19}

Fig. 1.3: Sumary of the current limits on the EDM for neutron electron and muon.

1.4.2 EDM experiments

In the last decades the interest towards EDM measurments and limits palyed an important part in testing old and new theories. A summary of the current limits is in Tab. 1.3. This subsection is a rundown of the experiments setting these limits.

Neutron: nEDM

n2EDM [41]

Electron

The conventional way to measure EDM is the separated oscillatory fields method: when a particle is subjected to an electric field parallel to a weak magnetic field the EDM changes interaction changes the Larmor frequency [42]. An alternative approach is to use solid-state techniques. In the presence of a strong magnetic field the EDM of valence electrons in a paramagnetic insulator would generate a small magnetization. Even though the effect is negligible for singular electrons, the cumulative effect can be detected using sensitive magnetometry. Using this method the limit $d_e < 6.05 \times 10^{-25} \text{ e} \cdot \text{cm}$ was obtained in $\text{Eu}_{0.5}\text{Ba}_{0.5}\text{TiO}_3$ [43]. Not long after, a different limit was set with the same technique in Gadolinium Gallium Garnet (GGG, $\text{Gd}_3\text{Ga}_5\text{O}_{12}$): $d_e = -5.57 \pm 7.89 \pm 0.12 \times 10^{-25} \text{ e} \cdot \text{cm}$ [44]. The choice of material is driven by:

- A strong magnetic response, generated by the high density of Gd^{3+} ions ($\sim 10^{-22} \text{ cm}^{-3}$), each with 7 unpaired electrons in $4f$ shell
- High dielectric strength (10 MV/cm) and electrical resistivity

ACME The current limit on eEDM was actually set by the ACME collaboration [38] using a different method: measuring the spin precession in a superposition of quantum states. As illustrated in Fig. 1.6, the measuring principle is the following:

- A collimated beam of ThO enters a E, B fields region
- A combination of lasers creates a spin state aligned with \hat{x}
- The spin precesses in the E, B fields
- The final spin alignment is readout by a laser: the resulting fluorescence depends on the angle between the laser linear polarization and the spin direction

The key aspect is that the precession frequency is linked to the states of the system and is modified by the presence of d_e . The results obtained is $d_e = (4.3 \pm 3.1 \pm 2.6) \times 10^{-30} \text{ e} \cdot \text{cm}$. Applying the Feldman–Cousins prescription this value translates to the limit $|d_e| < 1.1 \times 10^{-29} \text{ e} \cdot \text{cm}$.

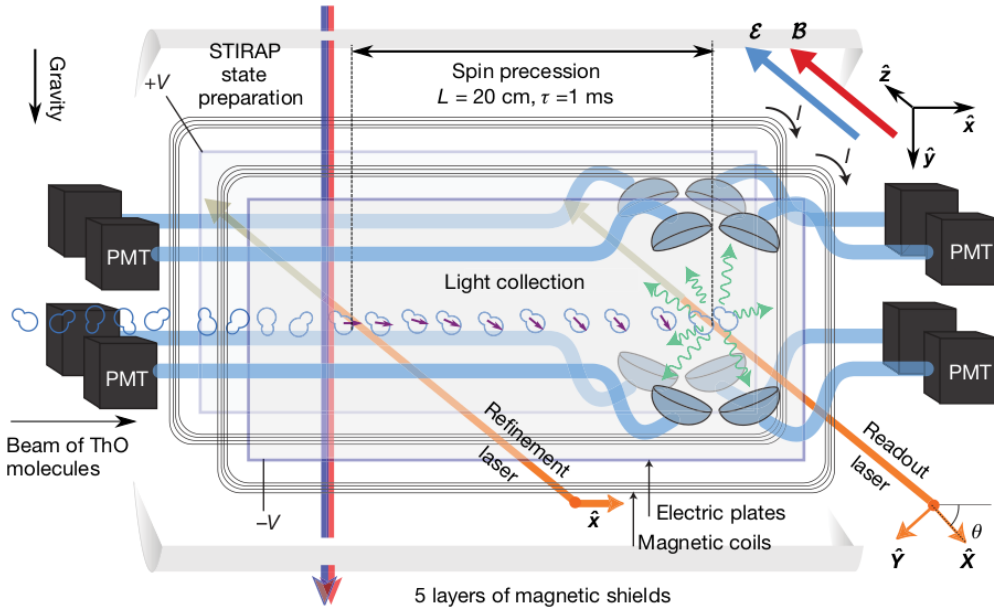


Fig. 1.6

Muon

We now come to the muon, to which most of this thesis is dedicated. The d_μ search at PSI is going to be discussed in detail in the following chapters but we will here review the current limits.

Muon g-2 In 2018 the $g-2$ collaboration performed three independent searches for d_μ . All results were compatible with a null value and an upper limit was set: $|d_\mu| < 1.9 \times 10^{-19} \text{ e} \cdot \text{cm}$ [40]. We will here skip the details but we will outline the methods used.

BNL We saw in 1.3.5 the effect that EDM and MDM have on a moving particle in E, B fields. In particular, for muons circulating in a storage ring, the spin precession is given by Eq. 1.27. The measurement with the $g - 2$ detectors is achieved by measuring the oscillation of the vertical component of the positron from the decay. This direction reflects the oscillation of the muon spin.

$g - 2$ We will here skip the details but we will outline the methods used. We saw in 1.3.5 the effect that EDM and MDM have on a moving particle in E, B fields. In particular, for muons circulating in a storage ring, the spin precession is given by Eq. 1.27.

FSD We will here skip the details but we will outline the methods used. We saw in 1.3.5 the effect that EDM and MDM have on a moving particle in E, B fields. In particular, for muons circulating in a storage ring, the spin precession is given by Eq. 1.27.

Indirect limit Given the rise in interest for EDM measurements an effort was undertaken to assess the indirect constraints imposed on d_μ by the EDM measurements performed with heavy atoms and molecules [39]. This was done by evaluating the d_μ - induced *Shift moment*¹ of the ^{199}Hg

¹As pointed out in [45], this is the operator inducing the atomic EDM.

nucleus, and a specific CP-odd operator for ThO. The results, $d_\mu(^{199}\text{Hg}) < 6.4 \times 10^{-20} \text{ e} \cdot \text{cm}$ and $d_\mu(\text{ThO}) < 1.9 \times 10^{-20} \text{ e} \cdot \text{cm}$, are more stringent than the current measured limit but are *indirect*.

1.5 The beams at PSI

1.5.1 High-Intensity Proton Accelerator facility

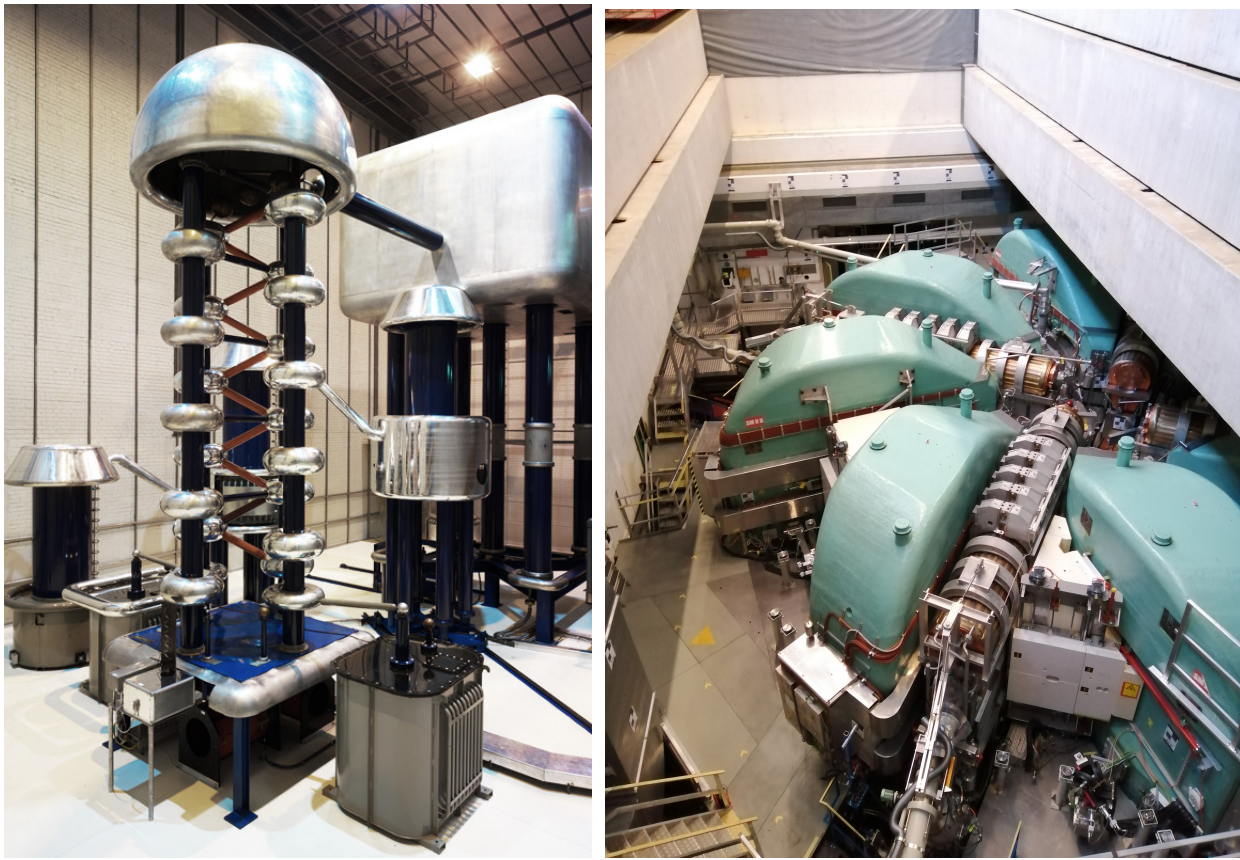
The proposal for the accelerator facility at PSI was completed in 1963. The objective was to develop a proton beam of tens of microAmpere and energy above 450 MeV to produce π/μ . The main accelerator is a cyclotron designed to accelerate the beam from 72 MeV to 590 MeV. The first pre-accelerator, Injector I cyclotron, was developed to accelerate protons and light ions up to 72 MeV and 180 μA . The performances steadily improved up to 180 μA but the beam losses at the extraction from the Injector I were the bottleneck. The Ring cyclotron was deemed to have the potential to surpass 2 mA. For this reason, in 1978, the proposal of using two pre-accelerators was approved: a 860 keV Cockcroft-Walton (CW) followed by a new Injector II cyclotron.

Since 2010 the chain is the following:

- Protons are produced by an electron cyclotron resonance source with a 60 kV extraction
- Two solenoids focus the protons onto a collimator: here $^2\text{H}^+$ and $^3\text{H}^+$ ions are stopped
- Protons are then accelerated in three stages
 - From 60 keV to 870 keV by the CW DC linear accelerator, shown in Fig. 1.7a
The beamline connecting the CW to the Injector II is equipped with a bunching system to match the acceptance of Injector II
 - Injector II accelerates the pre-bunched beam up to 72 MeV. An electrostatic beam splitter can redirect a fraction of the beam extracted beam (up to 100 μA) to produce radioisotopes
 - The beam is sent to the Ring cyclotron, shown in Fig. 1.7b. Eight magnets keep the particles on the spiral path and four cavities accelerate the beam up to 590 MeV
- After the acceleration the beam is extracted and sent to the meson production targets
- The surviving $\sim 65\%$ of the beam is sent to the spallation source SINQ (or to a beam dump)

Injector II The Injector II cyclotron is designed for high-current operation (1 mA and above) with minimal extraction losses. It achieves high extraction efficiency through a combination of factors: high accelerating voltage, large radius, large gap magnets, and low energy spread. To counter space charge forces, a high vertical betatron tune² is employed. Injector II is a low-field separate sector machine with four wedge sectors, accommodating two high-voltage double-gap resonators and two single-gap flat-top resonators. Its 870 keV injection energy allows for beam collimation and halo cleanup, being below the Coulomb threshold. The "vortex motion" is an interesting phenomenon caused by space charge in isochronous cyclotrons [46]. For long initial bunches, self-sustaining round sub-bunches are generated, while for short and compact bunches, the vortex effect stabilizes the bunch [47] [48]. The PSI operation crew discovered the usefulness of self-focusing, achieving high extracted currents with low losses by operating in an accelerating mode without the need for the flat-top system. In an ongoing upgrade program, Injector II will

²Refers to the number of vertical or horizontal oscillations that a particle undergoes per turn in a cyclotron, indicating the level of vertical or horizontal focusing.



(a) CW feeding the Injector II

(b) Picture of the Ring cyclotron.

Fig. 1.7: Picture of two of the stages of the HIPA facility: the Cockcroft-Walton bringing the proton up to 870 keV and the Ring cyclotron accelerating them up to 590 MeV.

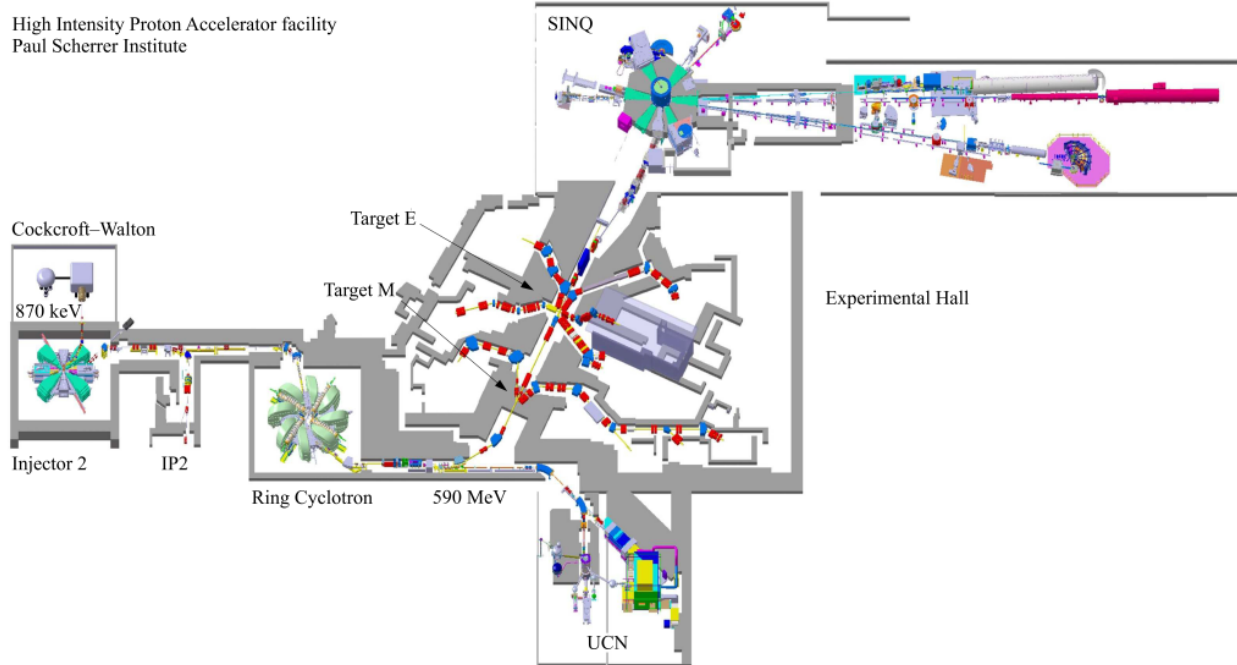


Fig. 1.8: High Intensity Proton Accelerator (HIPA) facility at PSI

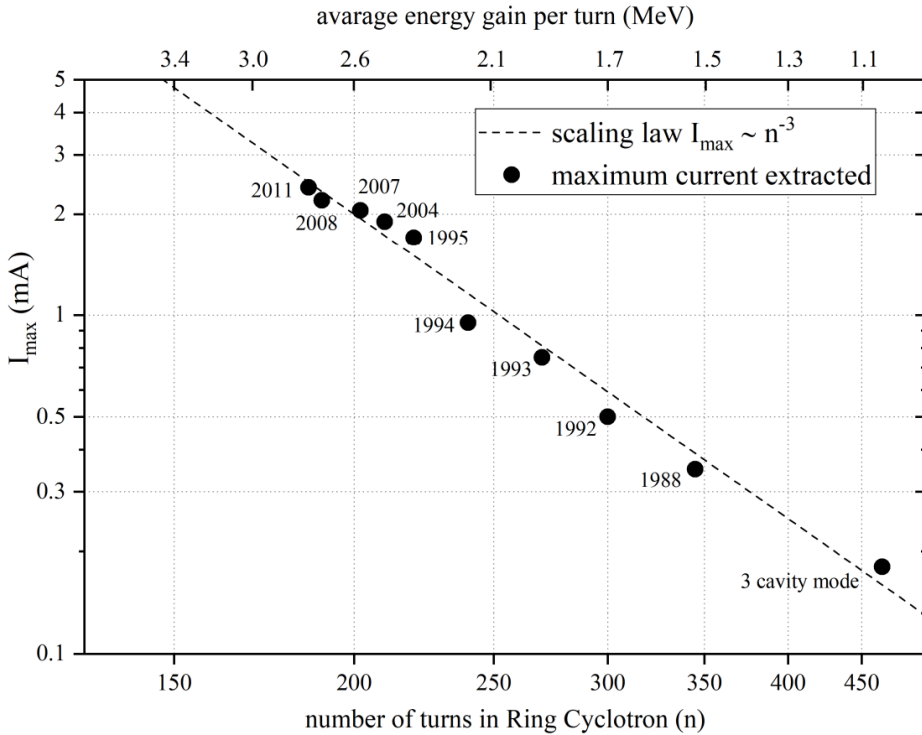


Fig. 1.9: In 1981, Werner Joho introduced Joho's N3-Law, an analysis of high-intensity issues in cyclotrons [49]. This law states that the current limit dominated by losses scales inversely with the third power of the number of turns in the cyclotron: $I_{\max} \propto N^{-3}$. Remarkably, this formula accurately predicted the performance of the PSI Ring cyclotron for the subsequent two decades.

replace the flat-top resonators with two 50MHz high-voltage resonators. This upgrade aims to reduce extraction losses and enable higher beam currents. Notably, Injector II is the only known production cyclotron worldwide that harnesses the vortex effect.

Ring cyclotron Over time, the Ring cyclotron's performance was improved, particularly its extraction efficiency. Initially, a well-centered beam was required to pass the Walkinshaw resonance³ without significant loss. However, by December 1976, an extraction efficiency of 99.9% was achieved with a peak intensity of 112 μ A. Ten years later, Injector II alone achieved a beam current of 1mA, and in combination with the Ring cyclotron, reached 310 μ A. To increase the intensity, the Ring underwent an RF system upgrade, while a bunching system was implemented in the injection line. The upgrades allowed for a reduction in Ring turns, resulting in a production current of 2.2 mA and a beam power of 1.3 MW, in line with Joho's N^3 -Law (see Fig. 1.9). Further upgrades, including the replacement of the 150MHz flattop cavity, are expected to enable a beam current of 3 mA and power of SI1.8MW for both Injector II and the Ring cyclotron.

Performances

HIPA operates at a beam power of up to 1.42 MW. The maximum beam power (1.42 MW) is limited by the activation and damage of the accelerator components while the maximum beam current authorized is 2.4 mA. The increase of the beam power in the period between 1974 to

³The Walkinshaw resonance is a phenomenon in cyclotrons where beams experience a resonance with the machine's magnetic field modulation. Proper alignment and adjustments are necessary to prevent significant beam loss.

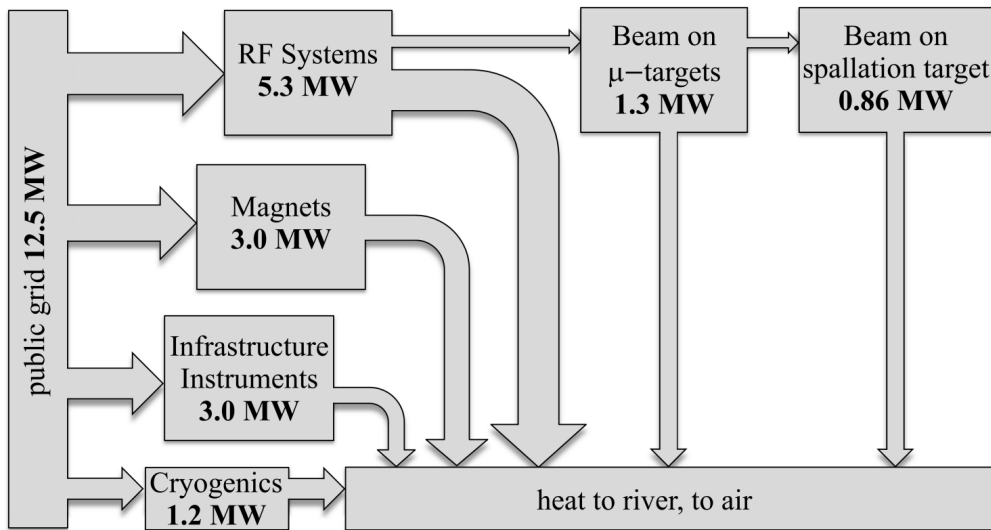


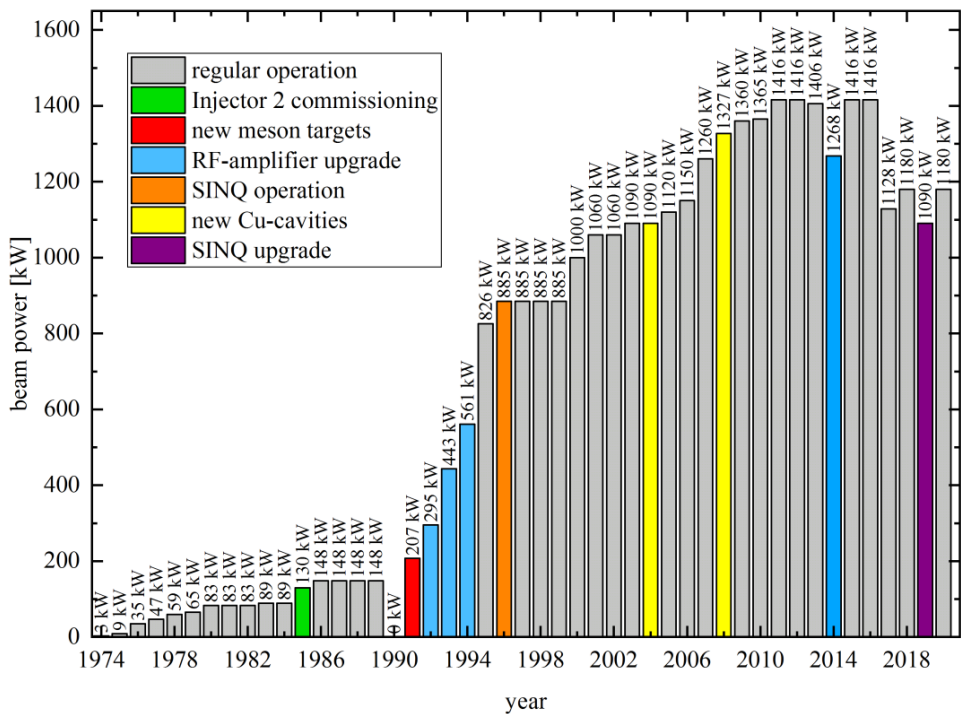
Fig. 1.10: Detail of the power usage of the HIPA facility.

2020 is shown in Fig. 1.11. The history of the delivered charge to the meson production targets and SINQ is shown in Fig. 1.12. A major limiting factor is the scattering of halo particles in the extraction septum. There are two key elements for low-loss beam extraction: the generation of beam tails must be suppressed as best as possible and the turn separation at the extraction septum must be maximized. In this way, the density of halo particles at the position of the extraction septum is minimized. The beam is operated 24/7 around 200 days a year. Every three weeks of operation two days of maintenance are scheduled. The details of the different particle production are discussed in the following subsections.

Power The experiments at HIPA require high-intensity particle beams for precise measurements, which consume significant electrical power. Upgrades aim to achieve higher particle flux and brightness, necessitating even greater power. Considering the global energy consumption challenges, improving HIPA's energy efficiency is crucial. Fig. 1.10 displays the power consumption breakdown of the proton facility. During routine operation at a beam current of 2.2 mA, 1.3 MW, the overall power consumption is approximately 12.5 MW leading to an efficiency of 11%. For the bare accelerator, the figure is 18%. The RF-to-beam power conversion accounts for the majority of this consumption, around 5.4 MW. It scales linearly with beam power, while the power consumption of magnets and auxiliary systems remains independent of the beam power. It can be shown that the efficiency can increase with higher current and the aim is >20% with 3 mA.

1.5.2 Meson production

As we saw in 1.5.1, High Intensity Proton Accelerator (HIPA) delivers a continuous 2.4 mA 590 MeV proton beam. To have a high pion/muon yield a low Z material is the best choice for the Meson Production Targets: graphite has been used since 1990's. The whole system (target, collimators, beam dumps, ...) has to be cooled and, due to nuclear reactions, is highly radioactive. Pions are produced by the interaction with nucleons in the target (threshold at 280 MeV in the center-of-mass frame) and muons are then produced by pion decay. When π^- are stopped at ~ 1 mm from the surface of the target, μ^+ can escape and are called *surface muons*. These muons have



Target	User facility	Particles	Momenta (MeV/c)	Rate ($s^{-1}mA^{-1}$)
M (5 mm)	$\pi M1$	$e/\pi/\mu/p$	10-450	2×10^8
	$\pi M3.1-3$	μ	10-40	3×10^6
E (4/6 cm)	$\pi E1$	$\pi/\mu/p$	10-450	1×10^9
	$\pi E3$	μ	10-40	3×10^7
	$\pi E5$	π/μ	10-120	5×10^8
	$\pi E1$	μ	60-120	6×10^7
	$\pi E4$	μ	10-40	4×10^8

Fig. 1.4: Particle types available at the meson facilities. The rate in particles per second per 1 mA of proton

energies below 4.1 MeV ($p = 29.8$ MeV) and are $\approx 100\%$ polarized. Muons created by in-flight decay have higher energies and are cooled *cloud muons*. Both positive and negative muons are possible but the negative charge is suppressed by a factor ~ 3 . There are two targets: M feeds two beamlines (PiM1 and PiM3; E feeds 5 beamlines (PiE1, MuE1, MuE4, PiE3, PiE5). The detail of the facilities are summarized in Tab. 1.4. The targets are graphite wheels which rotate to distribute the heat due to the impinging beam. The material is polycrystalline graphite made of small crystallites of $\sim 20\text{ }\mu\text{m}$ irregularly arranged.

E Target The target is inserted vertically into the beamline and held by a horizontal rotating shaft. The graphite and the hub are connected by six spokes. While operated at 2 mA, the temperature of this 40 mm/60 mm target is ~ 1700 K. Water-cooled copper shields are mounted on the rear of the target. To reduce the deformations the graphite rim is made of 12 segments. Variations of the beam positions are crucial and to improve the sensitivity the graphite wheel was modified: small grooves were applied on both sides. This modulates the beam transmission. At the end of 2019 a new target wheel was tested, having a small angle for the impinging beam. This *slanted target* keeps the effective thickness creating a larger active surface and two different spots for IN-/OUT of the beam. The net effect is an increase $\sim 50\%$ in the surface muons. As the bearings degrade from heat and radiation they have to be replaced after a few months of operation. The procedure for the maintenance of the target here will not be discussed.

M Target This target is smaller in thickness and the bearings are far from the beam thus the demands are less challenging. The rim of the target is 2 cm wide and 2 mm thick. With an impinging angle of 30 deg the effective thickness is 5.2 mm inducing a beam loss of 1.6%. The target operates at 1100 K and is cooled by conduction. For the upcoming High Intensity Muon Beam (HIMB) the aim is to increase the muon rate by a factor up to 100. For this purpose studies for an upgrade of the M target station, with a slanted target design, are ongoing. A similar slanted target was already tested in the E target station, yielding a $\sim 50\%$ increase in surface muon rate.

Collimators and Beam dump Just like target E, Collimators and beam dump are inserted vertically and shielded. Both are made of oxygen-free copper: improve thermal conductivity; avoid hydrogen embrittlement⁴; for brazing of the steel tubes onto the copper body. To avoid any significant change in the material, the copper is kept below 400 K using water-cooling. The collimator

⁴Hydrogen can be produced by the spallation reaction of the protons with copper. This hydrogen can bond with oxygen creating water molecules that can produce cracks in the copper.

system as well as the beam dump have to stand more than 100 kW per component. The water flows in stainless steel pipes are wound outside and brazed on the cylindrical body. This is done to avoid direct contact of the proton beam with the water, which would create corrosion-inducing ions. The main body is made of six slices brazed together. The shape and manufacture of these sections were optimized using computational fluid dynamics in order to reduce the energy deposit and thermal stress. An aperture, made of 4 slits of 100 μm Nickel foils, is mounted in front of the devices. Here free electrons from ionization are collected and used for beam position and size monitoring. Aside from a water leak problem, likely due to thermal stress, no visible signs of radiation damage are observed since installation.

1.5.3 Neutron production

SINQ

The first spallation neutron source built at PSI was SINQ, which has dedicated neutron scattering instruments and was used as a polarized cold-neutron beam line for fundamental neutron physics. After passing through the meson production target the proton energy is degraded to 570/565 MeV. The beam is bent downwards and then up vertically onto the spallation target. The thermal neutron flux scales with the beam current and is $\sim 1.5 \times 10^{14} \text{ cm}^{-2}\text{s}^{-1}$ near the target. This beamline was used for many measurements conducted in preparation for the UCN source and many parameters of UCN production (and loss) were here determined.

UltraCold Neutrons

Neutrons below 4 mK are called UltraCold. This corresponds to energy below 300 neV, which is comparable with the gravitational potential of a neutron at a few meters height and also the neutron optical potential: material bottles can hence contain UCNs. The design of the UCN source, shown in Fig. 1.13, was presented in 2000 to push the sensitivity of the nEDM search.

Source setup The HIPA 590 MeV proton beam is deflected by a magnetic kicker and sent in the spallation source. Each spallation reaction with the lead atoms leads to an average of 8 neutrons, which are then thermalized in heavy water. The main moderator is made of solid deuterium at 5 K. The UCN produced exit the moderator's vessel through a thin aluminum lid in a vertical guide and their energy is lost to gravity. From here the UCN are delivered via long neutron guides: two at the bottom and one at the top of the vessel. The 30 liters of solid D₂ is the core of the whole system and takes several days to achieve a good ice quality. UCN intensity reflects the quality of the achieved solid deuterium, as shown in Fig. 1.14 exemplifying a typical UCN intensity behavior during such a slow freezing process.

Performance A key parameter in the performance of a UCN source is the number of particles delivered. The exponential decay measured at the lower ports reflects the emptying time of the central storage vessel. Measuring in the higher port a faster exponential is found, demonstrating that the UCNs with energies high enough to reach that port are quickly drained. Several studies to understand all aspects of the UCN source have been conducted since its inauguration, as well as the UCN transport from production in the solid deuterium to a beam port. A slow decrease in

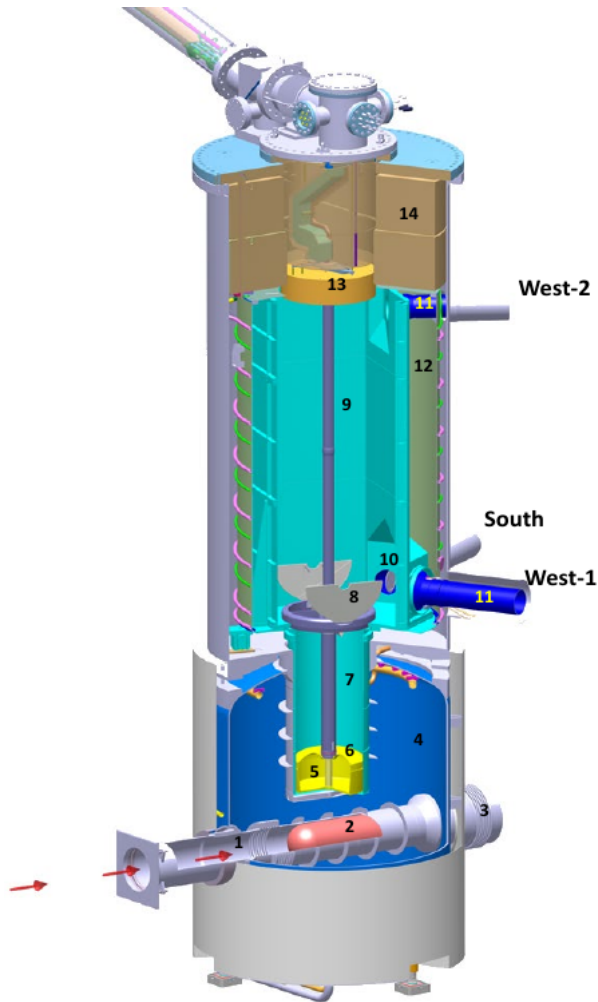


Fig. 1.13: CAD for the UCN source taken from [2]. Some of the key aspects are: 2 - lead spallation source, 4 - heavy water moderator, 5 - D_2 moderator, 9 - storage vessel, 10 - 11 UCN guide and guide shutter.

performance was discovered and a temperature-cycling “conditioning” was developed to regain maximum UCN intensity. The UCN source has been reliably operating since 2011 (see Fig. 1.15).

Results The resulting nEDM limit $d_n = (0.0 \pm 1.1_{stat} \pm 0.2_{sys}) \times 10^{-26}$ ecm was published in 2020 [37] but other results were also obtained thanks to this facility:

- A measurement of the mercury-to-neutron magnetic moment ratio
- Spin-echo spectroscopy with ultracold neutrons
- Measurement of gravitational depolarization of ultracold neutrons
- limit for oscillating electric dipole moments
- limit for spin-dependent forces mediated by axion-like particles

1.5.4 High-Intensity Muon Beams

Currently, PSI delivers the most intense continuous muon beam in the world with up to a few $10^8 \mu^+ / s$. The High-Intensity Muon Beams (HiMB) project at PSI focuses on the development of a new target station and muon beamlines to deliver up to $10^{10} \mu^+ / s$ [50][51]. The aim is to boost the production, collection, and transport of surface muons. HiMB is part of the Isotope and Muon

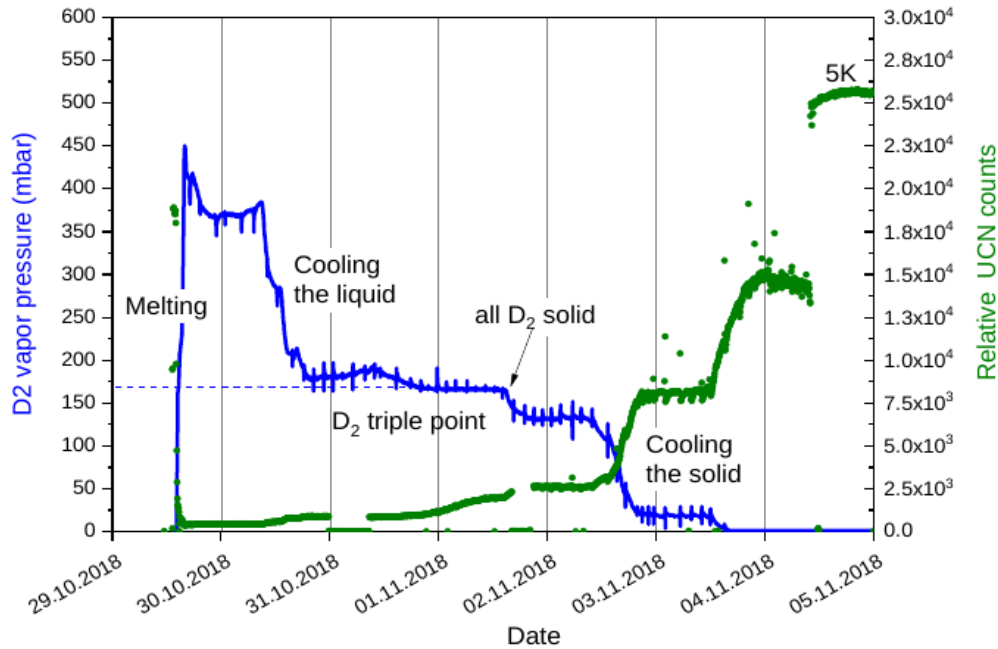


Fig. 1.14: The observed behavior during the slow freezing of the deuterium. The large increase in UCN output demonstrates the strong reduction in UCN losses within the D₂. Figure taken from [2]

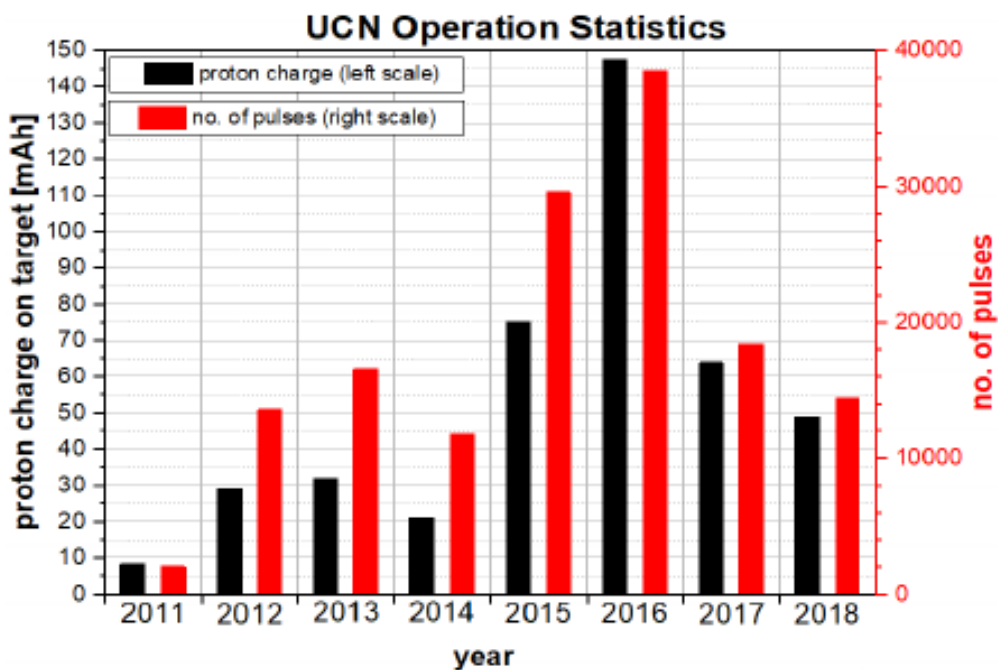


Fig. 1.15: Annual statistics of the UCN source showing total accumulated beam current on target (black bars) and number of beam pulses (red bars) on the UCN spallation target. Figure taken from [2]

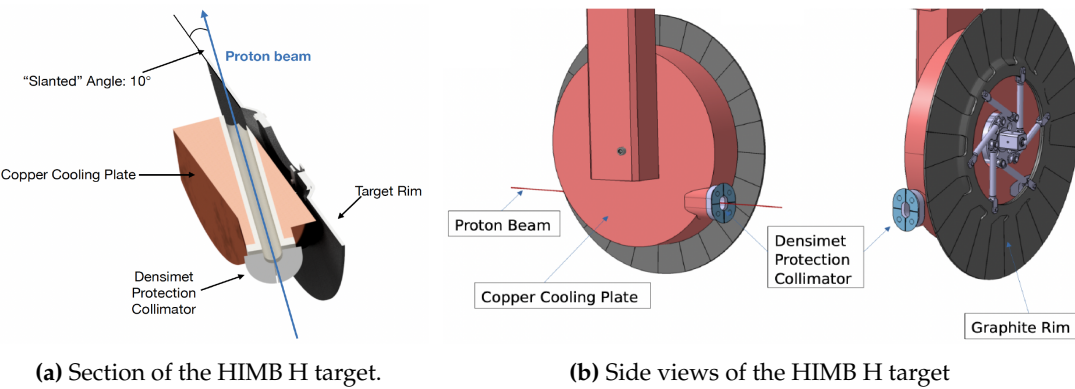


Fig. 1.16: Depiction of the target H for the HIMB project. The slanted target improves the production of surface muons. **a)** The proton beam impinges from the back side passing through a copper water-cooled shielding. **b)** The beam travels lower to avoid the rotating shaft.

Production using Advanced Cyclotron and Target Technologies project (IMPACT)[[impact](#)].

Production and collection

To increase the surface muon yield, the M target discussed in 1.5.2 will be substituted with target H, having a more slanted geometry. This new target, shown in Fig. 1.16, will be 20 mm thick in the proton direction, with a 10 deg slanting angle: surface muon yields comparable to a 40 mm thick non-slanted target. The protons will impinge below the rotation shaft (Fig. 1.16b), from the back of the target, in a copper water-cooled shielding (Fig. 1.16a). The target will fit in the remote-controlled exchange flask of target E for easier handling and maintenance.

When using solenoids to capture particles, the target is often completely enclosed in the solenoid aperture. This solution is not viable for HIMB because the proton beam is not stopped in the H target. The proposed solution, shown in Fig. 1.17, is to have two different NC solenoids (~ 0.45 T) sideways to the target.

The particles produced by the impact of the 590 MeV proton beam are: electrons, muons and pions. The momentum spectrum of the generated particle is shown in Fig. 1.18: the peak in the μ^+ spectrum is caused by surface muon production while, at higher energies, the muons come from pion decay in flight. This peak is not present for μ^- because stopped π^- undergoes nuclear capture and no muons are produced. In a similar fashion, the peak in positron around Michel edge is produced by stopped μ^+ . The HIMB project focuses on surface muons but the optimization are done to accept and transport momenta up to 80 MeV/c, while keeping the focus on 28 MeV/c.

Beamlines

HIMB will introduce two beamlines: MUH2 and MUH3. The peculiarity of these lines is the extensive use of solenoids. Solenoids achieve focus on both axes (wrt. quadrupoles) but usually, their usage is limited by the required magnetic fields. For the momentum of the surface muons ~ 0.45 T are sufficient and achievable with NC solenoids.

The MUH2 beamline is designed to deliver beams to fixed target experiments (e.g. Mu3e). It will be located at the left-hand side of the target station and its most important figure of merit for MUH2 is transmission. Two 40 deg bends are included in the beam trajectory with dipoles to

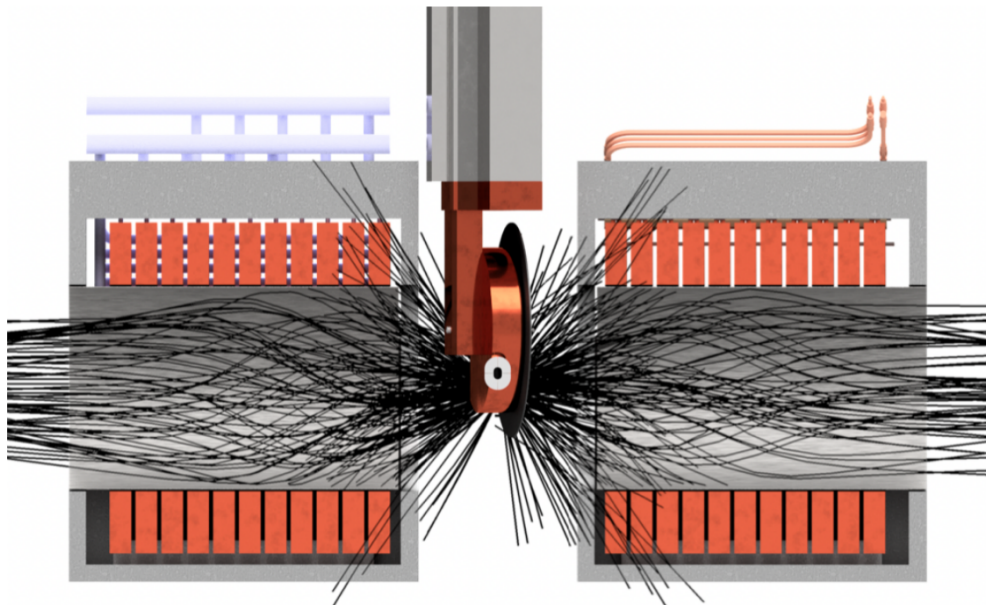


Fig. 1.17: HIMB will have two different NC solenoids sideways to the target. These are required to collect the produced muons and let the surviving proton beam continue toward the spallation SINQ setup.

avoid a direct line of sight to the target.

The model reported in the Conceptual Design Report (CDR) published in January 2022 [10] is able to deliver $1.22 \times 10^{10} \mu^+/\text{s}$ at a proton current of 2.4 mA at the entrance of the experimental area at the surface muon momentum. The beam spot size and the average polarization at the end of the channel are $\sigma_x = 40 \text{ mm}$, $\sigma_y = 42 \text{ mm}$, and $\varepsilon = 0.88$. Interesting to note that a double Wien filter scheme is currently under study to keep the positron contamination under control.

The MUH3 beamline, on the right-hand side of the target station, aims at delivering muon beams for muon spin rotation spectroscopy (μSR). For these applications, $10^{10} \mu/\text{s}$ is not required and part of the beamline follows a more standard approach with quadrupoles. From simulations, while the solenoid section delivers more than $10^{10} \mu/\text{s}$, the rate drops to $3 \times 10^8 \mu/\text{s}$ at 15 MeV and $6 \times 10^6 \mu/\text{s}$ at 10 MeV when reaching the two experimental area. The expected beam spots and polarization are $\sigma_x = 40 \text{ mm}$, $\sigma_y = 42 \text{ mm}$, and $\varepsilon \gtrsim 0.95$.

1.6 Proton Ionization Facility

Another interesting facility at PSI is the Proton Ionization Facility (PIF) [52][53]. This was designed, in conjunction with the European Space Agency, to be a user-friendly testing ground for spacecraft components. The deteriorating effect that high-energy protons can have on semiconductors is a key aspect of the correct functioning of spacecraft in the space environment. Depending on the orbit and the duration of the flight the exposure to this hazard can vary and having reproducible test grounds is cardinal during the design phase. The original goals of this facility:

- Radiation hardness of the new electronic products
- Single Event Upsets (SEU) and Latch-ups (SEL) of electronic components
- Properties of radiation monitors for space and laboratory applications
- Basic mechanics of radiation effects in semiconductors

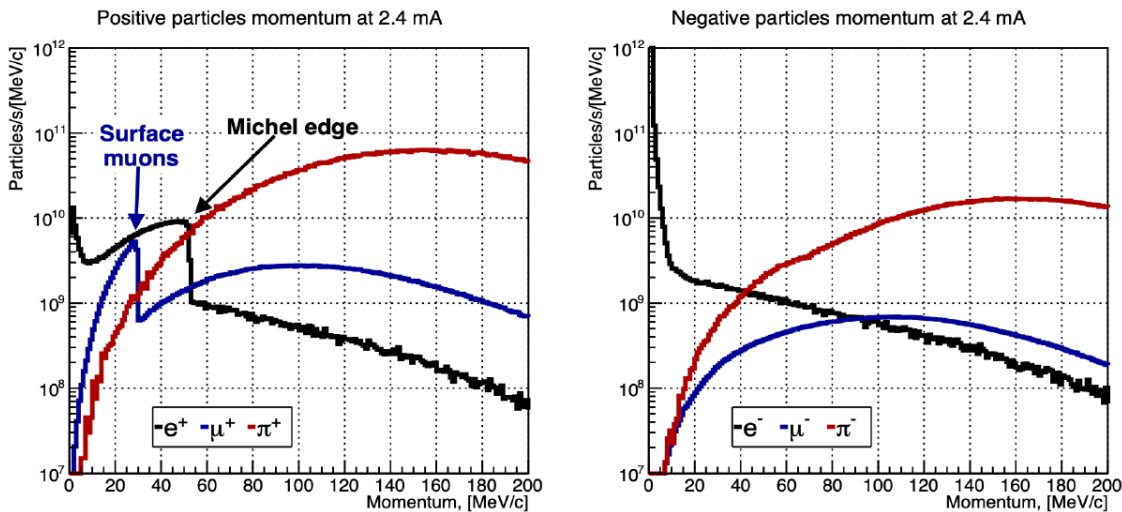


Fig. 1.18: Momentum spectrum for positive and negative e , μ , π produced at the HIMB H target for a proton current of 2.4 mA.

- Space radiation environment by on-earth simulations

Given the broad range of energy and intensities of the facility, alongside ESA many other users apply for beamtime at PIF within the accelerator communities, such as CERN, but also external laboratories, industries, and universities. During the daytime, the beam is usually reserved for biomedical applications and these irradiation studies are done parasitically during the night and on weekends. Although only for a short period, I joined PIF and I had the opportunity to be a shifter. It was quite an interesting experience, allowing me to become acquainted with a different setup and to see a different aspect of the research in particle physics. The usual shift would consist in tuning the beam to be suited to the user's needs and supporting during the data taking.

Bibliography for the introduction

- [1] Lorenzo Calibbi and Giovanni Signorelli. "Charged Lepton Flavour Violation: An Experimental and Theoretical Introduction". In: *Riv. Nuovo Cim.* 41.2 (2018), pp. 71–174. DOI: 10.1393/ncr/i2018-10144-0. arXiv: 1709.00294 [hep-ph].
- [2] Adrian Signer, Klaus Kirch, and Cyrus Hoffman. "Review of Particle Physics at PSI". In: *SciPost Physics Proceedings* (Sept. 2021). DOI: 10.21468/SciPostPhysProc.5.
- [3] M. Raidal et al. "Flavour physics of leptons and dipole moments". In: *Eur. Phys. J. C* 57 (2008). Ed. by R. Fleischer, T. Hurth, and M. L. Mangano, pp. 13–182. DOI: 10.1140/epjc/s10052-008-0715-2. arXiv: 0801.1826 [hep-ph].
- [4] F. J. M. Farley et al. "A New method of measuring electric dipole moments in storage rings". In: *Phys. Rev. Lett.* 93 (2004), p. 052001. DOI: 10.1103/PhysRevLett.93.052001. arXiv: hep-ex/0307006.
- [5] Maxim Pospelov and Adam Ritz. "Electric dipole moments as probes of new physics". In: *Annals of Physics* 318.1 (2005). Special Issue, pp. 119–169. ISSN: 0003-4916. DOI: <https://doi.org/10.1016/j.aop.2005.04.002>. URL: <https://www.sciencedirect.com/science/article/pii/S0003491605000539>.
- [6] A.M. Baldini et al. "Search for the lepton flavour violating decay $\mu^+ \rightarrow e^+\gamma$ with the full dataset of the MEG experiment". In: *Eur. Phys. J. C* 76.8 (2016), p. 434. DOI: 10.1140/epjc/s10052-016-4271-x. arXiv: 1605.05081 [hep-ex].
- [7] Wilhelm H. Bertl et al. "Search for the Decay $\mu^+ \rightarrow e^+e^+e^-$ ". In: *Nucl. Phys. B* 260 (1985), pp. 1–31. DOI: 10.1016/0550-3213(85)90308-6.
- [8] Wilhelm H. Bertl et al. "A Search for muon to electron conversion in muonic gold". In: *Eur. Phys. J. C* 47 (2006), pp. 337–346. DOI: 10.1140/epjc/s2006-02582-x.
- [9] L. Willmann et al. "New bounds from searching for muonium to anti-muonium conversion". In: *Phys. Rev. Lett.* 82 (1999), pp. 49–52. DOI: 10.1103/PhysRevLett.82.49. arXiv: hep-ex/9807011.
- [10] B. Aubert, Y. Karyotakis, et al. "Searches for Lepton Flavor Violation in the Decays $\tau^\pm \rightarrow e \pm \gamma$ and $\tau^\pm \rightarrow \mu^\pm \gamma$ ". In: *Phys. Rev. Lett.* 104 (2 Jan. 2010), p. 021802. DOI: 10.1103/PhysRevLett.104.021802. URL: <https://link.aps.org/doi/10.1103/PhysRevLett.104.021802>.
- [11] K. Hayasaka et al. "Search for Lepton Flavor Violating Tau Decays into Three Leptons with 719 Million Produced Tau-Tau- Pairs". In: *Phys. Lett. B* 687 (2010), pp. 139–143. DOI: 10.1016/j.physletb.2010.03.037. arXiv: 1001.3221 [hep-ex].

- [12] E. Abouzaid et al. "Search for lepton flavor violating decays of the neutral kaon". In: *Phys. Rev. Lett.* 100 (2008), p. 131803. DOI: 10.1103/PhysRevLett.100.131803. arXiv: 0711.3472 [hep-ex].
- [13] D. Ambrose et al. "New limit on muon and electron lepton number violation from $K^0(L) \rightarrow \mu\mu e^- e^-$ decay". In: *Phys. Rev. Lett.* 81 (1998), pp. 5734–5737. DOI: 10.1103/PhysRevLett.81.5734. arXiv: hep-ex/9811038.
- [14] Aleksey Sher et al. "An Improved upper limit on the decay $K^+ \rightarrow \pi^+ \mu^+ e^-$ ". In: *Phys. Rev. D* 72 (2005), p. 012005. DOI: 10.1103/PhysRevD.72.012005. arXiv: hep-ex/0502020.
- [15] Georges Aad et al. "Search for the lepton flavor violating decay $Z \rightarrow e\mu$ in pp collisions at \sqrt{s} TeV with the ATLAS detector". In: *Phys. Rev. D* 90.7 (2014), p. 072010. DOI: 10.1103/PhysRevD.90.072010. arXiv: 1408.5774 [hep-ex].
- [16] R. Akers et al. "A Search for lepton flavor violating Z^0 decays". In: *Z. Phys. C* 67 (1995) () .
- [17] Wilhelm H. Bertl et al. "A Search for muon to electron conversion in muonic gold". In: *Eur. Phys. J. C* 47 (2006), pp. 337–346. DOI: 10.1140/epjc/s2006-02582-x.
- [18] A.M. Baldini et al. "MEG Upgrade Proposal". In: (Jan. 2013). arXiv: 1301.7225 [physics.ins-det].
- [19] A.M. Baldini et al. "The design of the MEG II experiment". In: *Eur. Phys. J. C* 78.5 (2018), p. 380. DOI: 10.1140/epjc/s10052-018-5845-6. arXiv: 1801.04688 [physics.ins-det].
- [20] Angela Papa. "Towards a new generation of Charged Lepton Flavour Violation searches at the Paul Scherrer Institut: The MEG upgrade and the Mu3e experiment". In: *EPJ Web Conf.* 234 (2020). Ed. by G. D'Ambrosio et al., p. 01011. DOI: 10.1051/epjconf/202023401011.
- [21] Niklaus Berger. "The Mu3e Experiment". In: *Nucl. Phys. B Proc. Suppl.* 248-250 (2014). Ed. by Francesco Grancagnolo and Marco Panareo, pp. 35–40. DOI: 10.1016/j.nuclphysbps.2014.02.007.
- [22] Ann-Kathrin Perrevoort. "Status of the Mu3e Experiment at PSI". In: *EPJ Web Conf.* 118 (2016). Ed. by G. D'Ambrosio et al., p. 01028. DOI: 10.1051/epjconf/201611801028. arXiv: 1605.02906 [physics.ins-det].
- [23] R.M. Carey et al. "Proposal to search for $\mu^- N \rightarrow e^- N$ with a single event sensitivity below 10^{-16} ". In: (Oct. 2008). DOI: 10.2172/952028.
- [24] L. Bartoszek et al. "Mu2e Technical Design Report". In: (Oct. 2014). DOI: 10.2172/1172555. arXiv: 1501.05241 [physics.ins-det].
- [25] Y.G. Cui et al. "Conceptual design report for experimental search for lepton flavor violating mu- - e- conversion at sensitivity of $10^{**(-16)}$ with a slow-extracted bunched proton beam (COMET)". In: (June 2009).
- [26] R. Akhmetshin et al. "Letter of Intent for Phase-I of the COMET Experiment at J-PARC". In: (). URL: http://192.153.106.200/researcher/Hadron/en/pac_1203/pdf/COMET-PhaseI-LoI.pdf.
- [27] R. Akhmetshin et al. "Experimental Proposal for Phase-I of the COMET Experiment at J-PARC." In: (). URL: https://j-parc.jp/researcher/Hadron/en/pac_1207/pdf/E21_2012-10.pdf.

- [28] R. Abramishvili et al. “COMET Phase-I Technical Design Report”. In: *PTEP* 2020.3 (2020), p. 033C01. DOI: 10.1093/ptep/ptz125. arXiv: 1812.09018 [physics.ins-det].
- [29] Marco Chiappini. “The construction and commissioning of the ultra low mass MEG II drift chamber for the search of the $\mu^+ \rightarrow e^+ \gamma$ decay at branching ratios below 10^{-13} ”. PhD thesis. Pisa U., 2019.
- [30] A. Blondel et al. “Research Proposal for an Experiment to Search for the Decay $\mu \rightarrow eee$ ”. In: (Jan. 2013). arXiv: 1301.6113 [physics.ins-det].
- [31] F. Abusalma et al. “Expression of Interest for Evolution of the Mu2e Experiment”. In: (Feb. 2018). arXiv: 1802.02599 [physics.ins-det].
- [32] David Neuffer. “Mu2e-II Injection from PIP-II”. In: (Apr. 2018). DOI: 10.2172/1437287.
- [33] M.G. Catanesi et al. “Large-angle production of charged pions with 3-12.9-GeV/c incident protons on nuclear targets”. In: *Phys. Rev. C* 77 (2008), p. 055207. DOI: 10.1103/PhysRevC.77.055207. arXiv: 0805.2871 [hep-ex].
- [34] Andrew Williams John Edmonds. “An Estimate of the Hadron Production Uncertainty and a Measurement of the Rate of Proton Emission after Nuclear Muon Capture for the COMET Experiment”. PhD thesis. U. Coll. London, 2015.
- [35] Benjamin Edward Krikler. “Update on the AlCap Experiment”. In: *17th International Workshop on Neutrino Factories and Future Neutrino Facilities*. 2015, pp. 408–417.
- [36] Andrew Edmonds. “Latest Updates from the AlCap Experiment”. In: *13th Conference on the Intersections of Particle and Nuclear Physics*. Sept. 2018. arXiv: 1809.10122 [physics.ins-det].
- [37] C. Abel et al. “Measurement of the Permanent Electric Dipole Moment of the Neutron”. In: *Phys. Rev. Lett.* 124 (8 Feb. 2020), p. 081803. DOI: 10.1103/PhysRevLett.124.081803. URL: <https://link.aps.org/doi/10.1103/PhysRevLett.124.081803>.
- [38] V. Andreev et al. “Improved limit on the electric dipole moment of the electron”. In: *Nature* 562.7727 (2018), pp. 355–360. DOI: 10.1038/s41586-018-0599-8.
- [39] Yohei Ema, Ting Gao, and Maxim Pospelov. “Improved Indirect Limits on Muon Electric Dipole Moment”. In: *Phys. Rev. Lett.* 128.13 (2022), p. 131803. DOI: 10.1103/PhysRevLett.128.131803. arXiv: 2108.05398 [hep-ph].
- [40] G. W. Bennett et al. “An Improved Limit on the Muon Electric Dipole Moment”. In: *Phys. Rev. D* 80 (2009), p. 052008. DOI: 10.1103/PhysRevD.80.052008. arXiv: 0811.1207 [hep-ex].
- [41] N. J. Ayres et al. “The design of the n2EDM experiment”. In: *The European Physical Journal C* 81.6 (June 2021). DOI: 10.1140/epjc/s10052-021-09298-z. URL: <https://doi.org/10.1140/epjc/s10052-021-09298-z>.
- [42] Norman F. Ramsey. “A Molecular Beam Resonance Method with Separated Oscillating Fields”. In: *Phys. Rev.* 78 (6 June 1950), pp. 695–699. DOI: 10.1103/PhysRev.78.695. URL: <https://link.aps.org/doi/10.1103/PhysRev.78.695>.
- [43] S. Eckel, A. O. Sushkov, and S. K. Lamoreaux. “Limit on the Electron Electric Dipole Moment Using Paramagnetic Ferroelectric $\text{Eu}_{0.5}\text{Ba}_{0.5}\text{TiO}_3$ ”. In: *Phys. Rev. Lett.* 109 (19 Nov. 2012), p. 193003. DOI: 10.1103/PhysRevLett.109.193003. URL: <https://link.aps.org/doi/10.1103/PhysRevLett.109.193003>.

- [44] Y. J. Kim et al. "New Experimental Limit on the Electric Dipole Moment of the Electron in a Paramagnetic Insulator". In: *Phys. Rev. D* 91.10 (2015), p. 102004. DOI: 10.1103/PhysRevD.91.102004. arXiv: 1104.4391 [nucl-ex].
- [45] V. V. Flambaum, I. B. Khriplovich, and O. P. Sushkov. "On the Possibility to Study P Odd and T Odd Nuclear Forces in Atomic and Molecular Experiments". In: *Sov. Phys. JETP* 60 (1984), p. 873.
- [46] M. M. Gordon. "The longitudinal space charge effect and energy resolution". In: *Conf. Proc. C* 690917 (1969), pp. 305–317.
- [47] E. Pozdeyev et al. "Longitudinal beam dynamics studies with space charge in small isochronous ring". In: *Phys. Rev. ST Accel. Beams* 12 (2009), p. 054202. DOI: 10.1103/PhysRevSTAB.12.054202.
- [48] C. Baumgarten. "Transverse-Longitudinal Coupling by Space Charge in Cyclotrons". In: *Phys. Rev. ST Accel. Beams* 14 (2011), p. 114201. DOI: 10.1103/PhysRevSTAB.14.114201. arXiv: 1109.1996 [physics.acc-ph].
- [49] W. Joho. "High Intensity Problems in Cyclotrons". In: *9th International Conference on Cyclotrons and their Applications*. 1982, EI03.
- [50] M. Aiba et al. "Science Case for the new High-Intensity Muon Beams HIMB at PSI". In: (Nov. 2021). arXiv: 2111.05788 [hep-ex].
- [51] Giovanni Dal Maso et al. "Future facilities at PSI, the High-Intensity Muon Beams (HIMB) project". In: *EPJ Web Conf.* 282 (2023), p. 01012. DOI: 10.1051/epjconf/202328201012.
- [52] Wojtek Hajdas et al. "The Proton Irradiation Facility at the Paul Scherrer Institute". In: *Nuclear Instruments and Methods in Physics Research Section B: Beam Interactions with Materials and Atoms* 113.1 (1996). Accelerators in Applied Research and Technology, pp. 54–58. ISSN: 0168-583X. DOI: [https://doi.org/10.1016/0168-583X\(95\)01327-X](https://doi.org/10.1016/0168-583X(95)01327-X). URL: <https://www.sciencedirect.com/science/article/pii/0168583X9501327X>.
- [53] Wojtek Hajdas et al. "Proton Irradiation Facility and Space Radiation Monitoring at the Paul Scherrer Institute". In: *Physica medica : PM : an international journal devoted to the applications of physics to medicine and biology : official journal of the Italian Association of Biomedical Physics (AIFB)* 17 Suppl 1 (Feb. 2001), pp. 119–23.

Part I

muEDM

Chapter 2

muEDM

This chapter is an introduction to the muEDM experiment. After describing in some detail the spin dynamics, a reminder on the EDM searches for the different particles will follow. We will then outline the measuring principle of the experiment, the frozen spin technique, and deep dive into the current status of the experiment. The study of systematic uncertainties will close this chapter. As always, the early stage of the experiment means the rate of changes and improvement is outstanding. This my attempt to an up-to-date description but some details might be already outdated.

2.1 Electric Dipole Moment

As introduced in 1.3.5, the Hamiltonian describing the spin dynamics is:

$$\hat{H} = -\mu \hat{\sigma} \cdot \mathbf{B} - d \hat{\sigma} \cdot \mathbf{E}$$

We then saw that, when considering a combination of magnetic and electric fields and a moving particle it is useful to introduce the polarization vector $\boldsymbol{\Pi} = \mathbf{s}/s$ and the Thomas precession $\boldsymbol{\Omega}_0$:

$$\frac{d\boldsymbol{\Pi}}{dt} = \boldsymbol{\Omega}_0 \times \boldsymbol{\Pi}, \quad \boldsymbol{\Omega}_0 = -\frac{e}{m\gamma} \left[(1 + \gamma a) \mathbf{B} - \frac{a\gamma^2}{\gamma + 1} (\boldsymbol{\beta} \cdot \mathbf{B}) \boldsymbol{\beta} - \gamma \left(a + \frac{1}{\gamma + 1} \right) \frac{\boldsymbol{\beta} \times \mathbf{E}}{c} \right]$$

With no electrical field parallel to the momentum and with $\boldsymbol{\Omega}_c$ the cyclotron frequency, the relative spin precession of a muon in a storage ring is described by (T-BMT [**miss-59**]):

$$\begin{aligned} \boldsymbol{\Omega} = \boldsymbol{\Omega}_0 - \boldsymbol{\Omega}_c &= \underbrace{\frac{q}{m} \left[a \mathbf{B} - \frac{a\gamma}{\gamma + 1} (\boldsymbol{\beta} \cdot \mathbf{B}) \boldsymbol{\beta} - \left(a + \frac{1}{1 - \gamma^2} \right) \frac{\boldsymbol{\beta} \times \mathbf{E}}{c} \right]}_{\text{Anomalous precession, } \omega_a = \omega_L - \omega_c} \\ &\quad + \underbrace{\frac{\eta q}{2m} \left[\boldsymbol{\beta} \times \mathbf{B} + \frac{\mathbf{E}}{c} - \frac{\gamma c}{\gamma + 1} (\boldsymbol{\beta} \cdot \mathbf{E}) \boldsymbol{\beta} \right]}_{\text{Interaction of EDM and relativistic } \mathbf{E}, \omega_a} \end{aligned} \quad (2.1)$$

The second term describes the precession due to the EDM coupling to the relativistic \mathbf{E} , perpendicular to the \mathbf{B} in which the particle is moving. In the presence of a muon EDM the plane would be tilted and a vertical precession ($\omega_e \perp \mathbf{B}$), shifted by $\pi/2$ to the horizontal anomalous precession, would become observable.

2.1.1 Symmetry violation

In physics, there are three cardinal discrete symmetries: Charge (C), Parity (P), and Time (T). P and T are related to the invariance under spatial and temporal reversal while C is the invariance for particle \leftrightarrow antiparticle exchange. While the magnetic field and the spin are *pseudo*-vectors under P and vectors under T, the electric field behaves in the opposite way. The implication of this difference is that EDM and MDM behave differently under C, P, and T:

$$MDM : \begin{cases} P(-\mu\hat{\sigma} \cdot B) = -\mu P(\hat{\sigma}) \cdot P(B) = -\mu(+\hat{\sigma}) \cdot (+B) = -\mu\hat{\sigma} \cdot B \\ T(-\mu\hat{\sigma} \cdot B) = -\mu T(\hat{\sigma}) \cdot T(B) = -\mu(-\hat{\sigma}) \cdot (-B) = -\mu\hat{\sigma} \cdot B \end{cases} \quad (2.2)$$

$$EDM : \begin{cases} P(-d\hat{\sigma} \cdot E) = -dP(\hat{\sigma}) \cdot P(E) = -d(+\hat{\sigma}) \cdot (-E) = +d\hat{\sigma} \cdot E \\ T(-d\hat{\sigma} \cdot E) = -dT(\hat{\sigma}) \cdot T(E) = -d(-\hat{\sigma}) \cdot (+E) = +d\hat{\sigma} \cdot E \end{cases} \quad (2.3)$$

In light of the CPT theorem, the breaking of the T symmetry implies the breaking of CP.

2.1.2 Current limits on EDM

As discussed in 1.4.2, the last decades saw a continuous effort to measure the EDM of different particles. There the experiments setting the current limits were discussed but we report in Tab. 2.1 the results to aid the reader. It is important to note there are two limits for μ : one obtained by rescaling the limit on d_e , obtaining an *indirect limit*; one, less stringent, is a *direct limit* (*).

Experiment	Particle	EDM limit in ecm
nEDM [1]	n	0.18×10^{-25}
ACME [2]	e	1.1×10^{-29}
Indirect [3]	μ	$0.19 \times 10^{-19} *$
g-2 [4]	μ	1.8×10^{-19}

Fig. 2.1: Sumary of the current limits on the EDM for neutron electron and muon.

2.1.3 The *frozen spin* technique

As illustrated in [1, 9], with the appropriate choice of electric field and having p , B and E forming an orthogonal basis, the anomalous precession term in eq. 2.1 can be set to zero.

$$aB = \left(a - \frac{1}{\gamma^2 - 1} \right) \frac{\beta \times E}{c} \quad (2.4)$$

In this situation the relative angle between p and spin remains unchanged if $\eta = 0$, hence 'frozen'. In the presence of an EDM the change in polarization would then follow

$$\frac{d\Pi}{dt} = \omega_e \times \Pi, \quad \omega_e = \frac{\eta q}{2m} \left(\beta \times B + \frac{E_f}{c} \right) = \frac{2d_\mu}{\hbar} (\beta c \times B + E_f) \quad (2.5)$$

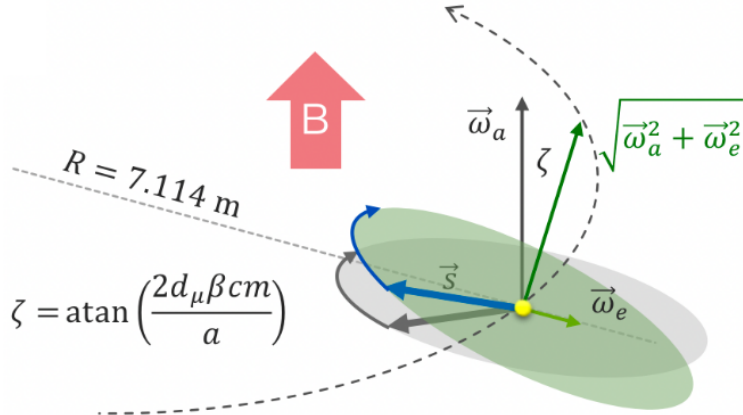


Fig. 2.1

The net result of the EDM is then a vertical build-up of the polarization given by Eq. 2.6 and illustrated by the sketch in Fig. 2.1.

$$|\Pi(t)| = P(t) = P_0 \sin(\omega_e t) \approx P_0 \omega_e t \approx 2P_0 \frac{d_\mu}{\hbar} \frac{E_f}{a\gamma^2} t \quad (2.6)$$

At this point, we would like to evaluate the sensitivity to this vertical build-up and this is dependent on the experimental setup investigated.

$$\frac{dP}{dd_\mu} = \frac{2P_0 E_f t}{a\hbar\gamma^2} \quad (2.7)$$

$$\sigma(d_\mu) = \frac{a\hbar\gamma}{2P_0 E_f \sqrt{N} \tau_\mu A} \quad (2.8)$$

2.2 The muEDM experiment

2.3 The precursor

The task at hand is quite complex and for this reason, the aim is to first have a working prototype to demonstrate the measuring principles, the achieved control on the different sources of uncertainties and the correct working of the different subdetectors.

2.3.1 Superconducting injection channel

To allow the incoming muons to enter the magnet without being reflected or deviated by fringing fields an injection channel is needed. For reasons that will be discussed in the section dedicated to the systematics (see Sec. 2.4), we will actually require two symmetrical injections. The idea is to use a superconducting pipe: the fields around the pipe will generate Eddy currents which will, in turn, generate an opposite field inside the pipe, canceling the first. Clearly, the development of such a system is not trivial, and a precise study of the different shapes and materials is required. The hope would be to find a suitable *high-temperature* superconductor.

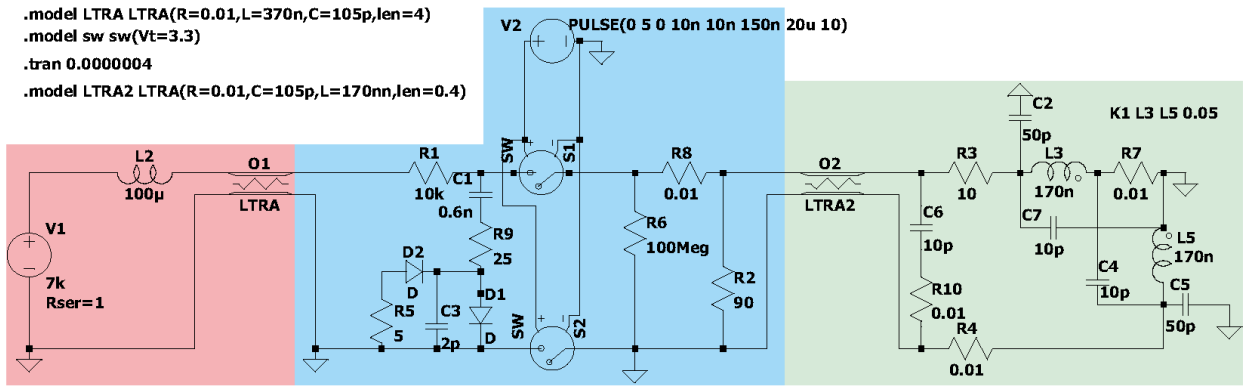


Fig. 2.2: LTSPICE simulation for the kicker circuit.

2.3.2 Entrance detector

After a muon successfully enters the experiment it would spiral to the other side of the magnet. To store it a magnetic kick is necessary. How to produce this kick is going to be explained in the next paragraph but in either case, this system needs to be triggered. To detect the muon entering the system a thin scintillator can be used. This needs to be thick enough to produce sufficient light but thin enough not to deflect the particle from the design orbit. With a dedicated GEANT4 simulation¹, the amount of light exiting the different sides of the thin scintillator was studied as a function of muon and positron momenta. The results of the simulations and the dedicated beamtimes to develop this entrance detector will be discussed in Ch. 3, dedicated to this detector.

2.3.3 Muon tracking

Although during physics runs it is important to minimize the number of interactions of the muon along the path, it is a cardinal step to prove the muons are following the correct path. For this reason, a removable muon-tracking device is under development. The idea is to use TPC + GRIDPIX. [5]

2.3.4 Kicker

The prerequisite for the *frozen spin* is to first store the muon around the design orbit. This is achieved by applying a longitudinal kick, canceling the momentum component parallel to the magnetic field. The development of this element is non-trivial because of the stringent requirements on the strength, time scale, and residual effects of the kick. We started by looking into different shapes and types of coil as well as developing LTSPICE simulations of the generating circuit. The current version of the circuit is shown in Fig. 2.2.

2.3.5 Electrodes

After the muon has been successfully stored around the design orbit the next step is to apply a radial electric field. The strength of this field is going to modify the frequency of the g-2 precession, eventually *freezing* the spin (eq. 2.5) along the momentum direction. These electrodes need to

¹To be honest this was actually my first GEANT4 project and few iterations were needed.

be out of the muon orbit and with a minimal material budget to reduce the positron scattering. Dedicated simulations and prototyping have been developed also for this element.

2.3.6 Positron tracking

The development of the positron tracker has been a big part of my work in the collaboration. For this reason, an in-depth description will follow in a dedicated chapter while here we will just outline the basic idea. The project is to use two subsystems:

- A silicon pixel external tracker will be used to track precisely the transverse position of the positron. The aim of this sub-detector is to measure the g-2 precession to fine-tune the radial electric field to achieve the frozen-spin condition.
- An internal scintillating fiber detector with a comparable resolution on the transverse position will complement the silicon pixel with additional hits. The requirement is to have a better resolution on the longitudinal position of the hits to measure the EDM by looking at the pitch of the outgoing helical track.

2.4 Systematics

[6] [[muEDM:g-2:2008](#)] [7] [8] [9] [10] [11] [12]

2.5 Conclusions

Bibliography on muEDM

- [1] C. Abel et al. "Measurement of the Permanent Electric Dipole Moment of the Neutron". In: *Phys. Rev. Lett.* 124 (8 Feb. 2020), p. 081803. DOI: 10.1103/PhysRevLett.124.081803. URL: <https://link.aps.org/doi/10.1103/PhysRevLett.124.081803>.
- [2] V. Andreev et al. "Improved limit on the electric dipole moment of the electron". In: *Nature* 562.7727 (2018), pp. 355–360. DOI: 10.1038/s41586-018-0599-8.
- [3] Yohei Ema, Ting Gao, and Maxim Pospelov. "Improved Indirect Limits on Muon Electric Dipole Moment". In: *Phys. Rev. Lett.* 128.13 (2022), p. 131803. DOI: 10.1103/PhysRevLett.128.131803. arXiv: 2108.05398 [hep-ph].
- [4] G. W. Bennett et al. "An Improved Limit on the Muon Electric Dipole Moment". In: *Phys. Rev. D* 80 (2009), p. 052008. DOI: 10.1103/PhysRevD.80.052008. arXiv: 0811.1207 [hep-ex].
- [5] G. Cavoto et al. "Operating the GridPix detector with helium-isobutane gas mixtures for a high-precision, low-mass Time Projection Chamber". In: (May 2023). arXiv: 2305.03599 [physics.ins-det].
- [6] Yannis K. Semertzidis et al. "A sensitive search for a muon electric dipole moment". In: *AIP Conf. Proc.* 564.1 (2001). Ed. by G. Cantatore, pp. 263–268. DOI: 10.1063/1.1374993.
- [7] A. Adelmann et al. "Compact storage ring to search for the muon electric dipole moment". In: *J. Phys. G* 37 (2010), p. 085001. DOI: 10.1088/0954-3899/37/8/085001.
- [8] Hiromi Iinuma. "New approach to the muon g-2 and EDM experiment at J-PARC". In: *J. Phys. Conf. Ser.* 295 (2011). Ed. by Hans Stroher and Frank Rathmann, p. 012032. DOI: 10.1088/1742-6596/295/1/012032.
- [9] Hiromi Iinuma et al. "Three-dimensional spiral injection scheme for the g-2/EDM experiment at J-PARC". In: *Nucl. Instrum. Meth. A* 832 (2016), pp. 51–62. DOI: 10.1016/j.nima.2016.05.126.
- [10] A. Adelmann et al. "Search for a muon EDM using the frozen-spin technique". In: (Feb. 2021). arXiv: 2102.08838 [hep-ex].
- [11] Mikio Sakurai et al. "muEDM: Towards a search for the muon electric dipole moment at PSI using the frozen-spin technique". In: *24th International Symposium on Spin Physics*. Jan. 2022. arXiv: 2201.06561 [hep-ex].
- [12] Kim Siang Khaw et al. "Search for the muon electric dipole moment using frozen-spin technique at PSI". In: *PoS NuFact2021* (2022), p. 136. DOI: 10.22323/1.402.0136. arXiv: 2201.08729 [hep-ex].

Chapter 3

muEDM entrance detector

In the previous chapter, the muEDM experiment was introduced and the current status was described. In this, we will describe the simulations and beamtimes connected to the entrance detector of the experiment. We will start with the GEANT4 simulations of scintillation in thick and thin scintillation, moving then to the entrance detector and the ‘telescope’ used in the beamtime of 2022. We will then move to the different beamtimes, focusing on both the data collection and analysis.

3.1 GEANT4 simulations

3.1.1 Entrance system

3.1.2 Thin scintillators

3.1.3 Telescope and entrance detector

3.2 Beamtime 2021

This was the first muEDM beamtime I participated in. I took an active part in the setup and measurement and I followed the analysis of the data collected. This section relies on the Master Thesis of Tim Hume, part of the muEDM collaboration. This beamtime was designed to study the positron multiple scattering in different thin foils of the material expected to be viable solutions for the different parts of the experiment. On top of the material details, the aim was also to validate the scattering model used in the GEANT4 simulations for further reference. The setup was quite simple: a telescope of five silicon pixel sensors, three upstream and two downstream.

3.2.1 Description of the multiple scattering

Highland The Highland formula for multiple scattering is a parameterization for the width of the multiple scattering distribution. For a particle of charge z , momentum p traversing a thickness of x of a material with radiation length X_0 , the RMS of the gaussian distribution is estimated as:

$$\theta_0 = \frac{13.6 \text{ MeV}}{\beta pc} z \sqrt{\frac{x}{X_0}} \left(1 + 0.038 \ln\left(\frac{xz^2}{X_0 \beta^2}\right) \right) \quad (3.1)$$

Often, in the context of high particle physics, the projection on the directions orthogonal to the momentum are considered:

$$P(\theta_{x,y}) = \frac{1}{\theta_0 \sqrt{2\pi}} \exp\left(-\frac{\theta_{x,y}^2}{2\theta_0^2}\right) \quad (3.2)$$

GEANT4 The default parameterization of the multiple scattering in GEANT4 is the Urbán. This is based on a different description of the process, required because when evaluating the processes at each step of the simulation, meaning *within* the volume. This model describes the angular distribution of multiple scattering and samples it every interaction. The probability density of the angular distribution is usually indicated with $g(u)$ where $u = \cos \theta$ and the form is the following:

$$g(u) = \alpha + \begin{cases} \beta \exp(\gamma u) & \text{for } u_0 \leq u \leq 1 \\ \delta(1-u)^\epsilon & \text{for } -1 \leq u < u_0 \end{cases} \quad (3.3)$$

The parameter u_0 is the one used to transition between the central Gaussian-like distribution and the Rutherford-like tails at larger angles.

For the Highland formula, the PDG reports an accuracy of $\sim 10\%$ in the range $10^{-3} < x/X_0 < 10^2$ [1], meaning it is less reliable for thin targets for which $x/X_0 \sim \mathcal{O}(10^{-4})$. On the other hand, while GEANT4 results have been widely tested against experimental measurements, there is a lack of data to compare in the ranges we are interested in.

3.2.2 Data taking

The idea behind the data taking is quite simple: a study on the multiple scattering can be performed using a beam telescope, such as the one sketched in Fig 3.1, in which the two sides of the telescope are used to track the in/out-coming particles. The delicate point is to carefully take into account the scattering of the particles in the telescope itself. It is then needed to collect data without the sample to apply a deconvolution of the telescope response. The downstream part of the detector is not symmetrical to the upstream because only five sensors had the necessary performance. This made the tracking task more challenging, leading to wider distributions. The beamline used is the π E1, which provides π^\pm, μ^\pm, e^\pm in a momentum range 100 MeV to 500 MeV. Clearly, a good understanding of the beam is key in both data-taking and analysis. An example is the study of the beam changing the degrader's thickness, shown in Fig. 3.3. For brevity, the description of the electronics and DAQ system will be skipped.

Silicon Pixel Sensors The sensors used are the last iteration of the sensors of the *mu3e* experiment, the MuPix10. These are High Voltage Monolithic Active Pixel Sensors (HV-MAPS) with 250×256 pixels of dimensions $80 \mu\text{m} \times 80 \mu\text{m}$. The sensor itself is on a PCB used for delivering the required voltages. A second, larger, PCB is set below the first and is responsible for reading and transmitting the data to FPGA. These sensors have been developed to achieve excellent position and time resolutions ($100 \mu\text{m}$ and 20 ns) with efficiency of $\epsilon \approx 0.99$. The thickness of these sensors is $50 \mu\text{m}$ but this was the case for just the detector positioned after the samples. The others were $100 \mu\text{m}$, important to be considered during the analysis. The whole apparatus is shown in Fig. 3.2a

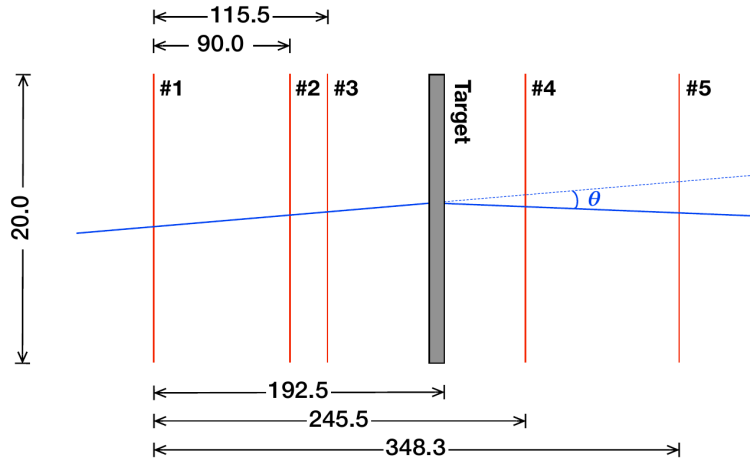
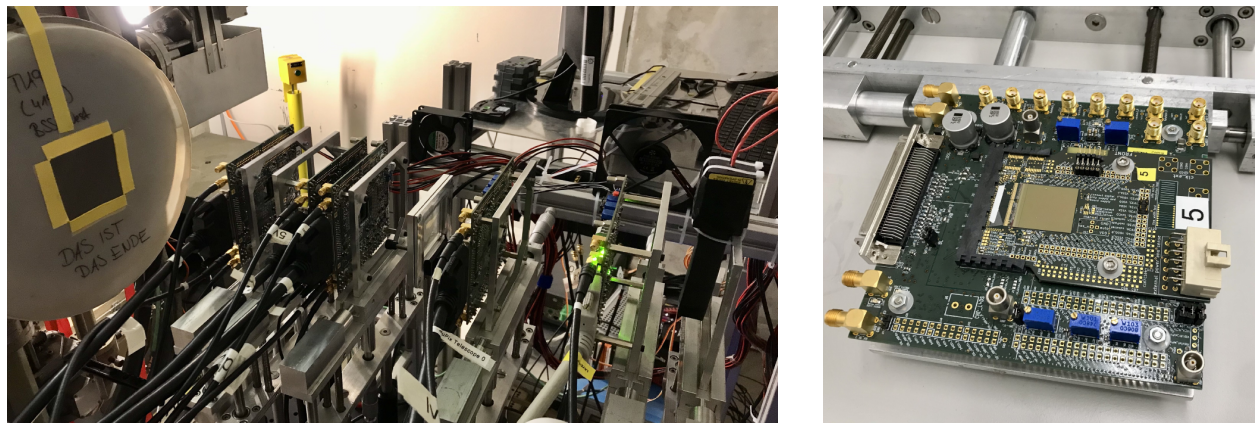


Fig. 3.1: Sketch of the telescope of Silicon Pixel Sensors used to study the multiple scattering in different materials. The samples are held in the position of the 'target'. In this sketch, the beam is coming from the left side.



(a) Picture of the setup for the beamtime of 2021. On the right, the scintillator was used as an external trigger, on the left, beam exit window.

(b) Picture of one of the MuPix10 mounted on the two PCBs.

Fig. 3.2: Picture of the setup and one of the MuPix10 (grey-colored square) mounted on the PCBs.

while a singular MuPix10 is shown in Fig. 3.2b.

3.2.3 Data analysis

Track selection Initial angular distributions obtained were broad due to noise in downstream sensors, making it difficult to distinguish noise from true hits. To address this, a filtering process was developed to select the track candidate with the least spatial separation between the intersections of upstream and downstream tracks on the plane of the sample. The expected angular distribution for particles passing through a material at normal incidence should be spatially symmetric and independent of chosen projection axes. Any deviation from this symmetry could indicate experimental, data processing, or analysis errors. To mitigate the effects the idea was to

Fig. 3.1: Table of the different materials, thicknesses, particles and momenta used.

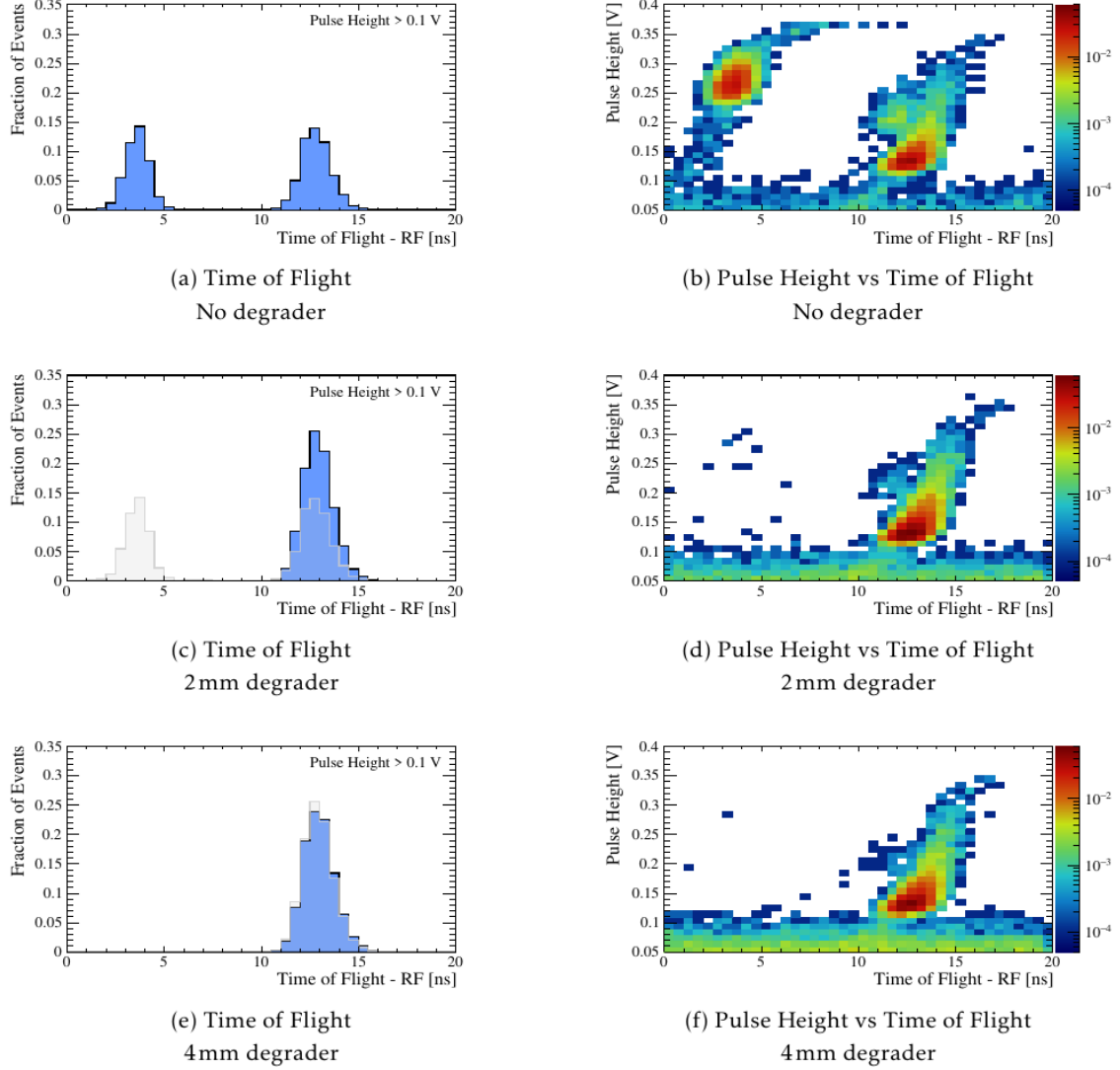


Fig. 3.3: Timing and the 2D plot for time and pulse height for 120 MeV/c particles. The three rows show what happens when inserting degraders of different thicknesses. With no degrader, the π peak is visible at lower TOF. When increasing the thickness, the contributions of π and μ decrease. It is important to note that the e and μ distribution overlap. In gray the distribution of the previous plot to make a comparison.

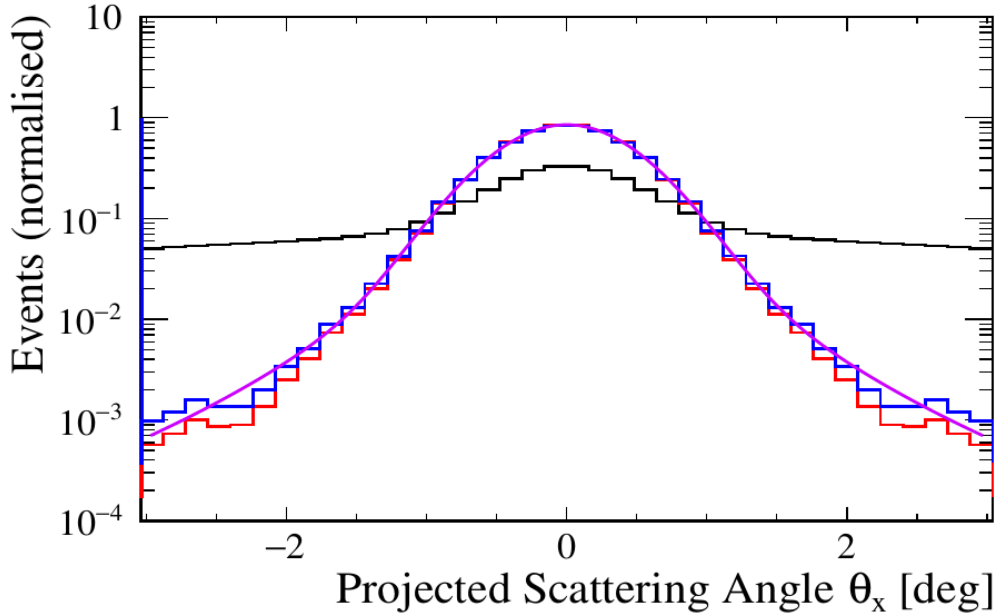


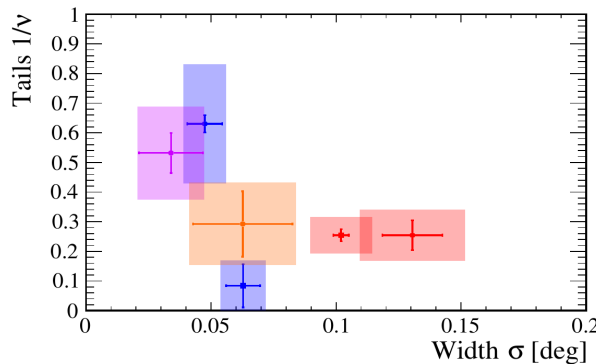
Fig. 3.4: The angular distributions show: the full distribution (black), the distribution after cuts in the distance at the sample’s plane (red), the distribution after acceptance correction (blue), and the fitted function for telescope characterization (violet).

combine distributions from multiple axes. In the initial distributions, the broad background can be attributed to false tracks generated by noise, poor fits, and some contribution of events with large angles of scattering in the telescope itself. This background was suppressed by enforcing a distance of 1 mm between the points at which the upstream and downstream tracks intersect the plane of the sample. Distributions before and after applying this filter are shown in black and red in Fig. 3.4. This distribution was then corrected for the geometric acceptance of the telescope.

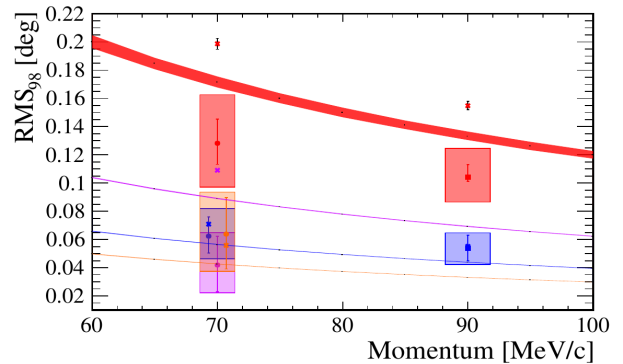
Acceptance The correction for the geometrical acceptance of the telescope was essential to accurately determine the tails of the angular distribution. To estimate the acceptance, for each upstream track identified, scattering angles were randomly assigned and added to a histogram, distinguishing instances within the acceptance of the most downstream sensor. The ratio of histograms yielded the average acceptance as a function of projected scattering angles. The acceptance correction was applied on a per-event basis, adjusting the scattering angles based on the acceptance value. An example of such correction is shown in blue in Fig. 3.4

Deconvolution The method of track selection and acceptance correction was applied to both runs with and without the sample. The distributions from these runs were then fitted. The process involved:

- Characterizing the telescope’s response without the sample using a weighted sum of a Gaussian distribution and a Student’s t distribution
- Convoluting the response function with the sample’s angular distribution, assumed to follow a single Student’s t distribution
- using the negative log-likelihood to determine the best-fit parameters for describing the measured distribution with the sample

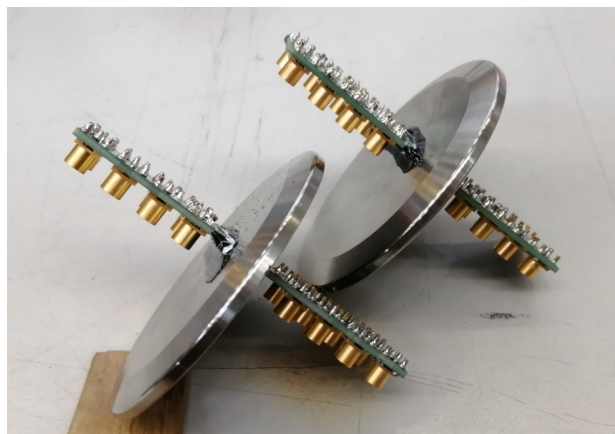


(a) Pokalon (orange), 17 μm Graphite (blue), 50 μm Graphite (violet), Silicon (red); circular markers for data at 70 MeV and squared at 90 MeV; error bars are the statistical uncertainties and the shaded area is the total uncertainties.

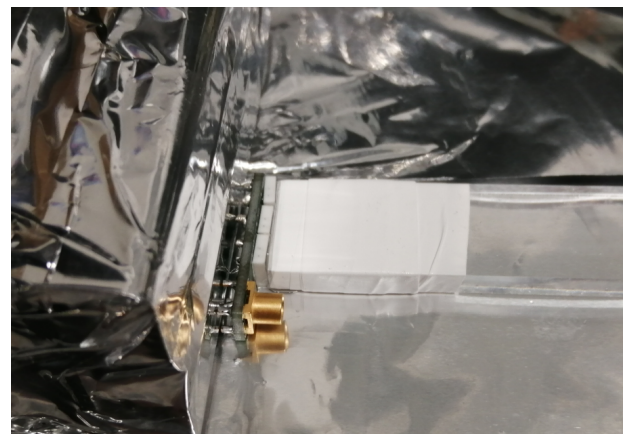


(b) Same color/shape coding as Fig. 3.5a and the predictions of the Highland formula are shown by lines of width representing the uncertainty in thickness.

Fig. 3.5: Results of the analysis of the different samples and confronted with predictions using the Highland formula and GEANT4. The details are not easy to read but the 'bring-home' message is that the results are somewhat in agreement and some improvement are planned on the analysis.



(a) Custom feed-throughs: PCB board, with soldered connectors, sealed with Stycast in a blind flange.



(b) A small PCB board with 3 SiPMs and one connector attached with optical cement to one of the scintillators.

Fig. 3.6: asd

3.2.4 Model evaluation and conclusions

This first beamtime aimed at testing the agreement between the Highland formula and the GEANT4 Urbán model for the multiple scattering in thin materials. The analysis of the data collected is still not finalized, but a rough agreement between data and models can be seen in Fig. 3.5. There are improvements that could be added to the analysis and/or to the simulation of the experimental setup, so updated results are expected in the following months.

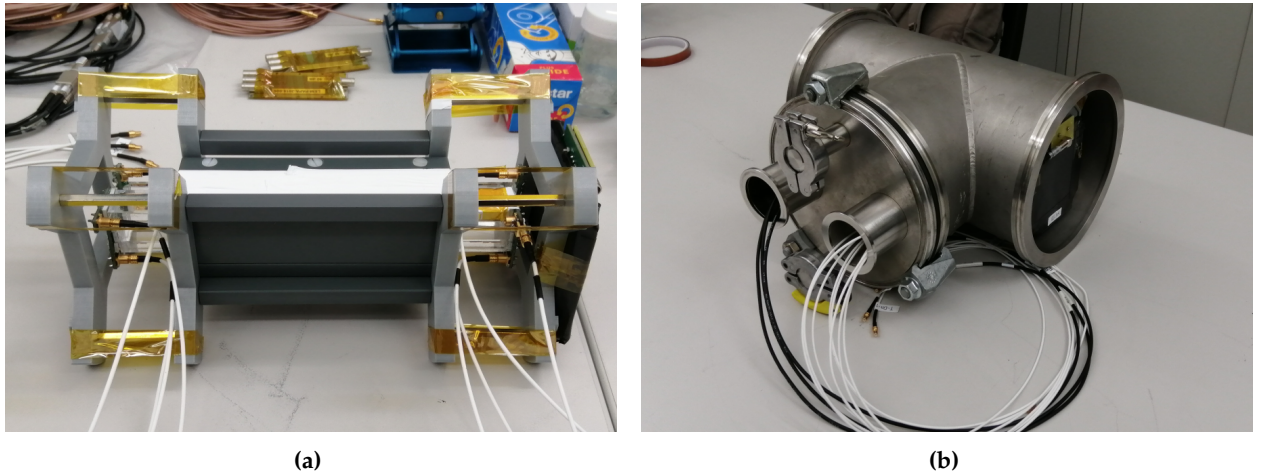


Fig. 3.7: asd

3.3 Beamtime 2022: Telescope and entrance detector

3.3.1 Construction

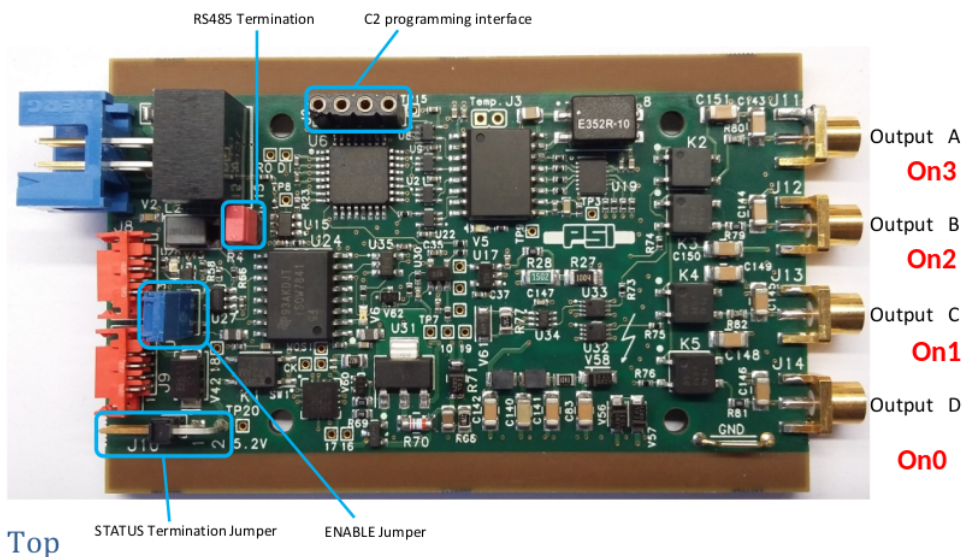
3.3.2 Data taking

3.3.3 Data analysis

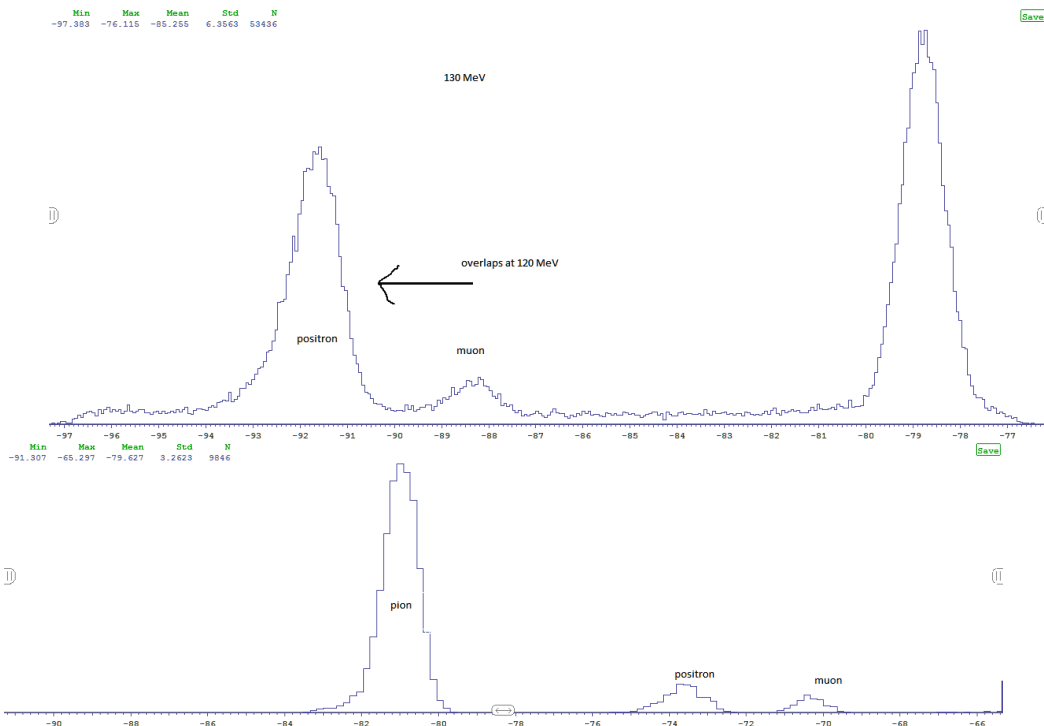
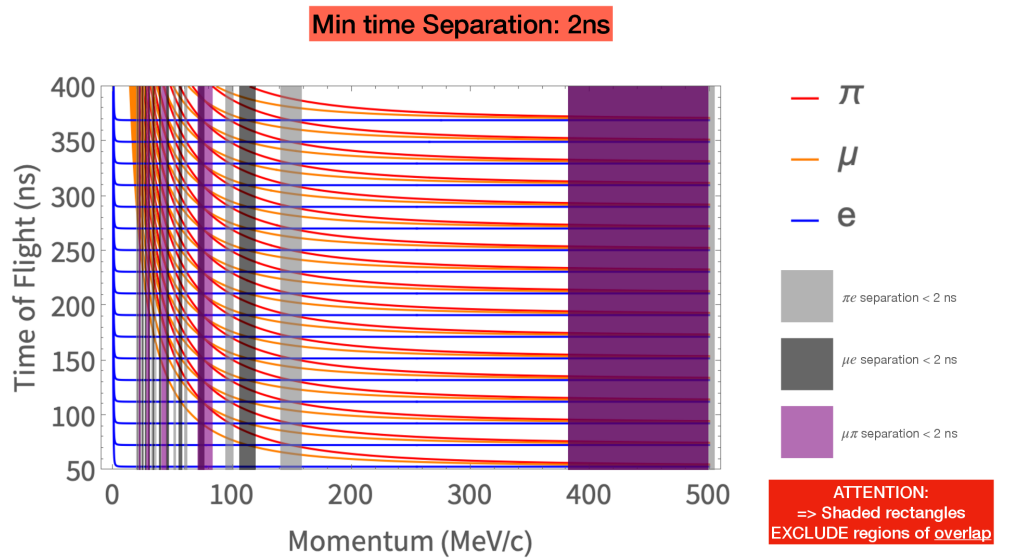
3.4 Beamtime 2023: Multi readout entrance

3.4.1 Data taking

3.4.2 Data analysis



3.4.3 Describe the beam



3.5 Conclusions

Bibliography on muEDM entrance detector

- [1] R. L. Workman et al. "Review of Particle Physics". In: *PTEP* 2022 (2022), p. 083C01. doi: 10.1093/ptep/ptac097.

Chapter 4

muEDM positron tracker

This chapter is an in-depth study on the development of the scintillating fiber part of the muEDM positron tracker. We will skip some preliminary studies and we will start with the description of the positron tracker which was included in the proposal of the experiment submitted to PSI at the end of 2022; we will move to the simulations done after that and the current design of this detector.

4.1 Design in the proposal 2022

The detector described in the proposal would satisfy the requirements for muEDM but comes with some limitations.

4.1.1 SciFi prototype

4.1.2 The barrel geometry

4.1.3 Issues

4.1.4 Alternatives

4.2 CHeT or CyFi

The first step in developing and prototyping the geometry chosen in the previous paragraph is to understand the requirements for this sub-detector and how the prospected resolutions compare to these. This scintillating fiber tracker will be used for position tracking and in particular is going to be complemented by silicon strips. The crucial information this system needs to provide is the longitudinal position of the particle with a good resolution: $\delta\ell \lesssim 1 \text{ mm}$.

4.2.1 Resolutions of crossed fibers ribbons

Let's consider a ribbon $3 \text{ cm} \times 15 \text{ cm}$ of squared fibers $250 \mu\text{m}$ running vertically. Assuming a 'perfect' readout, the resolution across the ribbon is given simply by the fibers' width while the resolution along the ribbon is extracted by reading the fibers on both sides. This second resolution is often quite worse than the previous. For practical purposes we will here assume $\delta_x = 1 \text{ mm}$; $\delta_y = 10 \text{ mm}$. Rotating the ribbon by an angle θ changes the projection of the resolutions on the \hat{x} ; \hat{y} axes and for this reason crossing two ribbons can improve the resolutions on

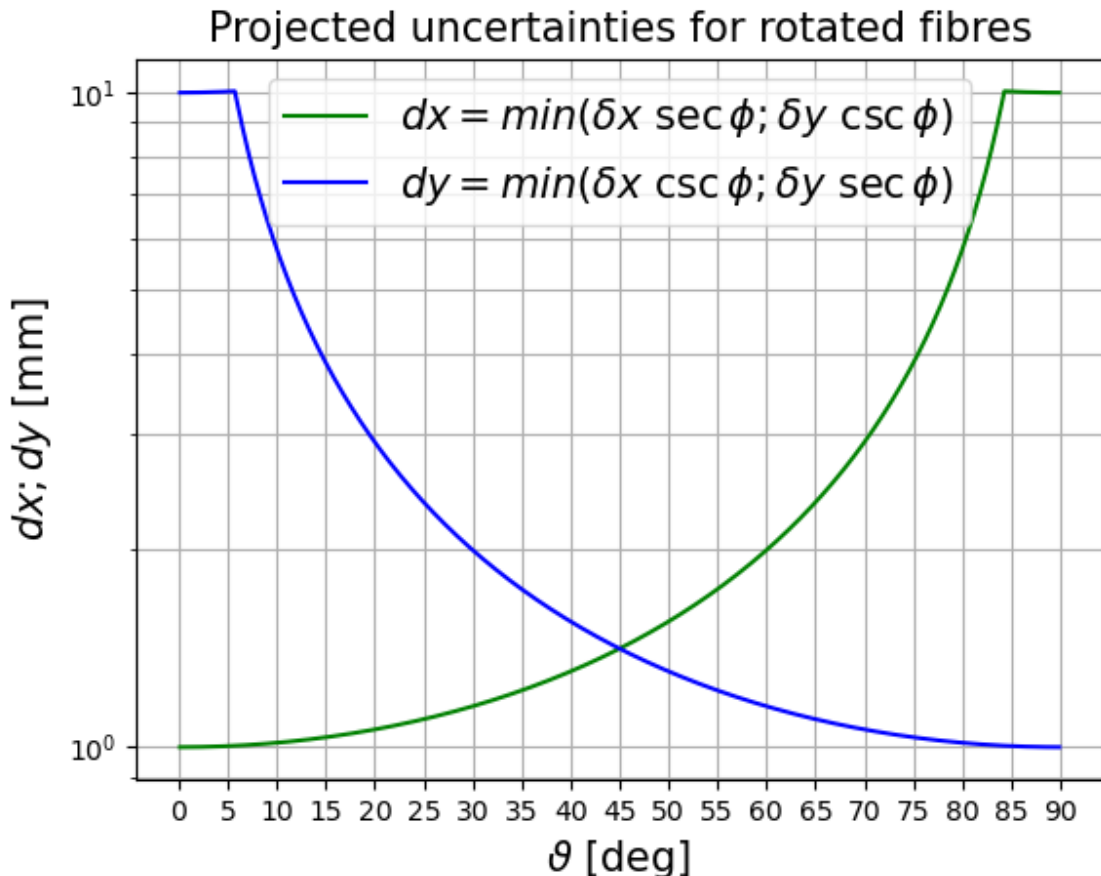


Fig. 4.1: Projection along the \hat{x} ; \hat{y} axes of the resolutions considering a ribbon of fibers rotated in different angles. The intrinsic resolutions are here assumed $\delta_x = 1$ mm; $\delta_y = 10$ mm.

the position of a crossing particle. When reading the ribbon on both sides the resolutions, as a function of θ , are given by the smaller between the projection of the two intrinsic resolutions.

$$\begin{cases} dx = \min(\delta_x \sec \theta; \delta_y \csc \theta) \\ dy = \min(\delta_x \csc \theta; \delta_y \sec \theta) \end{cases} \quad (4.1)$$

The relation between resolutions and the tilt angle is shown in fig. 4.4a.

4.2.2 Angle choices for the layers

When considering two layers the angles must be chosen to improve the overall resolution, which in practice means minimizing the uncertainty only on one axes per ribbon. Let's consider the different layouts in 4.2a and how they translate to resolutions in 4.2b. Clearly having the two ribbons at 90 deg along the axes is the best option but if we want to avoid having the readout on the plane of the muon orbit we need to consider less steep angles for the single ribbons. Options C and D are the possible solutions and, looking at the resolutions, D is actually the configuration minimizing the resolutions on both axes. At this point is important to notice an additional constraint, given by the cylindrical geometry: if two fibers cross multiple times when both are scintillating the position of the impinging particle is ill-defined. There is a 'real' crossing point but also additional 'ghosts'

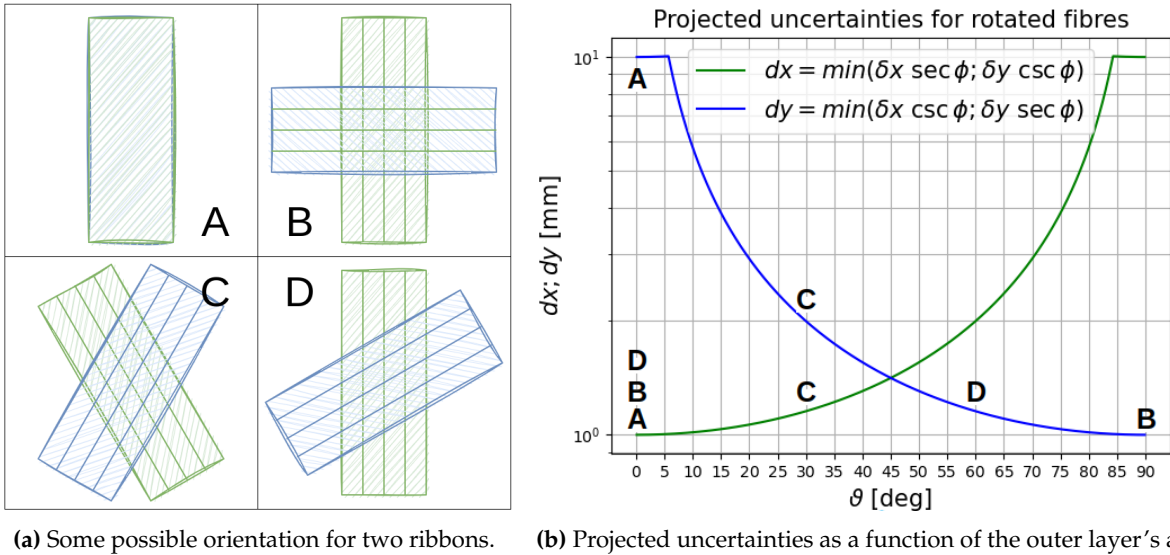


Fig. 4.2: Relation between the direction of the fibers and the associated uncertainties projected onto the axes. Some specific orientations of two overlapping ribbons are shown.

hits. If we consider a two-layer system the requirement of having only one crossing point (i.d. no ‘ghosts’) translates to having a difference in the number of turns $\lesssim 1$. In a cylindrical geometry the relation between the angle of the fibers and the number of turns completed, shown in Fig. 4.3, is determined by the dimensions of the cylinder itself. At this point, we can plot the resolutions as a function of the angle of one of the layers keeping the angle for the second layer such as $\Delta T = 0$. The results are in Fig. 4.4a while Fig. 4.4b shows the difference in angle for the two layers. We will consider two concentric cylinders, the outer layer being the one with a shallower angle: this is intended to reduce the effect of multiple scattering on the longitudinal position. Building the layers with infinite precision on the angle is clearly not feasible for this reason we can use the plots in Fig. 4.5, where the angles have been rounded to multiples of 5 deg. Additional attention we can have is to consider the length of the scintillating fibers: if the fibers are too long the light collection at the ends is decreased by the absorption. The length of the fibers in both layers is shown as a function of the outer angle in Fig. 4.5c. Clearly, this is the extreme case: depending on the intrinsic resolutions of the fibers, shallower angles and $\Delta T < 1$ could be chosen, simplifying the construction.

4.2.3 GEANT4 simulation

G4TessellatedSolid The first hurdle in the Geant4 simulation for this sub-detector is the definition of the geometry. The shape is the result of wrapping a squared fiber around a cylinder resulting in a ‘squared helix’. After some consideration there are two ways of defining this geometry:

- Taking bool difference of two G4TwistedBox¹. This is a simple solution but comes with some limitations: the shape of the fiber cannot be changed to circular; the twisted box cannot be twisted more than 90 deg, so a stack of clones is needed;

¹The documentation can be found here: G4TwistedBox

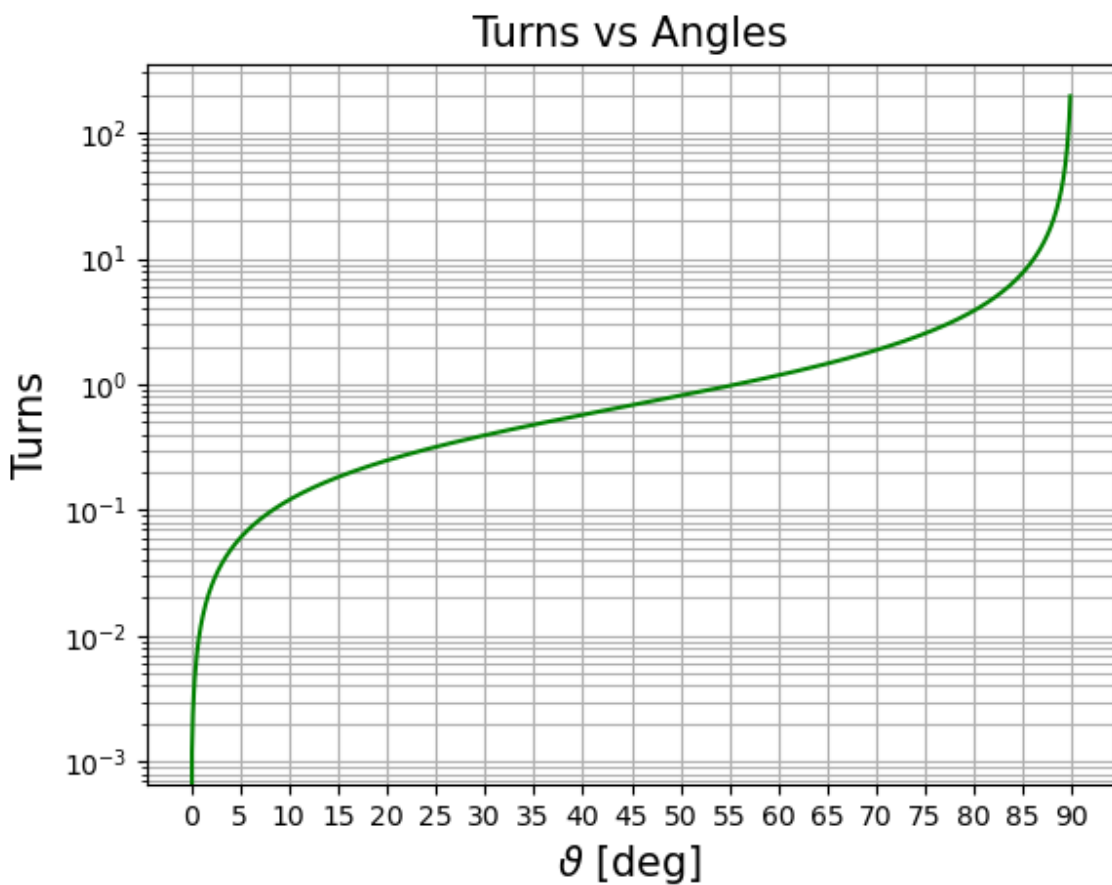
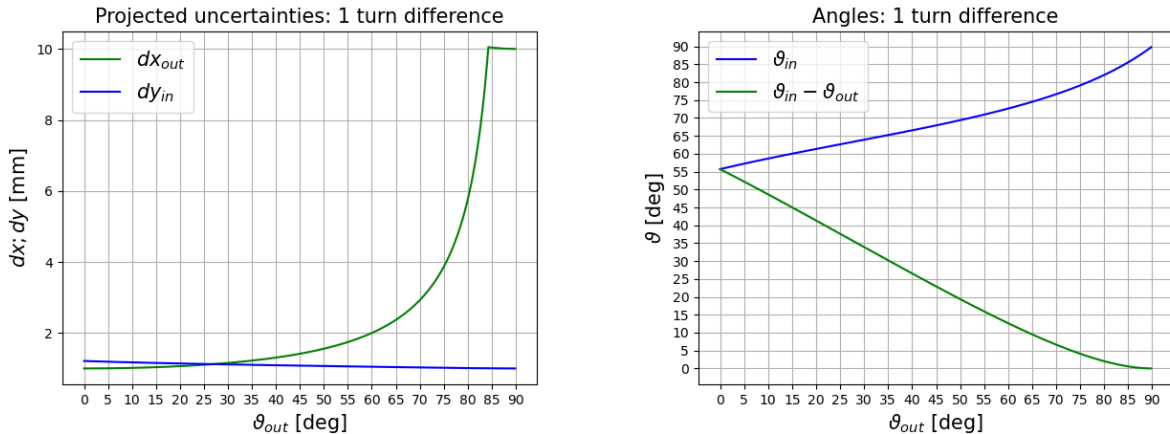


Fig. 4.3: In a planar configuration, the angle at which the fibers run translates directly to the angle at which the ribbon is oriented. In a cylindrical geometry, a fiber running at a given angle will complete a different number of turns depending on the dimensions of the cylinder.



(a) Projected uncertainties as a function of the outer layer's angle
(b) Angle of the inner layer and difference in angle as a function of the angle of the outer layer

Fig. 4.4: The results when considering two layers in a cylindrical geometry keeping the requirement $\Delta T = 0$: 4.4a shows the projected uncertainties; 4.4b shows the angle of the inner layer.

- Defying the geometry using G4TessellatedSolid², which means creating it by hand triangulating the shape. Clearly, this is a more cumbersome solution but it allows for more flexibility.

The core part of the code for generating the G4TessellatedSolid fibers is in appendix ??.

Fibers and read-out Aside from the specific geometry, the cardinal point is how to describe the fibers and their readout. The fiber itself is simulated as a three-layer volume:

- Core:
- First cladding: PMMA
- Second cladding: PMMA EMA

The optical property of the surface between the different layers is specified with a G4OpticalSurface³.

The readout simulates a SiPM:

- Optical grease:
- SiPM window: Silicon resin
- SiPM :

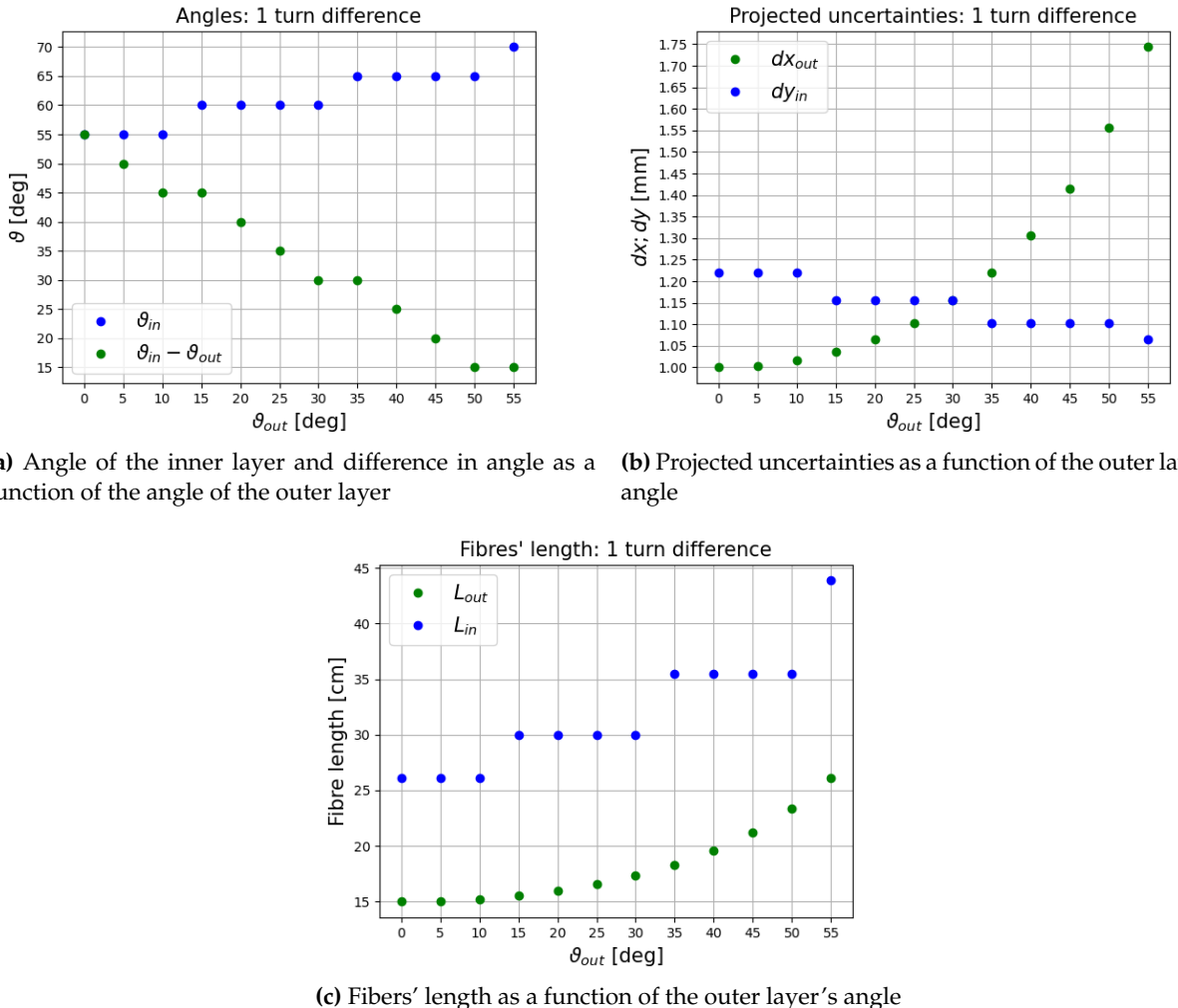
4.2.4 From γ s to waveforms

The simulation in GEANT4 ends with the recording of the optical photons entering the SiPM SensitiveDetectors. The physical processes going from the impinging photons to the analog signal are quite complex and simulating them would require a lot of effort (and CPU time). To get a feeling of the type of signals we can expect from the simulation we can create a simple script *faking* the readout. The required steps are:

- PDF: probability of a photon converting. This is a binomial distribution and is SiPM dependent: reasonable values $p_{PDF} \in [0.3, 0.5]$

²The documentation can be found here: G4TessellatedSolid

³The documentation can be found here: G4OpticalSurface



(a) Angle of the inner layer and difference in angle as a function of the outer layer's angle

(b) Projected uncertainties as a function of the outer layer's angle

(c) Fibers' length as a function of the outer layer's angle

Fig. 4.5: Key parameters as a function of the outer layer's angle keeping 1 turn difference between the two layers and rounding the angles to multiples of 5 deg.

- *Response*: per photon converted, add a 'waveform' at the photon time. The shape $w(t)$ is SiPM/electronics dependent but some assumptions can be made.
- *Dark noise*: add a probability of spurious photons converting. This is a poissonian process that gives n_{dark} photons distributed flat in the readout time.

$$W(t) = \sum_{i=0}^{n_\gamma} w(t_i) \cdot p_{PDF} + \sum_{i=0}^{n_{dark}} w(t_{flat}) \quad (4.2)$$

Once we obtain $W(t)$ we can apply a threshold w_{th} and turn the signal from analog to digital. If the w_{th} is crossed, we recorded a *hit*. Clearly, given the geometry under consideration, we need two *hits* to make a 'cylinder'-*hit* (a *c-hit*). Mapping pairs of hits in chits is not trivial and takes as parameters the dimensions of the cylinder and the SiPM numbers (or alternatively their position).

4.2.5 From *hits* to *c-hits*

4.3 Prototype/Beamtime

4.4 Conclusions

Part II

muCool

Chapter 5

muCool

5.1 The working principle

5.2 Simulations

5.2.1 Cooling

5.2.2 Extraction

5.2.3 Re-acceleration

5.3 Validation

5.4 Conclusion

[1] [2] [3] [4] [5] [6] [7]

Chapter 6

muCool upgrade

6.1 New target

6.2 Cryogenic system

6.3 High Voltage system

6.4 Conclusion

[1] [2] [3] [4] [5] [6] [7]

Part III

MEG II

Chapter 7

MEG II and the Cockcroft–Walton

This Chapter is dedicated to an in-depth description of the MEG search and the MEG II apparatus. After the description of the different subdetectors and their functionality a description of the beamlines will follow. MEG II is served by the main muon beamline, part of the PSI beamlines described in the Introduction Chapter, and a secondary proton beamline equipped with its own Cockcroft–Walton. This machine has different uses in the collaboration, which will be here discussed, and its functioning has been one of my main tasks. For this reason, some additional details will be here included.

7.1 MEG II

7.2 XEC

7.2.1 Xe scintillation

7.2.2 Xe as calorimeter

7.2.3 Cryogenics

7.2.4 PMTs

7.2.5 Performances

7.2.6 LED Calibration

7.3 Spectrometer

7.3.1 COBRA

7.3.2 CDCH

7.3.3 TC

7.4 Trigger and DAQ

7.5 Beam and target

The beam lines at PSI were described in 1.5. In particular, the beam line delivering μ^+ to MEG II is the $\pi E5$ line. This line is shown in Fig. 7.1 and the key elements are here discussed

7.5.1 $\pi e5$

This beam-line has actually two possible configurations: this will allow to share it between MEG II and Mu3e. As already illustrated, the surface muons delivered by this beam-line are produced for the decay of the pions generated as secondary beams from the HIPA proton beam. On top of muons, pions and positrons also are transported by the beamline: the rate of the different species is momentum dependent and is shown in Fig. ???. The peak at 29 MeV/c is the working point of the experiment.

$$\Delta R = a \left\{ \left[\left(\frac{200m_e}{M} \right)^{1/2} f \frac{E}{Mc^2} \right]^2 + \left(3.5 \frac{\Delta p}{p} \right)^2 \right\}^{1/2} p^{3.5} \quad (7.1)$$

The elements that makeup one of the two configurations, the "L" channel, were designed *ad hoc* for MEG II.

Quadrupoles and separator

BTS

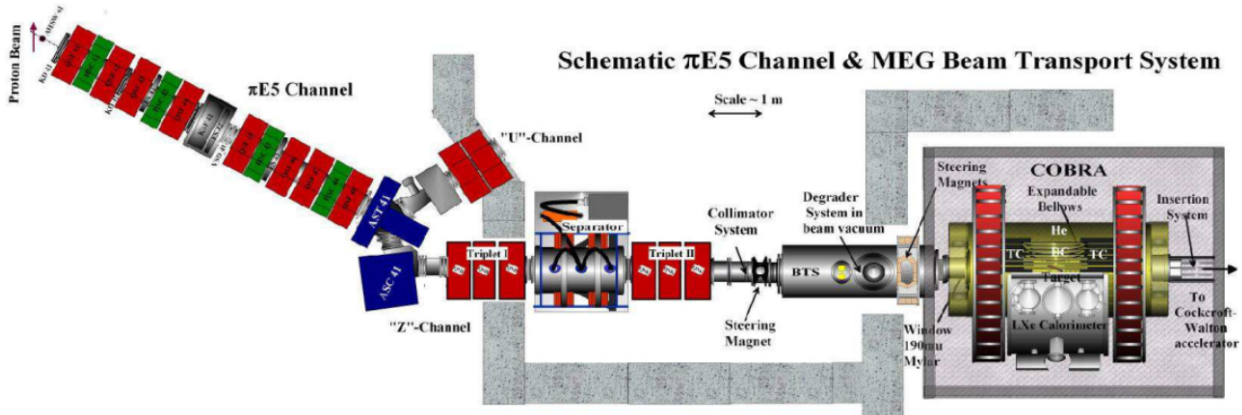


Fig. 7.1: Detail of the $\pi E5$ beamline at PSI. OLD

COBRA Finally the beam enters COBRA. The design choice for this element was previously illustrated (7.3.1). The behavior of the beam inside this element is quite tricky to simulate consistently.

7.5.2 Simulations

G4BEAMLINE

MAD-X During 2022/2023 Luca Biasia, a Master student in Pisa, developed a MAD-X¹ simulation to describe the $\pi E5$ line and cross-validate the results obtained using G4BEAMLINE. My contribution to this simulation was only partial: I provided Luca with some working MAD-X examples, developed while attending the JUAS, for him to start playing with this simulation framework. After this initial ‘starting kit’, Giovanni Dal Maso was the one overseeing the development while I only followed the updates and gave feedback or suggestions.

After a comparison with data and G4BEAMLINE some discrepancies arose and, after many iterations, they were associated with the description of the fringing fields of the components in MAD-X. The solution adopted was to slice the field maps in thin layers and define many thin ‘MAD-X elements’. A comparison of the results from QSK41 to COBRA center is shown in Fig. 7.2. During the beam tuning in June 2023, this simulation was crosschecked: after measuring the beam spot at COBRA center the currents of the magnets were chosen with MAD-X to obtain a different beam shape. The measurement was consistent with the resulting simulation. This was a great achievement and, moving forward, this tool is going to play a key role during the beam tuning.

7.5.3 MEG II target

Deformation and pictures

¹MAD-X is a general-purpose tool for charged-particle optics design and can be found [here](#).

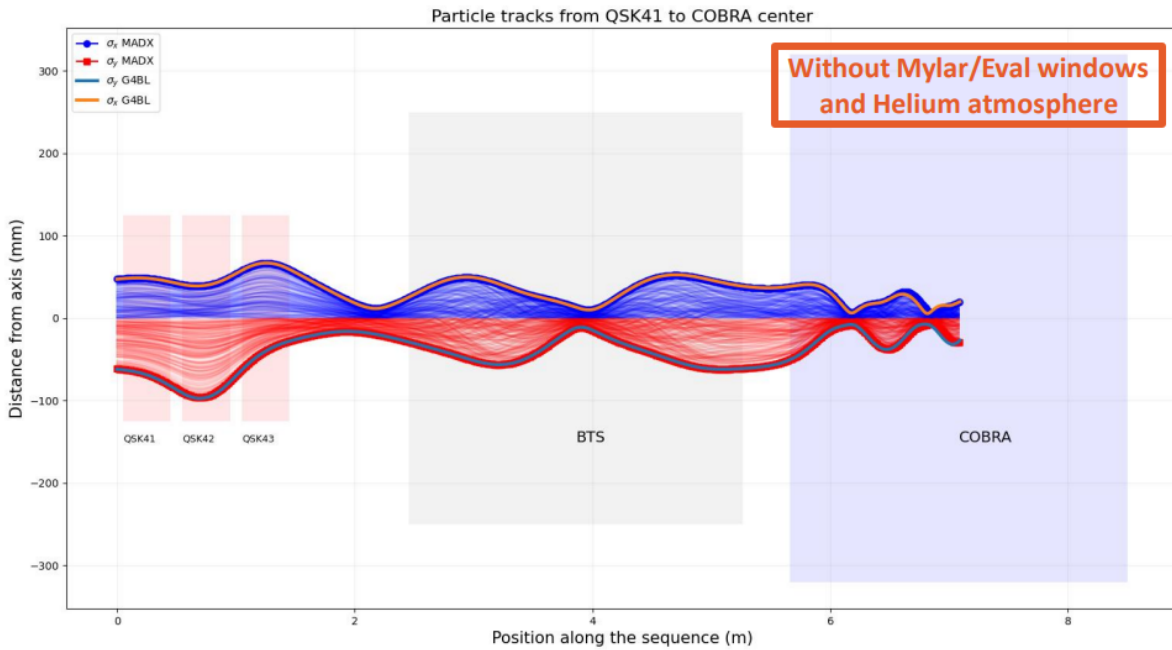


Fig. 7.2: Comparison of the results from the G4BEAMLINE and MAD-X simulations for $\pi E5$. While the agreement is very good for most of the beamline, there is some difference inside cobra. This is due to the difficulty in describing the highly ‘non standard’ magnet. Given MAD-X has no particle interaction, the comparison is fair only when removing all materials from the beamline in the G4BEAMLINE simulation.

7.6 Cockcroft–Walton

In addition to the muon beamline, MEG II has a Cockcroft–Walton proton accelerator. After the description of the machine, we will see the use of this accelerator by the collaboration: calibrations of the Liquid Xe Calorimeter and exotic searches.

7.6.1 Description of the machine

The accelerator is a single-stage in-line singletron produced by HVEE. This machine is a compact Cockcroft–Walton with a terminal voltage of 0.1 \div 1.0 MV and a proton current up to 100 mA.

Source The RF ion source is a bottle of gas that is excited by an RF oscillator. The electrons in the gas are excited and, because of the collisions with the neutral gas particles, cause ionization. The plasma produced is confined with an axial magnetic field and serves as the source of positive ions, which are extracted by applying a DC electric field. A schematic of the working principle of the RF ion source is shown in Fig. 7.3

CW-Circuit The high-voltage multiplier and rectifier stack, together with the RF driver and HV control and stabilizing system, is one of the core sections of the machine. It is located in the main pressure tank, while the RF resonance coils are in a separate SF₆ filled tank and the RF driver in a separate cabinet. This gas is often used as a gaseous dielectric medium because of its high dielectric strength, the result of the gas’s high electronegativity ² and density. In the case of an

²Electronegativity is a measure of the attraction of an atom for bonding electrons in molecules compared to that of other atoms: large values indicate a stronger attraction and it increases from left to right across the periodic table.

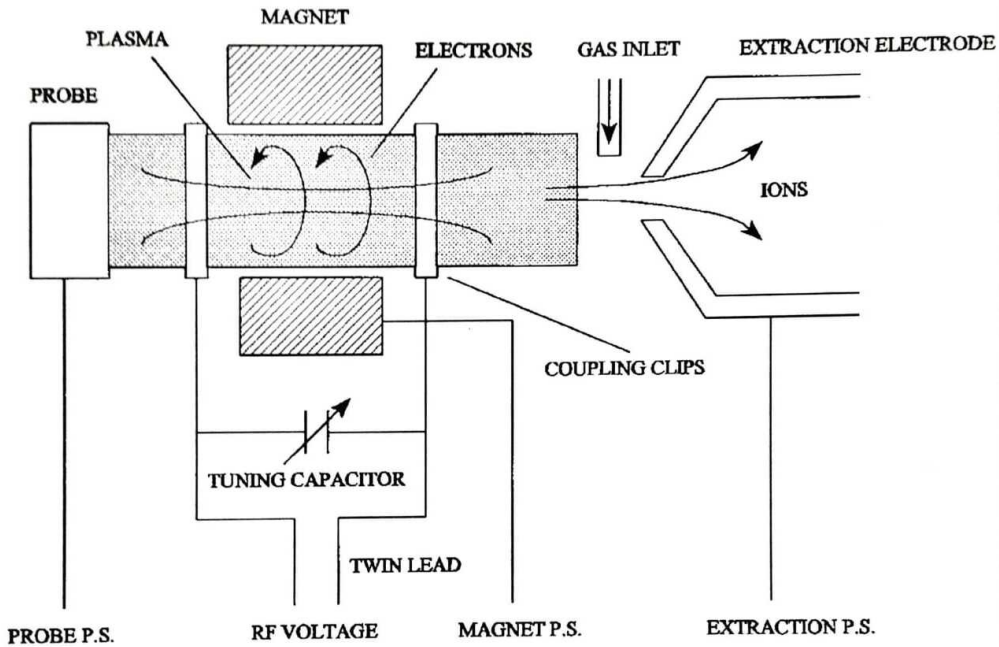


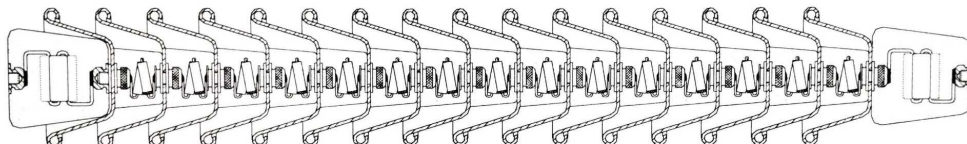
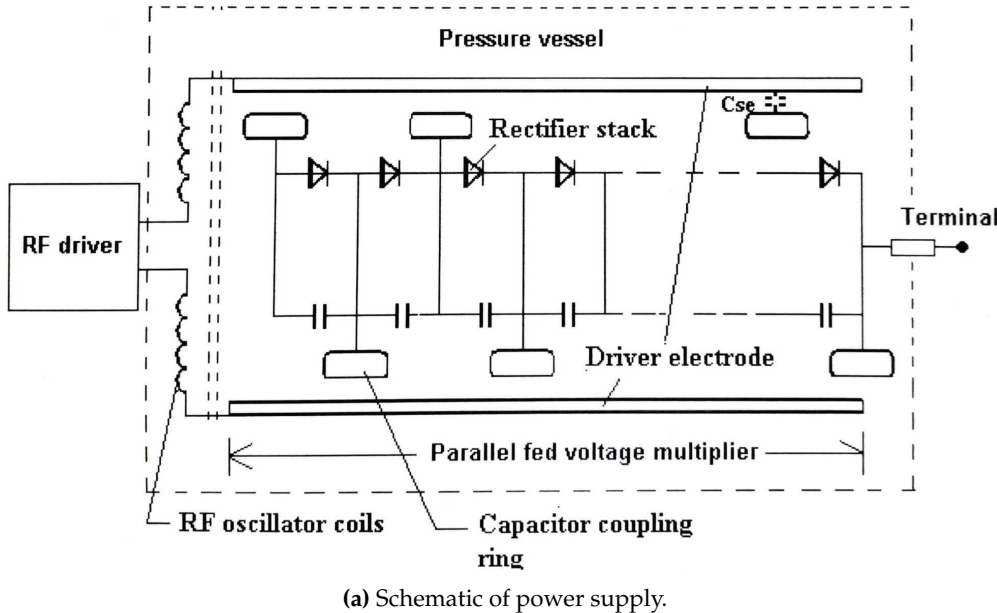
Fig. 7.3: Sketch of the ion source of the CW.

arc, SF_6 can break down in different ways but most of the decomposition products tend to quickly re-form SF_6 , a process termed *self-healing*. Arcing or corona can also produce disulfur decafluoride (S_2F_{10}), a highly toxic gas, which is the reason extra care is needed when opening such a system. This stack is a parallel-fed CW power supply that consists of a series of high voltage rectifiers and capacitive coupling *corona* rings. The power is fed via an RF driver capacitive coupled. A sketch of the inner structure of a rectifier assembly (*ass'y*) is shown in Fig. 7.4b while in Fig. 7.11b is clearly visible the way the ass'ys are mounted.

Driver The driver, as the name suggests, is the circuit that feeds the voltage/power to the whole system. In between the driver and the CW stack of rectifiers' ass'ys a resonant circuit is used to amplify the output of the driver. The power is fed to this resonant circuit in phase with the oscillating current. Keeping the frequency at resonance, the driver controls the terminal voltage adjusting the pulse width. A block diagram of the driver is shown in Fig. 7.5

Start-frequency The system can operate only at resonance and this frequency f_{res} is defined by the coil and dynodes. During star-up, the system starts at f_{start} higher than the resonance and then lowers it until the resonance is found. A parasitic frequency f_{par} , with $f_{par} > f_{res}$, is also present. At this frequency, the driver oscillates at a higher frequency, and no power is transferred to the terminal. To avoid the higher frequency, a tuning is needed so that $f_{par} > f_{start} > f_{res}$.

Q-factor In the RF resonance circuit high amounts of 'blind power' can be present (up to 1 MW). The quality factor (Q-factor) of the RF resonance circuit is the ratio of blind to dissipated power. E.g. for a blind power of 1 MW and a Q-factor of 1000 the transformer coil dissipates 1 kW of heat. If this factor is not high enough the dissipated power is too high and will prevent the driver from operating correctly. The Q-factor is measured using a function generator and looking at the



(b) Sketch of the inner structure of a *stack ass'y*: 15 rectifiers and 2 resistors.

Fig. 7.4: The first schematic (a) shows the CW circuit and the capacitive coupling to the RF driver while the second (b) shows the internal structure of a rectifier stack (*stack ass'y*).

relative phase and amplitude of voltage in two points of the accelerator's RF resonance circuit. A sketch of the measurement is shown in Fig. 7.6a. The system is at resonance when there is no relative phase between V_1 and V_2 , and the value of V_1/V_2 is used to evaluate the Q-factor:

$$Q = Z_{coil}/R_{loss} = 2\pi f_{req} I_{coil} (V_1/V_2 - 1)/R_l \approx 43.9 \times f_{res} [\text{kHz}] \times (V_1/V_2 - 1) \quad (7.2)$$

7.6.2 XEC calibrations

On top of the LED calibration illustrated in 7.2.6

'Standard' lithium calibration

Charge EXchange reaction

7.6.3 X17

The protons coming from the CW have been mainly used for the calibration of the XEC detector, but also to perform a parasitic measurement: the search for the X17 anomaly. This search, done in 2021-2023, will be extensively discussed in Ch. 9 but we wanted to underline here the key role that the CW machine has played in this parasitic search for exotic physics.

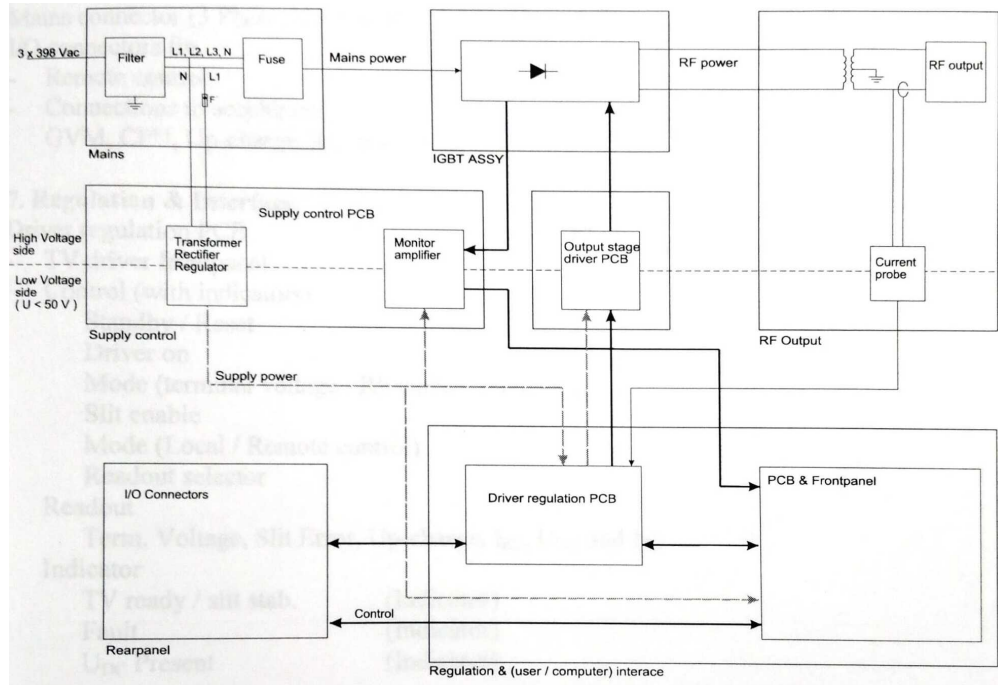


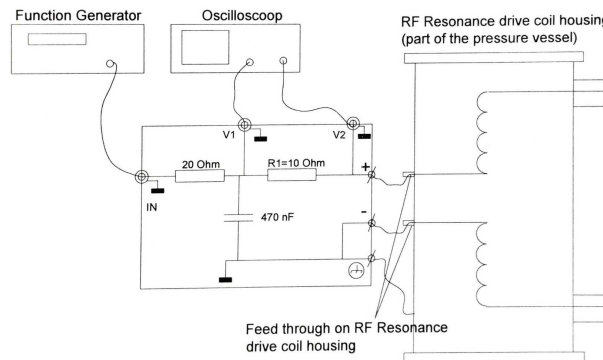
Fig. 7.5: Block diagram of the driver

7.7 CW issues and maintenance

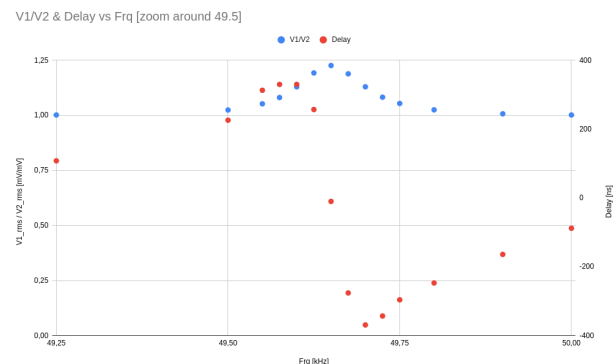
By the end of 2020, the CW started having some minor problems: the machine was running fine but the time required to switch it on kept growing longer. While the whole procedure would normally take $\sim 15 \text{ min}$ the time required exceeded the hour. We also noticed the machine was getting unstable when running near the maximum voltage at 1 MV. Following this behavior, an intense exchange with the HVEE company started and we performed many different tests on both the software and hardware sides.

Hot Fix We performed a measurement of the Q-factor of the machine using Eq. 7.2, shown in Fig. 7.6b. The value found was a factor $\sim 2k$ lower than expected and the position of the resonance frequency was shifted from the design value. For more information on the functioning of the machine and the Q-factor see Sec. 7.6.1. We adjusted the frequency at which the machine starts when turning ON. This solved the delay problem but didn't recover the maximum voltage. The machine was now starting quickly but working in a stable configuration only up to half of the nominal maximum voltage. As explained in the previous paragraph this was not a problem for the ‘usual’ calibrations but was a worrying sign on the health of the machine and would have prevented the CEX. At this point, an expert from HVEE was sent to inspect the machine.

Proper Fix After running some checks opening the CW was deemed necessary and for this reason, we removed the SF₆ contained in the main tank. After the extraction of the CW, we inspected and measured all the elements, removing also some of the *corona rings* for easier inspection. We



(a) Sketch of the circuit to measure the Q-factor.



(b) Example of measurement of the Q-factor: in red the delay while in blue the fraction V_1/V_2 .

Fig. 7.6: The Q-factor is the ratio of blind to dissipated power. Via this number is possible to evaluate the energy dissipated as heat running the machine. If it is too low the machine cannot operate correctly.

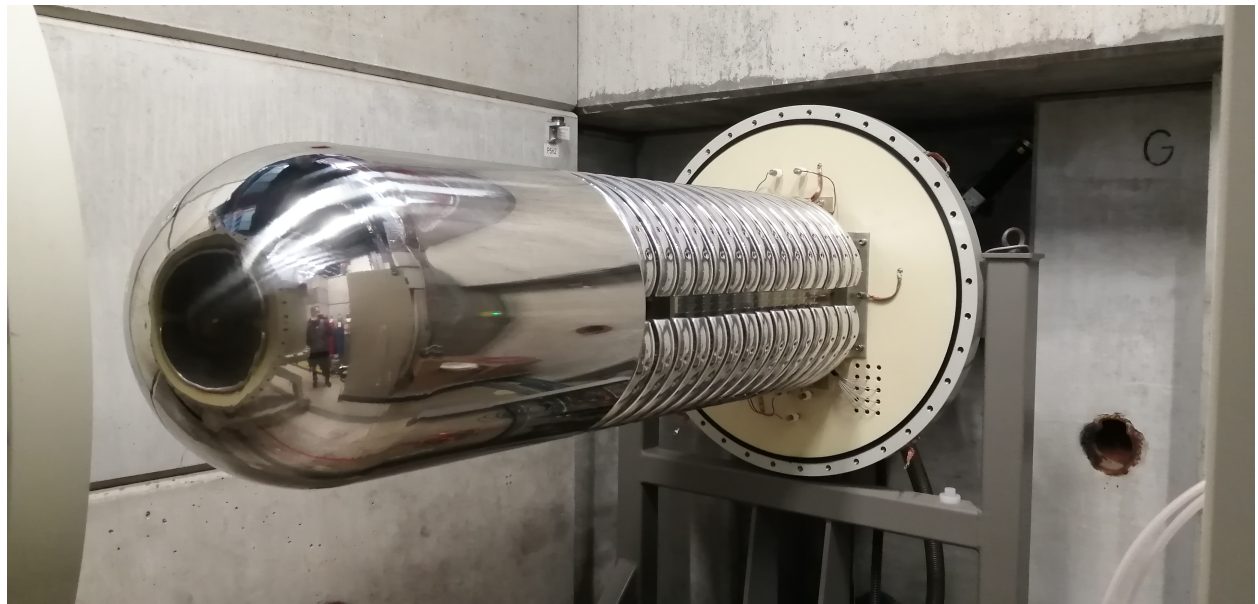


Fig. 7.7: View of the CW after the extraction from the external volume. This volume contains SF₆ which is used as a gaseous dielectric medium and needs to be evacuated before the extraction.

found signs of arcing on one of the *rectifier ass'y*. After the substitution of this element³, the machine was closed again, filled with SF₆, and tested again. This whole process is shown in the pictures in Fig. 7.11. Unfortunately, the faulty behavior persisted and we noticed sparks in the main volume. After re-opening we found burning marks on the rectifier ass'y next to the exchanged one. We then realized that both were damaged but the first was functioning as a 'bridge', preventing the second from being completely destroyed. After the substitution of the second and the tuning of the machine, we finally recovered its full functionality: quick switching ON and stable operation in the full range of voltages. 7.12.

³The rectifier ass'y are stacks of alternated diodes and aluminum capacitors capped by two resistors. We could re-use the capacitors, after careful cleaning, while resistors and diodes were too badly damaged. The process of refurbishing is shown in Fig. 7.12

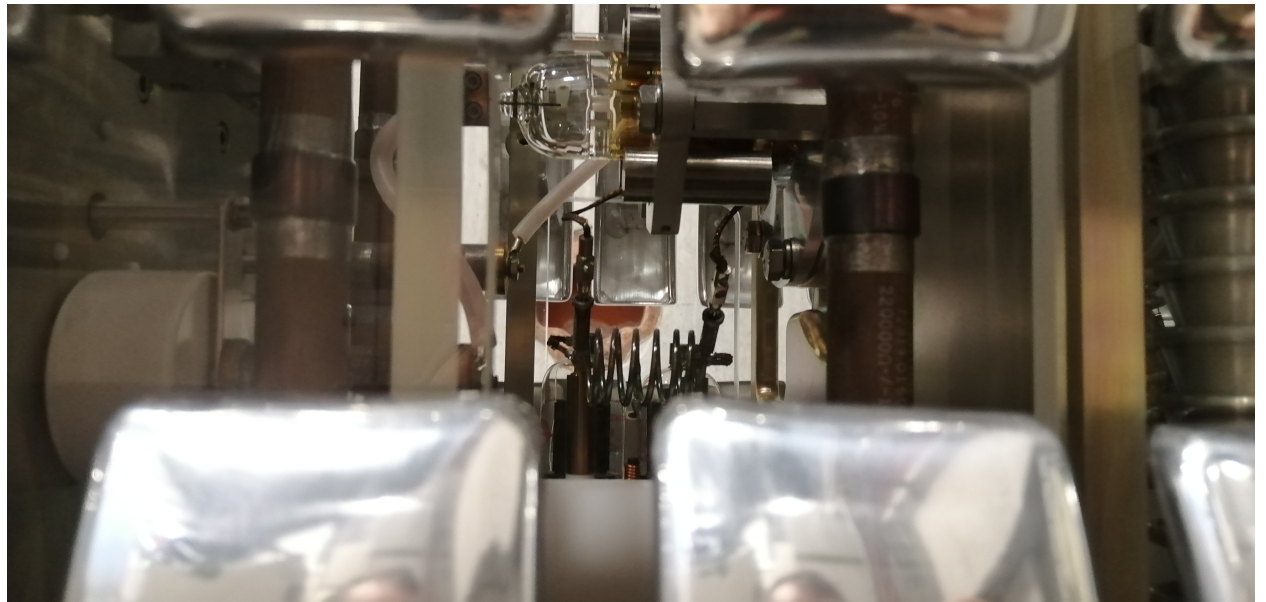


Fig. 7.8: View of the source of the CW machine.



Fig. 7.9: Top view of the CW after the removal of a few AAA. Here we can see all the elements of a CW circuit: red - the resistors on top; metallic rings on the central tube - the capacitors; blue and metallic cups - the resistance and capacitors of the rectifiers, which run vertically.

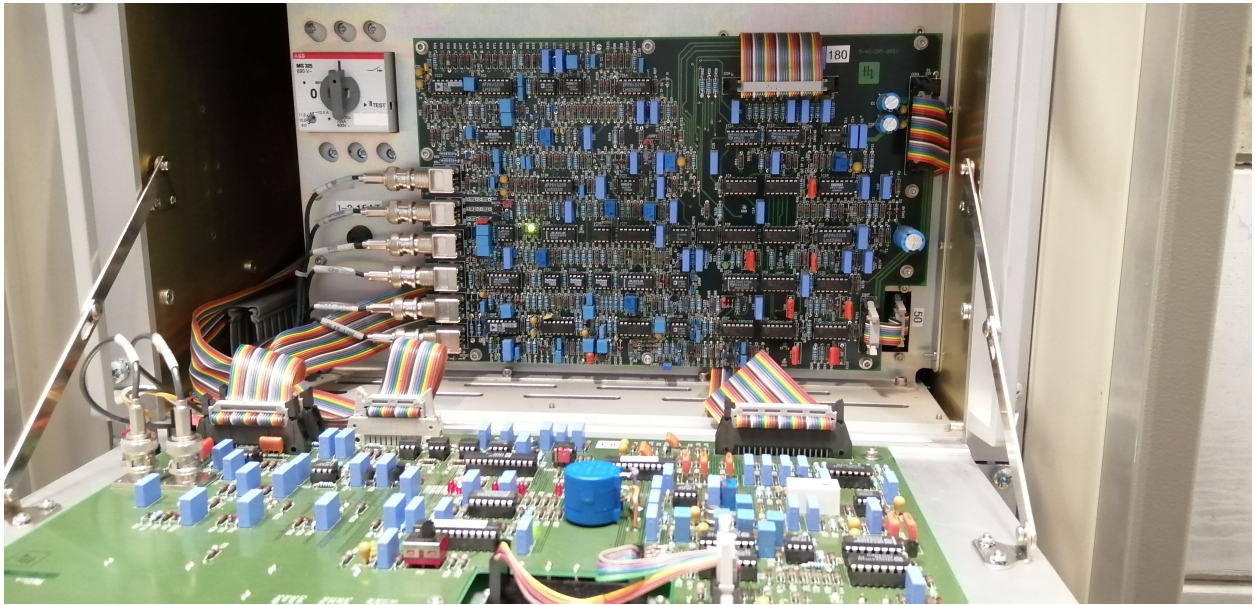


Fig. 7.10: Picture of the control panel for the CW machine.

7.8 Conclusions

In this (very dense) chapter we went through the description of two key elements of the work I have done during these three years: the MEG II apparatus and the Cockcroft–Walton. While I took no part in the design of either, in these years I spent a lot of time ‘hands-on’ on many subsystems of the MEG II apparatus: calibrations, tuning, and fixes of various types. On the other side, the CW functioning has been one of my main tasks. The unfortunate hiccup with the CW gave me the additional unforeseen opportunity to assist the HVEE technician in testing and fixing the machine, which was an extremely interesting experience.



(a) Discovery of the burning marks on two rectifiers. The reflectivity was a challenge in taking the picture.



(b) Extraction of the broken rectifiers.



(c) Broken rectifier ass'y after the extraction: clearly visible is the burned blue resistor at the top.

Fig. 7.11: After close inspection we found burning marks on two rectifiers' ass'y (7.11a). These were removed (7.11b) and carefully inspected (7.11c). The only salvageable part of the rectifiers were the aluminum capacitors, which we cleaned from burning residuals, while all diodes and resistors had to be exchanged.



(a) Picture of the burning marks on the end resistors of the rectifier ass'y.



(b) Assembly of one of the new stack: black - resistors; brown - diodes; metallic - aluminum capacitors.



(c) One of the finished new rectifiers.

Fig. 7.12: The rectifiers are made of three elements: diodes; aluminum capacitors; resistors (7.12a). Only the capacitors were salvageable: we re-assembled the rectifiers with new diodes and resistors (7.12b; 7.12c).

Chapter 8

Liquid Hydrogen target

In this chapter the Charge EXchange reaction, a calibration for the liquid XEnon Calorimeter, will be discussed and an in-depth description of the associated Liquid Hydrogen Target is given. Data taking, analysis, performances, and the different modifications will be also discussed. This target was designed in 2020 to overcome some limitations of the previous and in the last two years went through some heavy re-development. This calibration is cardinal for the correct functioning of the key subdetector of the MEG II experiment. It was one of the main tasks in my involvement in this experiment and it absorbed a sizable portion of my time and effort.

8.1 Charge EXchange reaction

As already discussed, the $\mu \rightarrow e\gamma$ process searched by MEG leads to a monochromatic photon at 53.2 MeV. We saw in Sec. 7.6 the XEC calibration which is performed three times a week. Unfortunately, while the frequent calibrations are great for the time dependencies, the photon produced by the Li is at lower energy than the signal. To calibrate the calorimeter near the signal region, the Charge EXchange reaction is exploited. The Charge EXchange (CEX) process $\pi^- p \rightarrow \pi^0 n$; $\pi^0 \rightarrow \gamma\gamma$ produces γ with a flat distribution in the interval [54.9, 82.9] MeV. Extremal values are reached for photons emitted back to back. Thus, a signal-like photon can be tagged by detecting a high-energy photon in the opposite direction. The tagging is performed with a BGO detector which can be positioned (steps of 30 cm in \hat{z} and 16 deg in $\hat{\phi}$) opposite to specific patches of the XEC. The requirement $\Delta E/E < 1\%$ translates to $\Delta\theta_{\gamma\gamma} < 5^\circ$. A sketch of the CEX measurements, a picture of the BGO detector, and its moving structure is shown in Fig. 8.1.

8.2 BGO

The BGO crystal already mentioned, and shown in Fig. 8.1b, is an auxiliary detector that plays a key role in two subjects of this thesis. For this reason, we will here describe it in some detail. BGO refers to $\text{Bi}_4\text{Ge}_3\text{O}_{12}$, a compound with a cubic crystal structure and often used as a scintillator. This detector is, in particular, a matrix 4x4 of $4\text{ cm} \times 4\text{ cm}$ crystals and mounted on a structure (see Fig. 8.1c) that allows it to translate and rotate around COBRA.

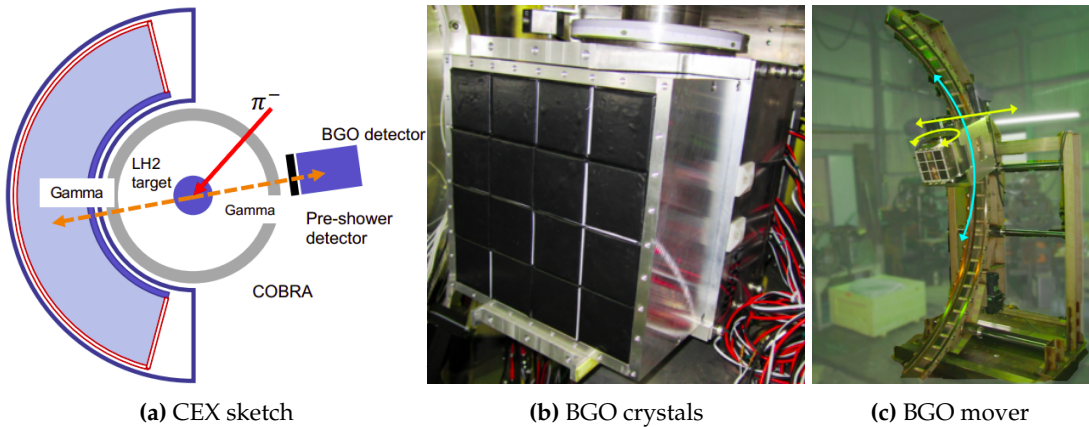


Fig. 8.1: Diagram of the CEX measurement, with the back-to-back photons configuration to define the XEC patch via the BGO positioning (8.1a) Picture of the BGO detector (8.1b) Picture of the BGO mover (8.1c).

8.3 LH2 target working principle

The details of the circuit and the operation changed on a yearly basis but it's worth do discuss the overall working principle before seeing the evolution of this system. Liquid Hydrogen was chosen to provide the protons needed for the CEX reaction. The incoming 70.6 MeV/c π^- are stopped in a cylindrical cell (60 mm diameter, 70 mm length) of 0.5 mm stainless steel containing liquid Hydrogen. This corresponds to $\sim 90\%$ stopping efficiency. The hydrogen has to be kept liquid ($T < 20.39$ K at 1 atm) and in the center of the COBRA magnet, requiring a cryogenic infrastructure to be inserted for 2 m. The target consists of four sub-systems:

- A “closed volume” hydrogen circuit, in which a 1.5 bar over-pressurized 100 ℓ buffer is connected to the target cell
- A copper rod (2 m in length and 2 cm in diameter): supported and cooled at one end with liquid helium flowing in a copper coil; holding the target cell at the other.
- Vacuum Insulation for the whole system
- A slow-control based on an SCS2000 [**midas**] controlling: temperatures, pressures, He flux, and the alarm system

The buffer volume for the gaseous hydrogen, as well as all the infrastructure and services, are kept outside the magnet. The circuit for the 2021 version is shown in Fig. 8.2 and, to increase the readability, the different sub-circuits are color-coded:

- Blue - Hydrogen is filled into the buffer from a cylinder, which gets then removed. The buffer itself is connected to the cell, the exhausting line, a vacuum pump, piezoresistive pressure transmitters and a Nitrogen bottle
- Red - The liquid He flux is obtained by pressurizing a Dewar with an He bottle. The He passes around the Cu rod and through a heater before entering the He recovery line
- Green - Insulation vacuum system
- Yellow - A nitrogen bottle is used for purging the hydrogen when emptying the buffer and kept connected for safety

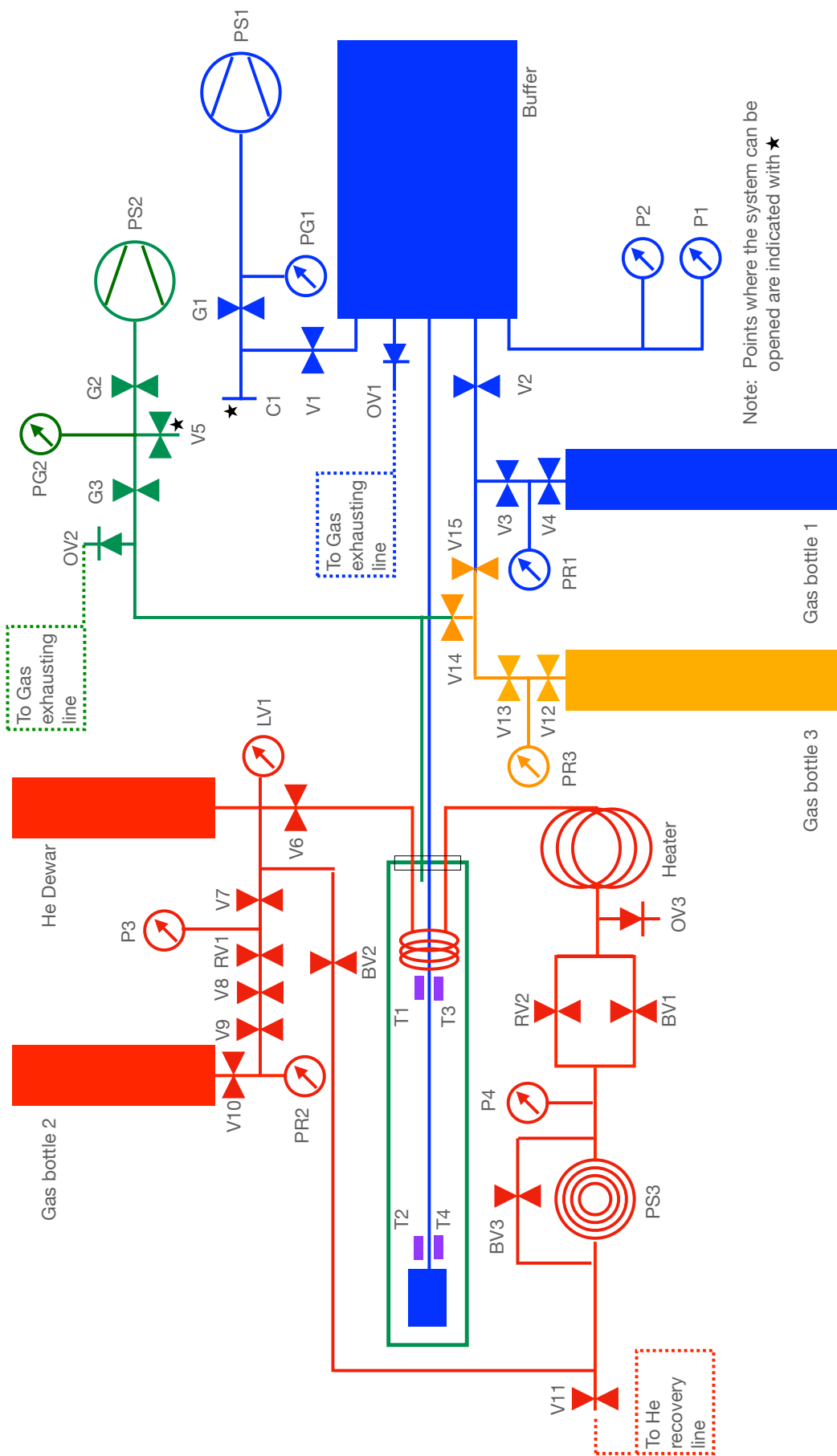


Fig. 8.2: Circuit of the LH2 target. To increase the readability of the scheme of the circuit, the different sub-circuits are color-coded:
Blue - Hydrogen; Red - Liquid Helium; Green - Insulation vacuum; Yellow - A nitrogen

8.3.1 Operation and control

The operation of the target itself is partially manual and partially controlled through a LabVIEW program which, for example, controls the read-out of the various sensors and the flux of the incoming He. A module SCS2000 allows to read the various sensors. There are two key indicators used to monitor the liquefaction process and stability of the system:

- Temperature sensors: resistors(later replaced by Lakeshore silicon diodes sensors) have been put in thermal contact with the Cu rod at both ends (two per side for redundancy). The readings of these elements allow us to monitor the cooling at the Cu coil and the cell.
- Hydrogen pressure: at room temperature, the hydrogen is set to 1.5 bar over-pressure. When the liquefaction starts the overall pressure is reduced and can be linked to the amount of liquid Hydrogen in the cell.

8.4 2021

I started my Ph.D in November 2020 but I joined the activities after the first year, in October 2021. For this reason, I did not participate in the development of the first iteration of the target and I joined directly the first tests before the data taking period. The status of the LH2 Target and the preliminary results of the 2021 CEX were presented at the 15th Pisa Meeting on Advanced Detectors [1].

8.4.1 Data taking

The data taking lasted roughly two weeks, during which CR runs and XEC calibrations were run while the target was cooling and liquefying. As soon as the level was sufficient the pion beam would be used for CEX data taking for a specific patch of the XEC. When the dewar needed to be exchanged, the data taking would be stopped and CR/calibrations would restart, waiting for the target to be sufficiently full to restart. In figure 8.3 is shown the history of the Hydrogen and Helium pressure at the dewar. Interesting features are:

- The decreasing parts of the blue plot are the liquefaction period: the Hydrogen pressure drops because of the phase change
- During liquefaction, some spikes can be seen: these are instances in which the system became unstable and liquefaction stopped
- The speed of cooling and liquefaction is always the same because the result of hardware choices;

Overall, CEX data could be collected when the target was considered ‘full enough’: below AAA bar, meaning 0 %. In the two weeks, this translates to efficiency of $\epsilon_{2021} \approx 0$. The efficiency for 2021 was lower than expected and the necessary statistic was not reached for every patch.



Fig. 8.3: Measured hydrogen pressure in the target and helium pressure in the dewar used for cooling during 2021 CEX data taking. Beam was ON when the target was considered ‘full enough’: below AAA bar, meaning 0 %. This translates to a time efficiency of $\varepsilon_{2021} \approx 0$. Unfortunately, the low efficiency prevented the collection of the necessary statistics for every patch of the XEC.

8.4.2 Data analysis

8.5 2022

8.5.1 Upgrades

He circuit

Cup

Shielding

8.5.2 Data taking

8.5.3 Data analysis

8.6 2023

Although the 2022 CEX campaign was much more successful than the previous one, the limitations of this design and the second iteration dictated a hectic schedule during data taking. The (somewhat risky) modification of the liquid hydrogen cup turned out to be a good improvement but there was still room for refinement. For this reason, we went back to the drawing board.

8.6.1 Upgrades

He circuit

Cup

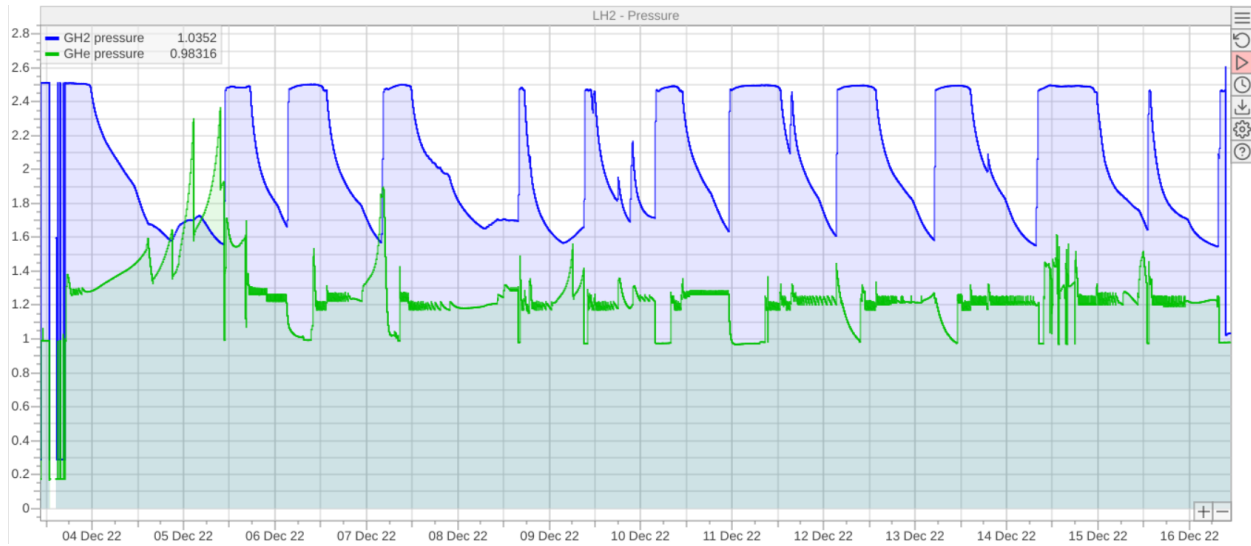


Fig. 8.4: Measured hydrogen pressure in the target and helium pressure in the dewar used for cooling during 2022 CEX data taking. Beam was ON when the target was considered ‘full enough’: below AAA bar, meaning 0 %. This translates to a time efficiency of $\varepsilon_{2022} \approx 0$ (against $\varepsilon_{2021} \approx 0$). The improvement in efficiency allowed us to collect the necessary statistics for every patch of the XEC.

Shielding

8.6.2 Data taking

8.6.3 Data analysis

8.7 Conclusions

Bibliography on LH₂

- [1] B. Vitali et al. "A liquid hydrogen target to fully characterize the new MEG II liquid xenon calorimeter". In: *Nucl. Instrum. Meth. A* 1049 (2023), p. 168020. DOI: 10.1016/j.nima.2023.168020.

Chapter 9

Search for X17

After the recent publications from the ATOMKI collaboration, the so-called X17 anomaly piqued the interest of the community. The flexibility of the MEG II apparatus allows for a variety of exotic searches and the collaboration deemed of interest searching for this anomaly in an uncorrelated way. The chapter starts with a recap of the previous searches and then moves to the description of this search in MEG II: setup used, simulations developed, data acquisition and data analysis.

9.1 ATOMKI and the X17 ‘anomaly’

The story of the Hungarian group and their result

9.2 X17 in MEG II

After reading with great interest the papers from ATOMKI, the MEG collaboration started evaluating if repeating this measurement was achievable with the MEG II apparatus. In 2022 the first data collection was performed but the time constraints, required to keep the main focus of the experiment on the $\mu \rightarrow \gamma e$ process, meant not all the necessary preparatory studies could be performed. The details of this first data-taking will be skipped and we will move directly to the second campaign, performed in 2023.

9.2.1 MC simulations

9.2.2 Magnetic field choice

The first step is to identify the magnetic field required. The geometry of the MEG II detector, in junction with the magnetic field, defines the acceptance of the produced particles. Given the nature of the COBRA magnet, the parameter here is the scaling of the magnetic field. Thorough simulations were run to optimize the scaling factor, finding the best compromise between the efficiency for signal and background reconstruction to be $B_{X17} = 0.15 \times B_{MEG}$. This value can be roughly estimated considering that a scale factor of 1 is optimized for positrons of 53 MeV while the pair produced by the X17 decay should be roughly at 8 MeV ($8/53 \approx 0.15$).

9.2.3 Target

The setup for the target is quite straightforward: a carbon fiber vacuum chamber is mounted at the tip of the insertion system of the CW bellows system; a mounting system holds different types of targets. The bellows system is the one used for XEC weekly calibrations and will be not discussed.

Vacuum and mechanical structure The thickness and dimensions of the carbon fiber vacuum chamber have been optimized via dedicated simulations for both integral structure and particle interaction. After receiving the carbon fiber the chamber was glued and tested for vacuum.

Lithium target The interesting process requires Lithium atoms but Lithium targets tend to be unstable. Among the options studied LiF and $\text{Li}_{3.6}\text{PO}_{3.4}\text{N}_{0.6}$ were the most promising. Looking back we now know that the spattering process behind the production of our targets resulted in a poorly characterized end-product. LiF targets were produced by INFN Legnaro while $\text{Li}_{3.6}\text{PO}_{3.4}\text{N}_{0.6}$ targets were produced at PSI.

9.3 Data acquisition

9.3.1 Beam tuning

The beam tuning was performed by substituting the end cap of the proton beam line with a transparent cap with a AAA crystal. The proton beam produces visible photons hitting the crystal so the beam position can be observed. Normally this operation would be done while the upstream side of COBRA is not closed, allowing the installation of a webcam that gives instant feedback on the beam position. This was not the case so we were forced to use the camera installed inside COBRA for MEG II target monitoring. This camera has some settings for *gain* and *aperture* but is controlled using a script in *ssh* and to view the picture first is necessary to move them locally, making the whole procedure somewhat cumbersome. Key aspects of the beam to be tuned were:

- Energy: This parameter is controlled by the *Terminal Voltage* of the CW.
- Focus: This parameter is controlled by the *Extraction Voltage* of the CW. Fig. 9.2 shows how the beam spot changes as a function of this parameter.
- Position: This parameter is controlled by the three dipoles of the CW beamline. The change of the position for different values of the dipoles at 500 keV is shown in Fig. 9.1.

After a careful scan of the three parameters, working points at different energies were chosen: the most relevant are the ones for 500 keV and 1080 keV. It is of interest to notice that 1080 keV is the balance between what was previously discussed and the limitations of the CW machine: a higher (~ 1100 keV) energy would be a better choice but the nominal upper limit of the machine is actually 1 MeV, meaning having it running stably at 1080 keV is already an achievement. To the best of our knowledge, the beam at COBRA center during the data-taking was Gaussian $(x, y) = 2, -2 \text{ mm}; (\sigma_x, \sigma_y) = 2, 2 \text{ mm}$.

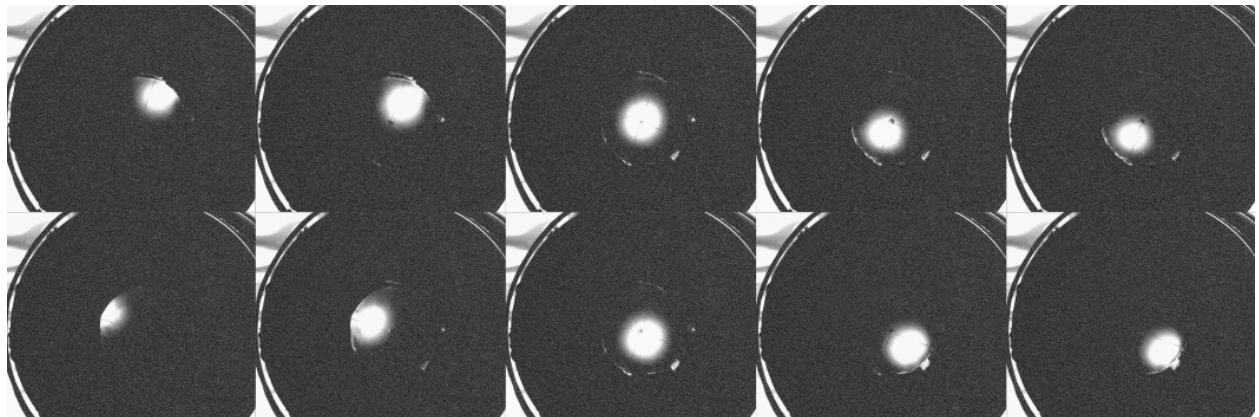


Fig. 9.1: Position of the proton beam at 500 keV when changing the current in the dipoles (the vertical dipole V and only one of the two horizontal dipoles H). In the first row, H is changing and the beam moves diagonally. In the second row, V moves the beam on the perpendicular diagonal.

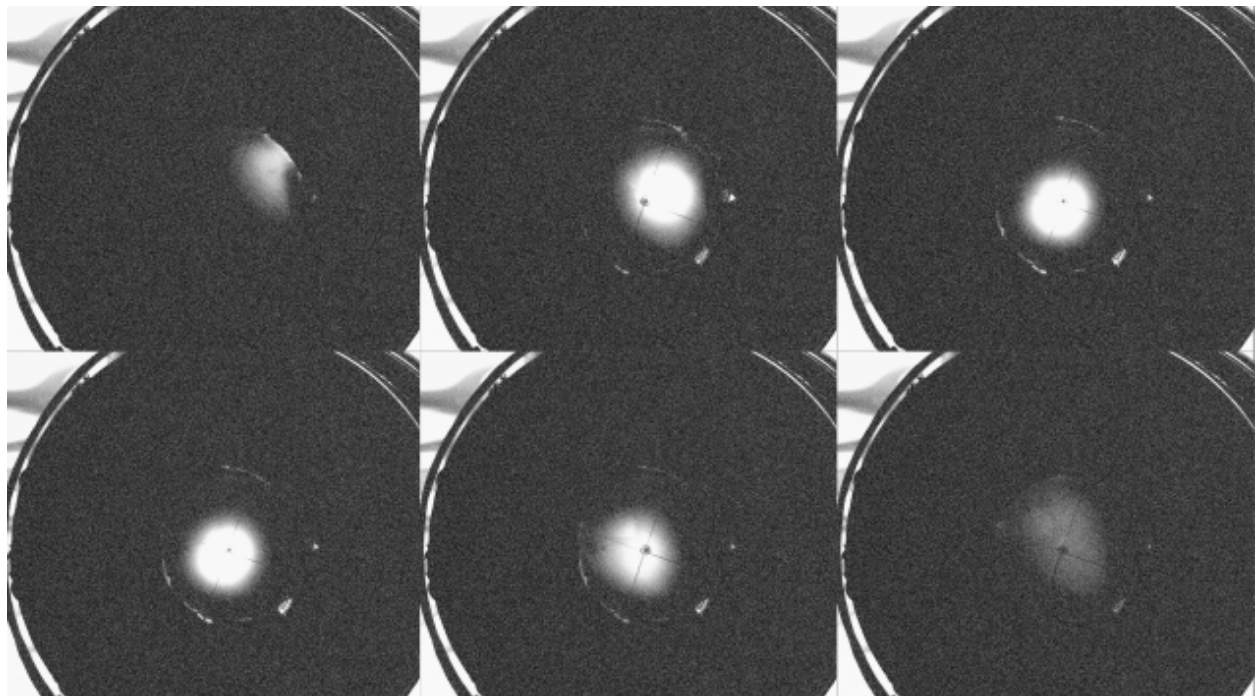


Fig. 9.2: Focus of the proton beam at 500 keV when changing the of the CW: values in the range 6 ÷ 15 keV. Is clearly visible for extreme values the beam barely reaches the crystal.

9.3.2 Asymmetry

9.3.3 Normalization

9.4 Data analysis

9.4.1 Pair reconstruction

B inversion

VerteXing

9.4.2 Asymmetry

BGO

XEC

9.4.3 Feldman-Cousin

Although the Feldman-Cousin approach is well-established in particle physics research, this was our first hands-on experience. After studying the relevant papers ([1][2]) and the internal notes of the collaboration we decided to develop a mock-up experiment to understand the framework necessary for a Feldman Cousin approach to data analysis. Given a measured sample and the probability density functions (PDFs) the framework we developed allows us to perform the analysis and obtain the confidence intervals. The full-blown X17 analysis was actually performed with the code already written for the MEG II analysis. This code was developed and improved upon over many years and was both more robust and flexible. Although it was an ‘academic exercise’, this effort made understanding the existing code and the underlying theory/structure an easier task. I contributed actively to this effort until we managed to have a running structure. Although I followed the whole procedure, the finalization of the mockup¹ and the transition to the MEG II code were done by Giovanni Dal Maso.

Likelihood This is an exercise to build confidence level belts based on Feldman-Cousins ranking using binned data. The data is synthetic and composed of an exponential background with a fixed slope and a Breit-Wigner with unknown mass and width. The data is binned. For such analysis, the likelihood can be written as:

$$\mathcal{L}(\mathbf{x}|\hat{\mathcal{N}}_S, \hat{\mathcal{N}}_{BK}, \hat{m}, \hat{\Gamma}) = \frac{\hat{\mathcal{N}}^{\hat{\mathcal{N}}} e^{-\hat{\mathcal{N}}}}{\hat{\mathcal{N}}!} \prod_{i=1}^m \left(\frac{\hat{N}_S}{\hat{\mathcal{N}}} \hat{\pi}_{S,i} + \frac{\hat{N}_{BK}}{\hat{\mathcal{N}}} \hat{\pi}_{BK,i} \right)^{\hat{\mathcal{N}}_i}, \quad \hat{\mathcal{N}} = \hat{\mathcal{N}}_S + \hat{\mathcal{N}}_{BK}, \quad \mathcal{N} = \mathcal{N}_S + \mathcal{N}_{BK}$$
(9.1)

Where \mathcal{N} is the number of measured events, $\hat{\mathcal{N}}$ is the center of the Poisson distribution and $\hat{\mathcal{N}}_i$ is the number of events in the i -th bin. The $\hat{\pi}_i$ variables are uniquely determined by the signal and background PDFs, and are the expected values of the fraction of events in the i -th bin.

¹The full description of the code will be here skipped but it can be found in the following git repository [🔗](#)

PDFs The signal PDF is defined as a Breit-Wigner:

$$\mathcal{S}(m|\hat{m}, \hat{\Gamma}) = \frac{k}{(m^2 - \hat{m}^2)^2 + \hat{m}^2 \hat{\Gamma}^2} \quad (9.2)$$

with:

$$k = \frac{2\sqrt{2}\hat{m}\hat{\Gamma}\gamma}{\pi\sqrt{\hat{m}^2 + \gamma}}, \quad \gamma = \sqrt{\hat{m}^2(\hat{m}^2 + \hat{\Gamma}^2)} \quad (9.3)$$

Given $\mathcal{S}(m|\hat{m}, \hat{\Gamma})$, it is possible to evaluate the $\hat{\pi}_{S,i}$:

$$\hat{\pi}_{S,i}(m_i) = \int_{m_i - \Delta m}^{m_i + \Delta m} \mathcal{S}(m'|\hat{m}, \hat{\Gamma}) dm' \quad (9.4)$$

with Δm being the bin width. The background PDF is defined as an exponential tail:

$$\mathcal{B}(m) = \lambda e^{-\lambda m} \quad (9.5)$$

with λ fixed. Given $\mathcal{B}(m)$, it is possible to evaluate the $\hat{\pi}_{BK,i}$:

$$\hat{\pi}_{BK,i}(m_i) = \int_{m_i - \Delta m}^{m_i + \Delta m} \mathcal{B}(m') dm' \quad (9.6)$$

with Δm being the bin width.

Toy MC framework

9.5 Results and conclusions

[3] [4] [5] [6] [7] [8] [9] [10] [11]

Bibliography on X17

- [1] Gary J. Feldman and Robert D. Cousins. "Unified approach to the classical statistical analysis of small signals". In: *Physical Review D* 57.7 (Apr. 1998), pp. 3873–3889. DOI: 10.1103/physrevd.57.3873. URL: <https://doi.org/10.1103%2Fphysrevd.57.3873>.
- [2] Till Moritz Karbach. *Feldman-Cousins Confidence Levels - Toy MC Method*. 2011. arXiv: 1109.0714 [physics.data-an].
- [3] F. W. N. de Boer et al. "A deviation in internal pair conversion". In: *Phys. Lett. B* 388 (1996), pp. 235–240. DOI: 10.1016/S0370-2693(96)01311-1.
- [4] D.R. Tilley et al. "Energy levels of light nuclei A=8,9,10". In: *Nuclear Physics A* 745.3 (2004), pp. 155–362. ISSN: 0375-9474. DOI: <https://doi.org/10.1016/j.nuclphysa.2004.09.059>. URL: <https://www.sciencedirect.com/science/article/pii/S0375947404010267>.
- [5] A. J. Krasznahorkay et al. "Observation of Anomalous Internal Pair Creation in ${}^8\text{Be}$ ". In: *Acta Phys. Polon. Supp.* 8.3 (2015). Ed. by Marek Gozdz, p. 597. DOI: 10.5506/APhysPolBSupp.8.597.
- [6] Ulrich Ellwanger and Stefano Moretti. "Possible Explanation of the Electron Positron Anomaly at 17 MeV in ${}^8\text{Be}$ Transitions Through a Light Pseudoscalar". In: *JHEP* 11 (2016), p. 039. DOI: 10.1007/JHEP11(2016)039. arXiv: 1609.01669 [hep-ph].
- [7] Jonathan L. Feng et al. "Particle physics models for the 17 MeV anomaly in beryllium nuclear decays". In: *Phys. Rev. D* 95.3 (2017), p. 035017. DOI: 10.1103/PhysRevD.95.035017. arXiv: 1608.03591 [hep-ph].
- [8] Jonathan Kozaczuk. "Dark Photons from Nuclear Transitions". In: *Phys. Rev. D* 97.1 (2018), p. 015014. DOI: 10.1103/PhysRevD.97.015014. arXiv: 1708.06349 [hep-ph].
- [9] A. J. Krasznahorkay et al. "New experimental results for the 17 MeV particle created in ${}^8\text{Be}$ ". In: *EPJ Web Conf.* 137 (2017). Ed. by Y. Foka, N. Brambilla, and V. Kovalenko, p. 08010. DOI: 10.1051/epjconf/201713708010.
- [10] A. J. Krasznahorkay et al. "On the X(17) Light-particle Candidate Observed in Nuclear Transitions". In: *Acta Phys. Polon. B* 50.3 (2019), p. 675. DOI: 10.5506/APhysPolB.50.675.
- [11] Johannes Backens and Marc Vanderhaeghen. "X17 discovery potential in the $\gamma N \rightarrow e^+e^-N$ process at electron scattering facilities". In: (Oct. 2021). arXiv: 2110.06055 [hep-ph].

Acknowledgements

There have been three types of relations helping me reaching this point in my life: relatives have been a steady pillar from which I could reach out to the unknown; mentors showed me a path, leaving me the leisure of choosing to take it; friends shared with me tears and laughter along the road. None of you reading these few lines has been fixed in one of these roles and I am grateful *to you* from the bottom of my heart. I do not wish to make this page a list of names. You know your own name and I look forward to thank you in person. I feel nonetheless compelled to thank here the one I am no longer able to meet: Nonni Carlo e Vittorio, Zio Papele.

Bastiano Vitali, Rome, xx/xx/202x

